國立交通大學

電子工程學系 電子研究所碩士班

碩 士 論 文

應用於下視網膜植入之高效率
電流刺激式互補式金氧半晶片

EFFICIENT CURRENT STIMULATION
CMOS CHIPS FOR SUBRETINAL PROSTHESES

研 究 生 ： 柳慧君
指導教授 ： 吳重雨 教授

中華民國九十九年八月

EFFICIENT CURRENT STIMULATION CMOS CHIPS FOR SUBRETINAL PROSTHESES

應用於下視網膜植入之高效率電流刺激式互補式金氧半晶片

研 究 生： 柳慧君　　Student : Hui-Chun Liu

指導教授： 吳重雨 教授　　Advisor: Prof. Chung-Yu Wu

國立交通大學

電子工程學系 電子研究所碩士班

碩士論文

A Thesis

Submitted to Department of Electronics Engineering & Institute of Electronics
College of Electrical and Computer Engineering
National Chiao-Tung University
in Partial Fulfillment of the Requirements
for the Degree of Master
in
Electronics Engineering
August 2010

Hsin-Chu, Taiwan, Republic of China

中華民國九十九年八月

應用於下視網膜植入之高效率
電流刺激式互補式金氧半晶片

學生：柳慧君　　指導教授：吳重雨教授

國立交通大學　電子工程學系電子研究所碩士班

ABSTRACT (CHINESE)

本篇論文中描述三種應用於下視網膜療程中的人工矽視網膜晶片設計與驗證，以提升感光電流刺激效率。包含單顆光電池陣列刺激晶片，兩顆串聯光電池陣列刺激晶片，與四區塊分區供電刺激晶片。

我們已設計並實作單一光電池陣列刺激晶片的體外生物實驗，成功的驗證視網膜晶片刺激視網膜細胞的生物反應，並得到使用75μm x 75μm的刺激電極，僅需不到0.28nC的電荷就可使視神經細胞產生反應。我們所設計的感光陣列中的單一像素均具有臨近的環繞式回流電極，由模擬中已驗證此種回流電極的設計方法可給予視網膜1.08μA的刺激電流，比擺放在遠端的環繞式回流電極的刺激電流高出三倍，且比擺放在遠端的單一回流電極的刺激電流高出十倍。將兩顆光電池串聯可得到較高的電位，基於我們由不同大小的微電極晶片已量測到視網膜與電極界面的阻抗在低操作頻率時超過一百萬歐姆，因此礙於小電位差單顆光電池陣列較難輸出電流。兩顆串聯光電池陣列的電路設計以提高電位的方式，在感光面積比單顆光電池陣列較小的情況下，可給予視網膜2.09μA的刺激電流，兩顆串聯的比單顆的光電池陣列高出近兩倍的電流刺激效能，用以改善視網膜阻抗過高的問題。在使用臨近的環繞式回流電極下，由模擬結果可得到單顆與兩顆串聯的光電池陣列最佳的感光面積分別為14400μm^{2}與19200μm^2，在此感光面積下，兩顆串聯光電池陣列的刺激電流比單顆的大1.65倍。

在四區塊分區供電的晶片設計中，已證明電路系統與光電池同時整合在互補式金氧半積體電路晶片上的可能性，並驗證各個區塊輪流使用光電池供電系統以提升電源管理效率的可行性。在原本1066顆光電池外，加入2540顆光電池，即可產生四個沒有重疊且不同相位的控制訊號。晶片的產生時脈電路在15.8mW/cm^{2}的光照強度下，可產生1.5kHz的震盪，且其電路消耗功率僅為24.8nW。四區塊分區供電的電路可以產生在相同光照強度下可以得到約略1.1μA的電流輸出，比將5003顆光電池分成十六像素高約三倍的有效

輸出電流，以提供視網膜細胞所需要的電性刺激，並節省四倍的電源。所提出電源管理架構大大改善了下視網膜療程中，金氧半晶片的電能使用效益與電流刺激效能。

在台灣積體電路製造股份有限公司與國家晶片系統中心的幫助下，不同大小的微電極晶片與單顆光電池陣列刺激晶片以0.35μm製程實現，兩顆串聯光電池刺激晶片與四區塊分區供電的刺激晶片以0.18μm製程實現。基於上述特性，此視網膜阻抗的分析結果，與三種視網膜電流刺激晶片的架構，均對下視網膜療程中的晶片設計上有相當程度的貢獻。

EFFICIENT CURRENT STIMULATION CMOS CHIPS FOR SUBRETINAL PROSTHESES

Student: Hui-Chun Liu **Advisor: Prof. Chun-Yu Wu**

Department of Electronics Engineering &Institute of Electronics
College of Electrical and Computer Engineering
National Chiao-Tung University

ABSTRACT (ENGLISH)

In this thesis, new retinal stimulation chips have been designed, analyzed, and fabricated to improve current stimulation efficiency of the subretinal prosthesis. Three types of stimulation chip are proposed, one is single solar cell array stimulation chip; another is two cascode solar cell array stimulation chip and still another is four-block divisional power-supply stimulation chip.

The single solar cell array stimulation chip with local surrounding return electrode has been designed and verified after the in vitro experiment. The silicon retina with solar cell array can successfully trigger the ganglion cells with threshold charge lower than 2.8nC with 75μm x 75μm stimulating electrode. Probed retinal stimulation current of solar cell array with local surrounding return electrode is 1.08μA, which is 10 times of remote surrounding return and 3 times of remote single return. Probed retinal stimulation current of two cascode solar cell array is 2.09μA, which is 2 times more current efficient than single solar cell array. Retina interface impedance has been measured by the multi-size microelectrode chip. Retina interface impedance decreases with increasing frequency, increasing electrode size and decreasing center-to-center distance of electrodes. At low frequency, retina interface impedance is over 1MΩ which is difficult for stimulation current generated from solar cell array to flow into retina. High potential of two cascode structure is one of the solutions to this problem. With local surrounding return electrode, optimum photo-sensing regions of each pixel of single and two cascode solar cell array stimulation chips are 14400μm^2 and 19200μm^2 and current stimulation efficiency with the optimum photo-sensing region of the latter is 1.65 times larger than the former.

In the work of four-block divisional power-supply stimulation chip, the capability of on-chip solar cell supply system integrated with circuit system in CMOS technology has been

proved, and the feasibility of using power supply system in turn to elevate power management efficiency has also been verified. Power control unit with original 1066 solar cells and extra 2540 solar cells is able to generate four power control signals, which are nonoverlapping and on different phases, to control each block of pixel array. Clock frequency is 1.5kHz under 15.8mW/cm^2 incident light intensity with only 24.8nW power consumption. The output stimulating current of each pixel is approximately 1.1μA under same light intensity. Comparing with 16-pixel conventional solar cell array, which can only generate 0.31μ A at 15.8mW/cm^2 for total 5003 solar cells, output stimulation current of four-block divisional power supply stimulation chip is 3 times higher and power efficiency is 4 times higher. The proposed power management structure could be considered as one of the highly integrated solutions for the efficient current stimulation CMOS chips of subretinal prosthesis.

Multi-size microelectrode chip and single solar cell array stimulation chip are fabricated with standard 0.35μm and tsmc process; two cascode solar cell array stimulation chip and four-block divisional power-supply stimulation chip are fabricated with standard 0.18μm tsmc CMOS process. The proposed efficient current stimulation chips all have contribution to the subretinal prosthesis.

ACKNOWLEDGEMENTS

致謝

首先誠摯的感謝指導教授吳重雨博士,讓我成為奈米晶片與系統實驗室(307實驗室)的一份子。在吳教授循序漸進的教誨、無與倫比的耐心與滿懷愛心的鼓勵下，使我得以獲得許多積體電路設計的專業知識，並不斷從問題中尋找到答案，更學會遭遇難題的解決態度與方法。另外也要特別感謝和藹可親的師母曾昭玲女士，謝謝她不時給予我關懷與鼓舞，讓我重新找回研究的熱忱。

此外，我還要感謝林伯剛醫師在醫學領域，與焦傳金老師在細胞電生理領域的指導與協助，並感謝焦老師的學生楊雅婷學姊在量測過程中的協助，讓這份跨領域的研究能夠順利完成。

在這段求學過程中，307實驗室給予了我完善的硬體及軟體資源，讓我能夠順利的完成學業，全靠歷代學長姐們努力經營實驗室，讓實驗室如此成長卓越，並有相較於其他實驗室更有系統的體制。另一方面也要感謝林俐如、陳勝豪、楊文嘉、陳煒明、王文傑、黃祖德、蘇烜毅、蔡夙勇、劉麗珍、萬諶、許筱妊、蔡宗昀、陳偉丞、周敬程等實驗室學長姐的細心指導，讓我的研究可以順利進行；另外也感謝及助理卓慧貞小姐與李清音小姐，給予我在研究上的資源及行政上的幫助，讓我完成學業。

接著要感謝的是一起打拼的同學們：明翰、子薰、健軒、書瑾、旻毅、文杰、偉霖、堂龍、詩翰、佑達等。大家一起努力修課、做考古題，熬夜趕工，出遊玩樂，讓我的碩士生活增添風采。謝謝你們一直以來的陪伴與關懷，並互相扶持，加油打氣讓我能充電再繼續努力。

最後，我要致上最深的感謝給予我最親近的父母親，由於他們一直以來的關心、支持與無微不至的照顧，並用心的栽培我讀書，進而讓我擁有今日的成就。還要感謝姐姐的幫助與鼓勵，及男友的照顧與陪伴，讓我在安逸與溫馨中念完碩士。最後祝福我的師長、家人、朋友及學弟妹們事事順心、身體健康。我在撰寫的過程中，雖力求嚴謹，然誤謬之處，在所難免，尚祈各位讀者賜予寶貴意見，使本論文能更加完善。

柳　慧　君

謹誌於竹塹交大

庚 寅 夏

CONTENTS

TABLE CAPTIONS

CHAPTER 2

CHAPTER 3

CHAPTER 4

FIGURE CAPTIONS

CHAPTER 1

CHAPTER 2

CHAPTER 3

CHAPTER 4

CHAPTER 1 Introduction

1.1 Background

Vision is one of the most important sensory organs and thus losing vision can bring one endless torments. The vertebrate retina can perform two functions. Firstly, the photoreceptors (rods and cones) are able to transducer the information of the optical image into neural signals. Secondly, the neural circuitry is able to abstract certain features of the visual world. Via optic nerve fibers, the features can form large number of photoreceptor signals and pass the information on to the brain.

Currently, over 10 million people worldwide are afflicted with photoreceptor degenerative diseases that reduce vision to bare light perception or complete blindness [1]. Retinitis pigmentosa (RP) is the leading cause of inherited blindness with 1.5 million people worldwide affected and an incidence of 1/3500 live births. Also, age-related macular degeneration (AMD) is the leading cause of visual loss among adults older than 65, with 0.7 million patients newly diagnosed annually in the United States, 1/10 of whom become legally blind each year [2]. Once photoreceptors are nearly completely lost, such as in end-stage RP or AMD, very few approaches can restore useful vision to blind patients. One possible avenue that has been explored is to use implantable microelectronics. The different methods currently being pursued to electrically stimulate damaged areas of the visual system include electrical and neurotransmitter stimulation of the retina, as well as the use of light-sensitive nano-particles. Implantable methods can be categorized by the extraocular or intraocular sites of device implantation.

Extraocular implantation includes the visual cortex and optic nerves. Dobelle's 64-channel platinum electrode surface stimulation prosthesis of the occipital cortex was shown to allow blind patients to recognize 6-inch characters at 5 feet [3]. However, this prosthesis encountered several difficulties including controlling the number of phosphenes induced by each electrode. The optic nerve is a dense neural structure with approximately 1.2 million axons confined within a 2-mm diameter cylinder [4]. While this allows the entire visual field to be represented in a relatively small area, it remains difficulties to achieve focal stimulation of neurons and to decipher the exact retinotopic distribution of the optic nerve.

Implementation of the artificial retinal prosthesis system can be classified by

intraocular implantation sites. Four prostheses are well known; these include the transscleral, suprachoroidal, subretinal and epiretinal prostheses. Four different implantation sites are shown in Fig. 1.1, transscleral prostheses are implanted on the sclera; suprachoroidal prostheses are implanted on the choroid; subretinal prostheses are implanted between the pigment epithelial layer and the degenerated photoreceptors; epiretinal prostheses are implanted onto the inner retinal membrane.

Transscleral and suprachoroidal stimuli were designed to minimize insult to the retina by electrode stimulation. The fibers of the electrode of the transscleral implantation were placed on the lower bulbar conjunctiva 5mm from the corneal limbus [5]. The anodic stimulating electrode of the suprachoroidal implantation was positioned on the choroidal membrane and the cathode was placed in the vitreous body [6]. Due to less direct stimulation of the retina, the threshold charge densities of these two prostheses were as large as 318μC/cm^2 [5] and 790μC/cm^2 [7], respectively, which are higher than direct stimulation of the retina. Subretinal prostheses are trying to directly stimulate the remaining intact retinal neurons—bipolar or horizontal cells, the initial neuronal processing stage of the retina—by currents generated from photodiodes or electrodes. Epiretinal implants have been designed to directly stimulate retinal ganglion cells—the final and intricate retinal processing stage—with an electrode array.

The majority of the groups currently working in visual prosthetics are concentrating either on epiretinal (e.g., [8-14]) or subretinal (e.g., [15-21]) electrical stimulation. In the next section, we will review on these two prostheses.

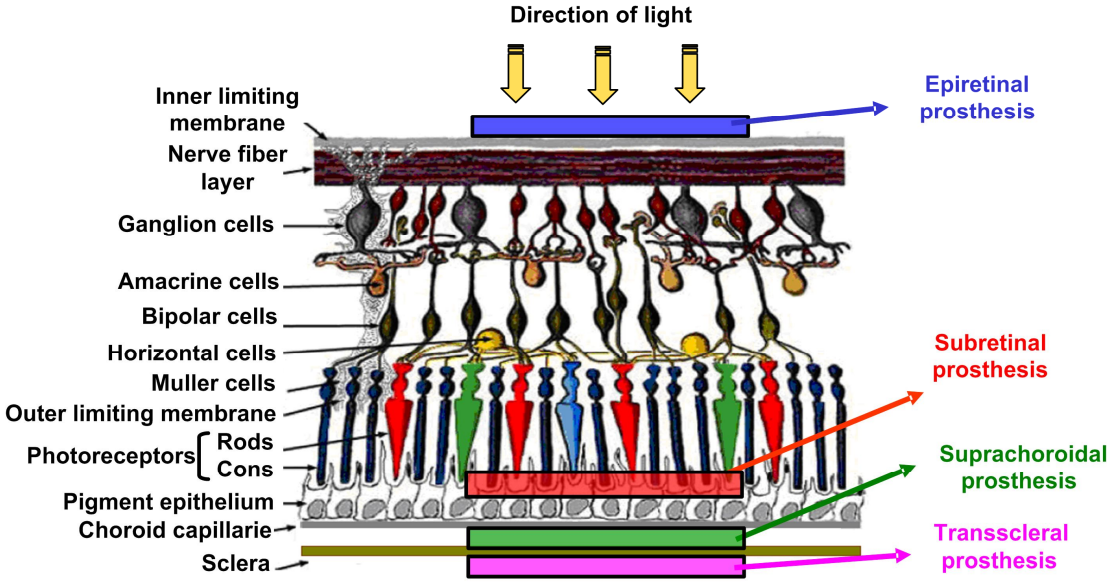

Figure 1.1 Cross-section of retina and implementation system of artificial retina prostheses. (Image courtesy of Webvision, webvision.med.utah.edu.)

1.2 Review on Epiretinal and Subretinal Prostheses

1.2.1 Epiretinal Prosthesis

The idea of the epiretinal prosthesis resembles that idea of the cochlear implant. The cochlear implant converts sound into electrical impulses to stimulate the auditory nerve in the inner ear. The conceptual prosthetic system of Fig. 1.2 shows that the epiretinal prosthesis involves the capture and digitization of images from the external world with a device such as a camera. These images are transformed into patterns of electrical stimulation, which are used to excite remaining, viable inner retinal neurons. Significant power and data telemetry mechanisms are required to drive this process. Several groups worldwide have developed different designs of epiretinal implants that vary in terms of the intraocular and external elements which constitute the devices and how they function to enable vision in patients. They were all guided by similar requirements, which included preserving as much of the normal anatomy/physiology of the eye as possible while minimizing the amount of implanted electronics required to power the device [8]. Three such approaches are described below.

The Intraocular Epiretinal Prosthesis (IRP) was initiated by a team led by Dr. Mark S. Humayun at the Doheny Eye Institute of the University of Southern California. IRP was composed of a pair of glasses housing a miniature video camera, an external visual processing unit, an intraocularly implanted stimulating electrode array, and inductive coil for wirelessly relaying power and data. The visual processing unit acquired and digitized video input from the camera, applied various filters on the image (e.g. edge detection, contrast enhancement, difference of Gaussian), and downscaled the resolution to a 6 x 10 grid. This processed information, in the form of controlled patterns of electrical pulses, was then transmitted into the eye by magnetic coils of the inductive link telemetry system and sent to the temporal skull. The microelectrodes on the array applied these pulses to stimulate any viable inner retinal neurons. The array was positioned just temporal to the fovea and was attached to the inner retinal surface using a single tack, which was inserted through the electrode array into the sclera as shown in Fig. 1.2 [9]. This 60-pixel image was then mapped to a stimulation intensity using customized look-up tables that have been derived from testing of individual patients. To date, 21 patients with degenerated photoreceptors have received the 60-electrode device. Seventeen patients described visual

perceptions of retinotopically consistent phosphenes that were seen when local current was applied to the surface of the retina with the implanted electrodes. At the 6th month followed up testing points, average success rates of touching the door with the system on and off were 59% and 32%; tracking the line until the end with the system on and off were 44% and 26%. With a perceptual threshold ranging from 24μA to 702μA (1 ms pulse), patients were not only able to distinguish the direction of motion of objects but also to discriminate between percepts created by different electrodes based on their locations. These phenomenons demonstrate that retinotopic organization is not lost when a patient loses sight [10].

The Learning Retina Implant (LRI) was developed by a consortium of 14 expert groups in Germany directed by Rolf Eckmiller since 1995. LRI also comprised of intraocular and extraocular components. The retina encoder (RE), which approximated the typical receptive field properties of retinal ganglion cells, replaced the visual processing capabilities of the retina by means of 100 to 1000 individually tunable spatiotemporal filters. The RE was situated in the frame of a pair of glasses or embedded in a contact lens. The processing of visual information that occurd in the RE simulated the filtering operations performed by individual ganglion cells. The RE output was then encoded and transmitted via a wireless signal and energy transmission system to the implanted retina stimulator (RS). The RS was a ring-shaped, soft micro-contact foil centered about the fovea that was affixed to the epiretinal surface and must be in contact with a sufficient number of retinal ganglion cells/fibers to elicit electrical spikes as shown in Fig. 1.3 [11]. Visual patterns were mapped onto spike trains for the contacted ganglion cells through the REs. The REs not only simulated the complex mapping operation of parts of the neural retina, but also provided an iterative, perception-based dialogue between the RE and human subject. The purpose of this dialogue was to tune the various receptive field filter properties with information “expected” by the central visual system to generate optimal ganglion cell codes for epiretinal stimulation. In order to optimize the dialog between the retina encoder and the central visual system, proper stimulation coding of electrically induced neural signals for the retinal ganglion cells in contact with the RS needed to be determined [12]. Clinical trials primarily focusing on testing of the learning implant and dialogue-based RE tuning had being done but no much success has been reported so far.

A third epiretinal prosthesis was developed by Joseph 3rd Rizzo and John Wyatt at the Harvard Medical School. Their version of an implant was similar to that of the IRP group in that it consisted of distinct intraocular and extraocular modalities. The

intraocular components were composed of a photodiode panel and a stimulator chip that were affixed, away from the retinal surface, onto a modified intraocular lens. A flexible 10-μm thick polyimide electrode array was implanted onto the retina, rather than held above the retinal surface, as performed by Humayun et al., and attached to the epiretinal surface using a small gold weight and a viscoelastic made of hyaluronic acid. The extraocular unit was composed of a charge coupled device camera, a signal processing unit, as well as a laser, all mounted onto a pair of glasses. The battery back which powered the device was also located external to the eye. The photodiode panel captured the processed signal from a laser pulse emitted from the glasses and the stimulator chip then delivered this information to the microelectrode array on the epiretinal surface of the eye [13]. Implantation in 5 blind patients with RP and 1 normal-sighted patient who was scheduled for enucleation due to orbital cancer had been done. Similar to the results found by the IRP group, they observed that higher charge densities were required to stimulate the retinas in patients with worse vision, with the 400-μm electrode in blind patients charge density thresholds were 0.28 to 2.8mC/cm^2. No apparent damage as a result of electrical stimulation of the retina was evident of the normal-sighted patient's eye. The results from their short-term studies in 5 patients were mixed and inconclusive. Simple pattern vision was not achieved by either the blind or the normal sighted patients when multi-electrode patterns of electrode stimulation were applied in trials with multiple electrodes [14]. Due to the inability of getting good or consistent results with epiretinal stimulation, Rizzo and Wyatt have abandoned the epiretinal approach and are now developing a subretinal approach.

Some disadvantages come along with advantages in these prostheses. Firstly, with inductive coil for wirelessly relaying power and with electrical pulses from wiring, microelectrodes on the array can stimulate any viable inner retinal neurons for sufficient power supply. But, heat dissipation by intraocular prosthesis components may cause elevated temperature and thus damage the eyeball. Secondly, the implementation of the prosthesis onto the retina may carry on pixel-tuning after surgery easily, but this also means that fixation of electrode array requires some of retinal tack which can dislodge, e.g. due to trauma. Besides, in conjunction with the foreign material of the array as well as electrical impulses deliver to the implant could possibly result in fibrous encapsulation of the tack. Thirdly, in most cases, both intraocular and extraocular components are required to make good functions. Limited area of epiretinal space will greatly confine the goal of implantation of 1000-electrode epiretinal prosthesis. Lastly, in order for a desired visual percept to be generated by

the central visual system, significant information in the form of electrically induced neural signals must not only be provided by the retina stimulator or encoder system but also be clear or unambiguous for interpretation by the brain, therefore, stimulation sites uncertainty is a big challenge.

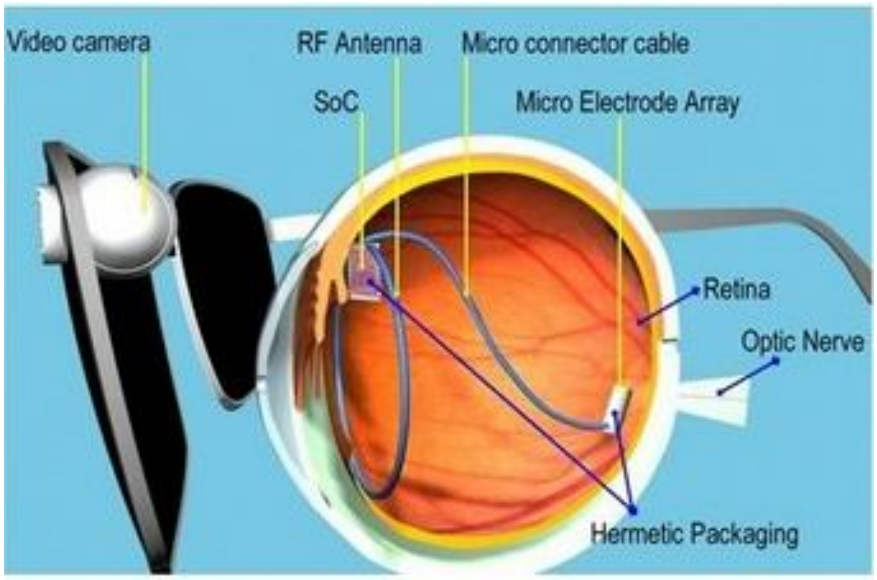

Figure 1.2 System overview of an epiretinal implant. (Reprinted from http://www.cbse.ucsc.edu.)

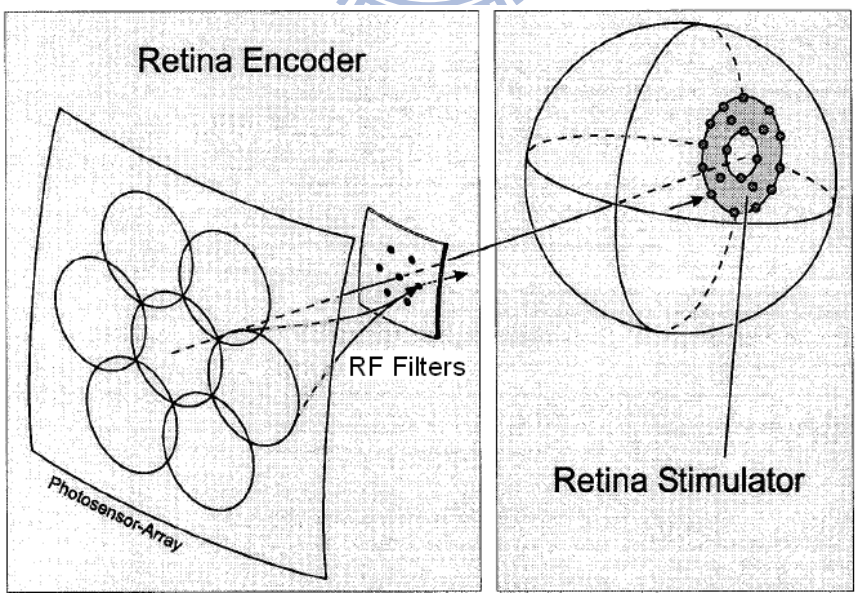

Figure 1.3 Schematic of the retina implant with a retina encoder outside the eye and an implanted retina stimulator adjacent to the ganglion cell layer. (Reprinted from "Dialog concepts for learning retina encoders," by R. Eckmiller).

1.2.2 Subretinal Prosthesis

The fundamental concept of the subretinal approach is to restore vision by means of prosthesis involves the implantation of micro-photodiode array between the bipolar and horizontal cell layer and the retinal pigment epithelium. Subretinal implants are trying to stimulate the ganglion cell layer through the remaining intact retinal neurons by currents generated from photodiodes or electrodes. Implants act like photoreceptors and its stimulation on the ganglion cells may result in a correlated stimulus in location and a perceived stimulus in vision. Four such approaches are described below and are categorized by the power sources. Passive devices rely on incident light for power, whereas active devices have external power sources.

The first passive device was developed by Alan and Vincent Chow of Optobionics Corp, who believed that a subretinal implant could function as a simple solar cell without the need for a power or input source of any type [15]. Their Artificial Silicon Retina (ASR) Microchip was powered entirely by light entering the eye, without batteries or other ancillary devices. Two millimeters in diameter, the ASR contained approximately 3500 microelectrode-tipped micro-photodiodes which converted incident light into electrical signals similar to those normally produced by the retina's own photoreceptors. The photodiodes had a photoelectric efficiency of 0.45A/W per cm^2 and developed a maximum compliance voltage of 450 mV with a 1 MΩ resistance. These electrical impulses, in turn, stimulated any viable retinal neurons, which then processed and sent these signals to the visual processing centers in the brain via the optic nerve. As part of a safety and feasibility study, the ASR Microchip was implanted in 6 patients, with a follow-up of 6 to 18 months. Some of the patients had reported improved visual function away from the implant site, suggesting that the presence of the implant alone, or coupled with low-level electrical stimulation, induced a "neurotrophic effect" that improved the health of the retina and consequently improved visual function. However, the reports demonstrated that the idea behind this simple approach is not feasible, because it lacked a source of viable power and stimulating charge density was only 0.1nC/cm^2 [16].

An active device for a subretinal implant was initiated by a consortium of research universities in Germany since 1996 under the guidance of Eberhart Zrenner. Their subretinal Integrated Circuit (IC) was composed of a micro-photodiode array which contained approximately 1500 microelectrodes in a checker-board pattern configuration and served to modulate current pulses based on the amount of light incident on the photodiode [17]. A micro-fabricated cable that passed out of the orbit

and crossed the skin behind the ear supplied command and configuration signals as well as power to the subretinal IC. Because such a cable arrangement is a potential infection source, the implant was limited to 30 days. This implant also included 16 “direct stimulation” electrodes, and the electrodes were not activated by the subretinal IC but were directly connected to the cable and were activated by external equipment. Due to packaging limitations, the subretinal IC did not function in all of the implants. Direct stimulation electrodes were able to elicit responses in all subjects [18]. This device applied constant voltage stimulation and adequate stimulus levels (1–2.5 V for 0.5-6ms) to generate perceptions. In recent reports, 11 patients received subretinal implants. Subretinal multi-electrode implants with charge close to recognition threshold (10 to 27nC/ electrode or 0.4mC/cm^2 to 1.08mC/cm^2) produced correct patterns that allowed for the recognition of individual letters even at low luminance levels [19]. This clearly supports the feasibility of light sensitive subretinal multi-electrode devices for restoration of useful visual percepts in blind patients.

Another type of active device subretinal prosthesis was recently developed by Rizzo and Wyatt. The size of the implanted device is 12mm x 31mm. Schematic diagram of the wireless operation of the visual prosthesis system is shown in Fig. 1.4. A camera and transmitter collected and then rebroadcasted an image signal to the implanted stimulator chip, which was to retransmit biphasic current pulses, in patterns corresponding to the desired image, to the stimulating electrode array located in the subretinal space. The implant positioned large coil and electronics structures at a distance of approximately 1.5cm from each other; thereby the device may be implanted in the superior nasal and superior temporal quadrants of the ocular orbit. The middle section of the device contained only the polyimide host flexible circuit and a large reference/return electrode, which could be implanted underneath the superior rectus muscle. Only the flexible, 16-μm thick polyimide array with iridium oxide (IrOx) stimulating electrodes enters the scleral flap, which was typically made 10mm posterior to the limbus. The chip, capable of delivering up to 775μA stimulation current, drove 15 electrodes with 15 current-source drivers. Though this project is still in its early stages of development, they have reported that biocompatibility studies examining the effects of a foreign material in the subretinal space as well as surgical methods to implant their device have been extensively evaluated. While their results have been encouraging to date, further studies regarding the long-term biocompatibility of materials in the subretinal space as well as methods to protect the retina upon insertion of the prosthesis during surgery will need to be performed before a clinical trial is conducted to determine the safety and efficacy of

their implant in blind patients [20].

A second type of passive device subretinal prosthesis was recently developed by Jim Loudin et al. of Stanford University. Unlike the project done by Alan and Vincent Chow, which no image processing system was involved, they developed a retinal prosthesis system shown schematically in Fig. 1.5. Video stream from a miniature camera was processed and imaged onto the retinal implant by a video goggle projection system using 905nm near-infrared light. This wavelength is practically invisible to photoreceptors, and therefore does not interfere with any residual vision. However, it could be detected by implanted photodiodes, which converted pulsed (~0.5ms) light into pulsed electric current, with charge injection maximized by specially optimized photodiode circuits. This system delivered information to all pixels in parallel and scaled large numbers of pixels straightforward. Also, image processing was adjustable and many separate arrays could be implanted to expand the field of view. Several circuit diagrams of the photoconductive and photovoltaic cells were developed. One, two, and three diodes in series connection were studied in both anodal and cathodal polarities. With 50-μm side length sputtered iridium oxide film (SIROF) square electrodes and illuminating 0.3-mW light power per diode, the charge injection per photo-sensing region and stimulating charge density of a cathodal or an anodal diode were only 0.29nA/μm^2 and 0.2mC/cm^2, respectively. Among the developed structures, an anodally biased photoconductive circuit generated the greatest charge injection (1.6nA/μm^2 and 1.1mC/cm^2). These values were million times of a single photodiode developed by Alan and Vincent Chow. Although this project is still in its early stages of development, prostheses of pixel densities from 16pix/mm^2 to 256pix/mm^2 have been designed, simulated, and prototyped. Retinal tissue response to subretinal implants made of various materials has been investigated in RCS rats [21]. The prosthesis is expected to provide sufficient charge injection for high resolution retinal stimulation without the requirement for implantation of any bulky discrete elements such as coils or wiring.

The approaches of subretinal prostheses, like other methods of artificial vision, have its distinct advantages and disadvantages. One advantage is that the micro-photodiodes of a subretinal prosthesis directly replace the functions of the damaged photoreceptor cells while the retina's remaining intact neural network is still capable of processing electrical signals. Placement of the subretinal prosthesis in closer proximity to any remaining viable inner retinal neurons in the visual pathway may be advantageous in decreasing current requirement for stimulation. In addition to the relative ease in positioning and fixing the micro-photodiodes in the subretinal

space, the lack of mechanical fixation allows for less surgically induced trauma upon implantation. Unlike the epiretinal prostheses, external cameras or image processing units are not required and the patients' eye movements can still be used to locate objects. With photodiodes as power supply rather than wire-line connections, no difficulties are in keeping sterile and scarring problems are less.

One of the disadvantages of active devices is the limited area of the subretinal space, which contains the microelectronics, predisposes the contacted retinal neurons to an increased likelihood of thermal injury resulting from heat dissipation of wiring. Additionally, if the subretinal implant is only composed of an electrode array with the electronics outside the eye, then the prostheses must have a cable piercing the sclera leading to potential tethering on the cable. The tethering effect on the electrode array in the subretinal space can lead to possible movement after implantation as well as the more invasive transchoroidal incision and extensive subretinal bleeding.

On the other hand, the main disadvantage of passive devices is that stimulation current of the device is in proportion to photo-sensing region of each pixel, and thus limited area of the subretinal space confines the stimulation efficiency or resolution of this prosthesis. Thereby to improve the current stimulation efficiency of passive devices in a limited area of subretina is the major concern of this prosthesis.

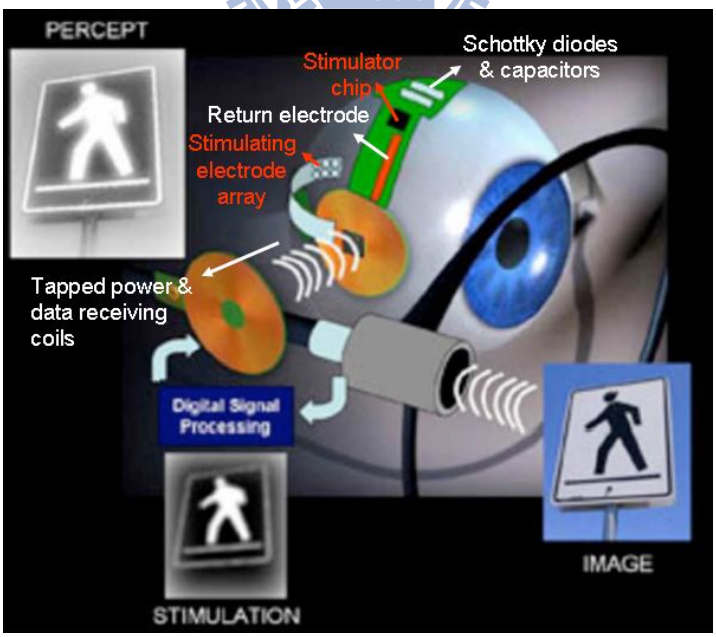

Figure 1.4 Schematic diagram of the wireless operation of the visual prosthesis system. (Reprinted from "Development and implantation of a minimally invasive wireless subretinal neurostimulator," by Rizzo and Wyatt).

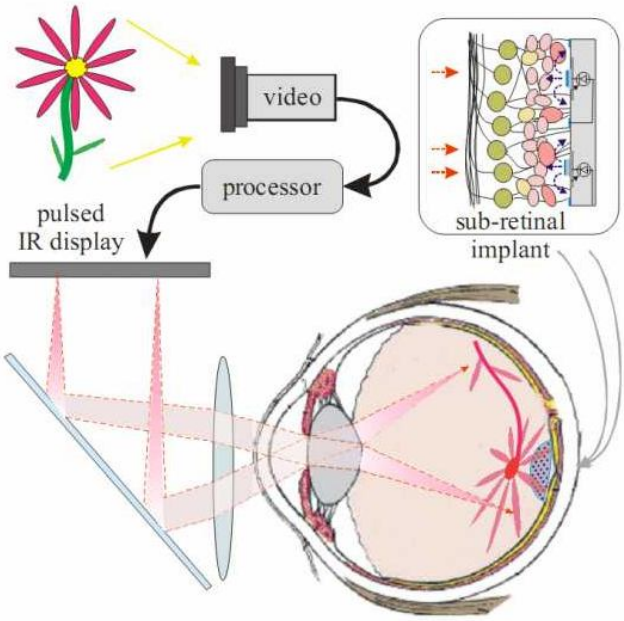

Figure 1.5 System overview of an subretinal implant. (Reprinted from "Optoelectronic retinal prosthesis: system design and performance" by Jim Loudin et al., Stanford University).

1.3 Motivations

To develop efficient current stimulation CMOS chips with passive devices for subretinal prosthesis, three major concerns are listed below.

A dense current stimulation chip with a small electrode per pixel is desirable to achieve maximum visual acuity. However, the output load of a stimulator is retina interface impedance. The impedance would vary with the size of electrodes [22]. Smaller electrode size results in a larger output load. Besides, with different return electrode to stimulating electrode distances, retina interface impedance ought to be different. Photocurrent, generated from a passive device, could barely stimulate the retina if the output load is too large compared with photoresistance. Therefore, to measure retina interface impedance with multi-size microelectrodes and different return electrode to stimulating electrode distances is the first priority in the design of retinal prostheses.

Solar cell array stimulation chip with multi directions of return path could enhance the stimulation efficiency [23]. Thus the shape of return electrodes is also relative to the current stimulation efficiency. Different kinds of return electrode have to be designed and evaluated the best one. Solar cell array with thousands of solar cells and

the best return electrode type can stimulate retina cells with large photocurrent. Solar cell with many two cascode solar cells and the best return electrode type can stimulate retina cells with even large current because of large photovoltage. Resolution of the photodiode arrays larger than 16 pixels can mimic partial photoreceptors well [24].

Power management efficacy of solar cell array can be elevated by redistribution of solar power to pixel array. One method is to facilitate the refractory period of vision. The retinal stimulation chips need not to stimulate the retina cells continuously but discretely. The maximum frame rate which can be distinguished by human is about 60Hz, namely, stimulating retina cells every 16ms or less, the brain of a patient still consider discrete stimuli as continuous ones. Applying the power control unit to the pixel array, each pixel activates in accordance with divisional blocks and uses solar cell power supply in turn. Output stimulation current and power efficiency are proportional to the divisional block numbers.

1.4 Main results and Thesis Organization

Four chips had been made in the development of efficient current stimulation CMOS chips for subretinal prosthesis.

First chip is multi-size microelectrode chip which was fabricated with standard 0.35μm tsmc process. The function is to measure retina interface impedance. From the measurement and analysis results, retina interface impedance not only decreases with increasing frequency and increasing electrode size but also decreases with decreasing center-to-center distance of electrodes. The analyzed retina impedance is in the range of 10kΩ to 200kΩ with 50-μm to 80-μm side length square electrodes.

Second chip is single solar cell array stimulation chip and was also fabricated with standard 0.35μm tsmc process. The main function of this chip is to efficiently stimulate retina cells with large photocurrent by 2540 parallel solar cells in each pixel. The other one is to mimic photoreceptor cells with 16 pixels. With 3-dimensional spreading resistive network simulation model, stimulation current passing through thick retina resistance of single solar cell array with local surrounding return electrode is 1.08μA, which is 10 times of remote surrounding return and 3 times of remote single return. By using the local surrounding return, optimum photo-sensing region of solar cells is 14400μm^2 and maximum photocurrent per photo-sensing region is 2.55pA/μm^2. The stimulation chip with single solar cell array and 75μm x 75μm stimulating electrode can successfully trigger the ganglion cells with low threshold

charge of 2.8nC, which is 3.5 times lower than Zrenner et al. in 2009 [19].

Third chip is two cascode solar cell array stimulation chip which was fabricated with standard 0.18μm tsmc process. The main function is to efficiently stimulate retina cells with high photovoltage by connecting two solar cells in series. With 414 parallel two cascode solar cells, stimulation current passing through thick retina resistance is 2.09μA, which is 2 times more current efficient than single solar cell array. By using the local surrounding return, optimum photo-sensing region of solar cells is 19200μm^2 and maximum photocurrent per photo-sensing region is 3.15pA/μm^2.

Fourth chip is four-block divisional power-supply stimulation chip which was also fabricated with standard 0.18μm tsmc process. The purpose of this chip is to increase power management efficiency and current efficiency with divisional power control system. The time interval between neighboring activation of the same pixel is smaller than refractory period of the retina cell thus to provide continuous signals for the brain. Power control unit with original 1066 solar cells and extra 2540 solar cells is able to generate four power control signals, which are nonoverlapping and on different phases. Clock frequency is 1.5kHz under 15.8mW/cm^2 incident light intensity with only 24.8nW power consumption. The output stimulation current is approximately 1.1μA under the same light intensity. Comparing with 16-pixel conventional solar cell array, which can only generate 0.31μA at 15.8mW/cm^2 for total 5003 solar cells, output stimulation current per pixel of four-block divisional power supply stimulation chip is 3 times higher. The capability of on-chip solar cell supply system integrated with circuit system in CMOS technology has been proved, and the feasibility of using the power supply system in turn has also been verified.

The remainder chapter of this thesis is organized as follows:

Chapter 2 describes the method to stimulate isolated retina and to record retina interface impedance from stimulators and recorders of multi-size microelectrodes, also analyzes three components of interface impedance by model.

Chapter 3 compares electrical characteristic and current stimulation efficiency of single and two cascode solar cell array, simulates three different designs of return electrodes, and records electrical responses of isolated rabbit's retina.

Chapter 4 considers the divisional architecture of current stimulation chips that integrate solar cells and CMOS technology together. The chips were designed, measured, and verified as a power efficient method of subretinal prosthesis.

Chapter 5 concludes our research presented in this thesis and puts forth some thoughts for future work.

CHAPTER 2 Analysis of Retina Interface Impedance

2.1 Electrode-Electrolyte Interface Properties

Impedance of the retina interface largely defines the output load of a stimulator. To guide the design of a retinal prosthesis, understanding the electrical interface properties of retina is important. Retina interface is composed of electrode-electrolyte interface and electrolyte-retina interface. Retina interface impedance can be represented by an equivalent circuit model as shown in Fig. 2.1. The model of electrode-electrolyte interface comprises an interface capacitance (C_{dl}), which is shunted by a charge transfer resistance (R_{ct}) and in series with a solution resistance (R_s) [22]. The model of electrolyte-retina interface consists of R_s and retina impedance (R_{re}) in series connection.

The nonfaradaic impedance arising from the C_{dl} is constant phase angle impedance (Z_{CAP}), which is given by the empirical relation:

$$Z_{CAP}(\omega) = \frac{1}{(j\varpi C_{dl})^n} = Y_0(j\varpi)^{-n}$$

where Y_0 equals C_{dl}^{-n}, n is a constant representing inhomogeneities in the surface and ω is angular frequency. In a Nyquist plot the angle between the data and the abscissa axes n gives according to $n=2\theta/\pi$, and n=1 represents a purely capacitive impedance element corresponding to the interface capacitance. Taken to be the series combination of the double layer capacitance and the diffuse layer capacitance, C_{dl} is in proportion to the electrode size. R_{ct} is a faradaic resistance given by the experimental relation:

$$R_{ct} = \frac{1}{J\square q} \text{ and } J = \frac{J_0 F\eta}{RT}$$

where is J the measured current density, q is the charge on the ion in the electrolyte. F is Faraday's constant, η is the applied over potential, R is the gas constant, and T is the temperature. J_0 is the equilibrium exchange current density which is composed of reduction reaction rate constant and concentration of electron-acceptor ions, etc. The resistance measured between the working electrode and the reference electrode is termed to be R_s. Under the assumption that the counter electrode is infinitely large and

the working electrode is surrounded by electrolyte, R_s can be determined from the spreading resistance which is encountered by current spreading out into solution. For a square electrode and a round electrode, the spreading resistances are given by

$$R_{s-square} = \frac{\rho \ln 4}{\pi l} \text{ and } R_{s-round} = \frac{\rho}{4r}$$

where ρ is the solution resistivity, 72 Ωcm for physiological saline, ι is the electrode side length of a square electrode and r is the radius of a round electrode.

Looking into the theoretical equations, three components of electrode-electrolyte interface impedance are all relative to electrode size. Therefore, the approximate value of retina impedance can be obtained from measurement of retinal interface impedance with muti-size microelectrodes.

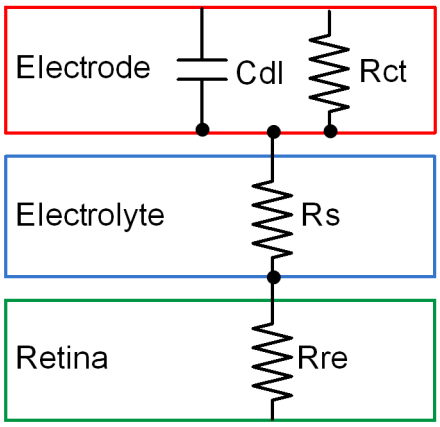

Figure 2.1 Equivalent circuit model of retina interface.

2.2 Chip Structure and Measurement Setup

2.2.1 Epiretinal Prosthesis

The electrode array pattern we designed is shown in Fig. 2.2(a). One stimulator was connected to one recorder. Electrode side length of a square stimulator, ι, is ranging from 10μm to 80μm. Electrode side length of a square recorder is 30μm which is the minimally bond-wired size of the COB apartment of IST, Inc. Separating eight kinds of ι into two groups, 10μm, 20μm, 30μm and 40μm are "small electrode set" and 50μm, 60μm, 70μm and 80μm are "big electrode set." Center-to-center return electrode to stimulating electrode distance is called "electrode distance." To confirm the relationship between different electrode distances and retina impedances, the distance between each column is ranging from 50μm to 1217μm. The detailed

description of the electrode distances between column 1 and other columns of electrodes is in Table I. Column 1 to column 15 and row A to row H are labeled in Fig. 2.2(b). Columns from left to right are defined as column 1, column 2…, to column 15; the rows from top to bottom are defined as row A, row B…, to row H. Electrode sizes of row A and row E are depicted here; ι of row A is 80μm and ι of row E is 40μm. The electrode distances of rows B, C, D are the values of the row A minus 10μm, 20μm and 30μm, respectively; the spaces of rows F G, H are the values of the row E minus 10μm, 20μm and 30μm, respectively. Whole chip layout view of multi-size microelectrode chip (microelectrode chip) is shown in Fig. 2.3, 10 columns were composed of both small and big electrode sets and 5 columns contained small electrode sets only, totally 15 columns. To sum up, 100 stimulators and relatively 100 recorders were designed as a planar microelectrode chip. The middle part of Fig. 2.3 is 1.5-mm long metal routing, connecting stimulators and recorders together. The long routing length ensures a minimum glue overflow effect. Summary of the microelectrode chip is shown in Table II. Whole chip size is 2.25mm x 1.30mm.

Table I Electrode distances of row A and row E

Row A		**Row E**	
Column	**Electrode distances (μm)**	**Column**	**Electrode distances (μm)**
2	90	2	50
-	-	3	129
4	219	4	179
-	-	5	258
6	348	6	308
-	-	7	387
8	487	8	447
-	-	9	526
10	616	10	576
-	-	11	655
12	745	12	705
13	898	13	859
14	1077	14	1077
15	1217	15	1177

Table II Summary of the microelectrode chip

SUMMARY		
Technology		Tsmc 0.35μm 2P4M
Small electrode sets	Size (ι μm x ι μm)	10 x 10 20 x 20 30 x 30 40 x 40
	Sets	15
Big electrode sets	Size (ι μm x ι μm)	50 x 50 60 x 60 70 x 70 80 x 80
	Sets	10
Total stimulators		100
Recorder size		30μm x 30μm
Whole chip size		2.25mm x 1.30mm

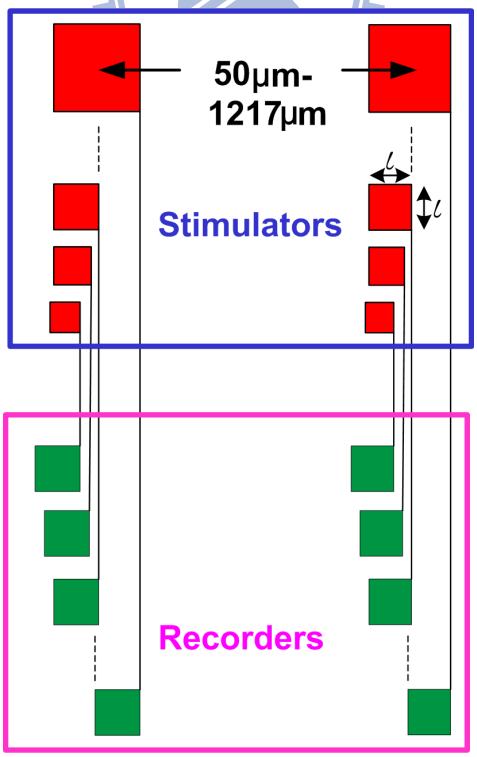

(a)

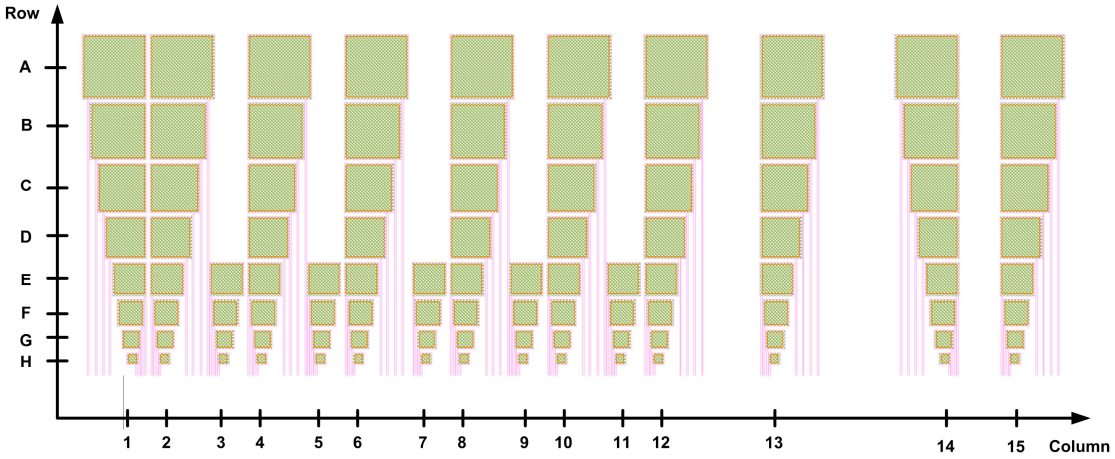

(b)

Figure 2.2 (a) Electrode array patterm and (b) array description of the microelectrode chip. Totally 8 rows and 15 columns of multi-size microelectrodes are in this chip.

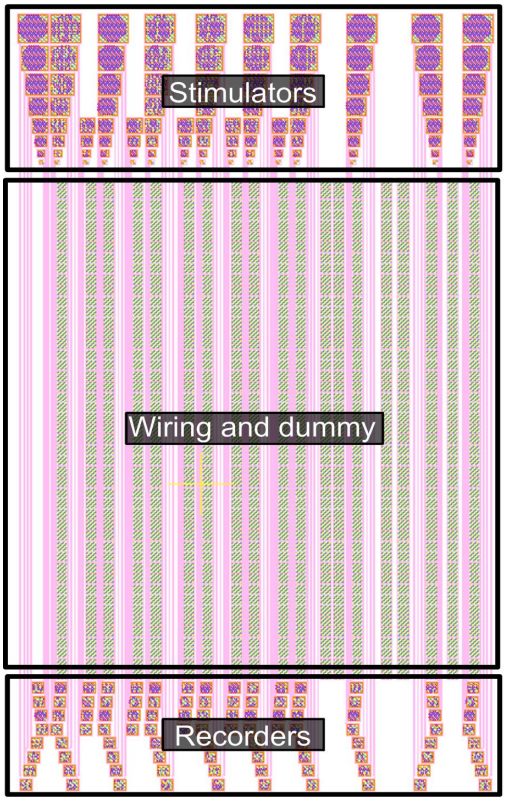

Figure 2.3 Layout view of the microelectrode chip.

2.2.2 Retina Preparation and Measurement Environment

Chip micrograph of the microelectrode chip is shown in Fig. 2.4. Whole chip size is 2.25mm x 1.30mm and metal connection between the stimulators and recorders is 1.5mm long. The space between neighboring recorders in the same column is only 1μm, which is impossible to wire-bond all 100 recorders on a PCB. Thereby we

separated the fabricated chips into two wire-bonded types because of the dense layout structure. “Big electrode chip” contains big electrode sets only, that is, columns 1, 2, 4, 6, 8, 10, 12, 13, 14, and 15 are involved. “Small electrode chip” contains small electrode sets only. The small electrode sets are even denser than the big electrode sets, so we bonded columns 1, 2, 7, 12, 13, 14, 15 in this version only. In case that electrical responses of the recorders would also stimulate the retina and result in disturbance of the measurement. Recorders of the microelectrode chips have to be sealed with black glue after bonding.

The isolated retina we used was retina tissues from adult New Zealand White rabbits (1-2 kg). The animal was anesthetized with an intramuscular injection of 1:1 mixture of ketamine (50mg/ml) and xylazine (20mg/ml). A local anesthetic (proparacaine hydrocholoride; 2-3 drops) was been applied to the eye before intraocular injection of 4’, 6-diamidino-2-phenylindole (DAPI, 2μg; Sigma, St. Louis, MO). The animal was allowed to recover. The deeply anesthetized animal will be euthanized with overdose of anesthetic or 100% CO_2. One day after DAPI injection, the animal was dark-adapted for at least one hour before dissection. The animal was deeply anesthetized again for isolating the retina. Hemi-sectioned in oxygenated (95% O_2 and 5% CO_2) Ames’ medium, each eye was removed and the retina was dissected out from the sclera and carefully peeled off the pigment epithelium.

At the beginning of the experiment, we put a self-made recording chamber on the wire-bonded microelectrode chip and poured in some balanced salt solution (BSS) to ensure biocompatibility of the retina. Then the prepared retina was cut into a small piece (diameter<5mm) and moved into the chamber. We pressed down the retina to the microelectrode chip by weights of a filter paper as shown in Fig. 2.5(a). To measure interface retina impedance, we used an impedance analyzer (4294A, Aglient, Inc) as shown in Fig. 2.5(b) to probe the impedance between a stimulating electrode and a return electrode. Two wires of the wire-bounded microelectrode chip were connected to the probe of impedance analyzer.

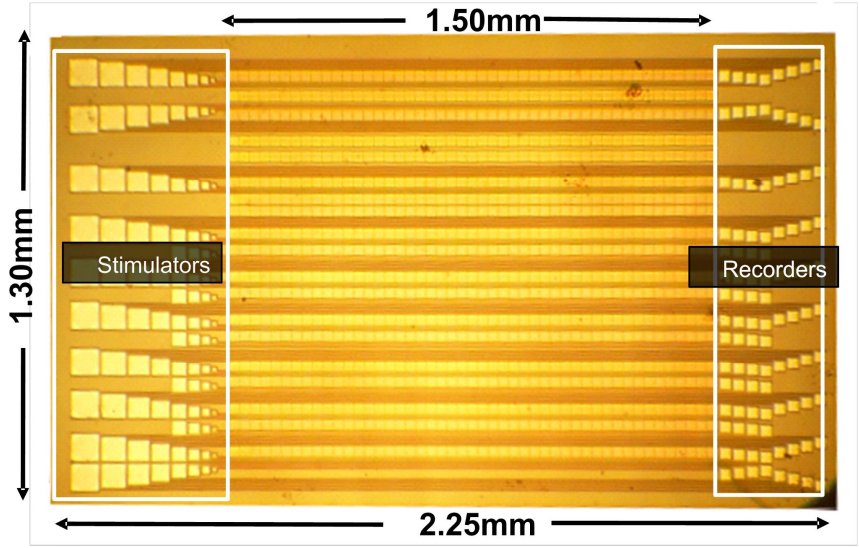

Figure 2.4 Chip micrograph of microelectrode chip. Whole chip size is 2.25mm x 1.30mm. Metal connection between the stimulators and recorders is 1.5mm long.

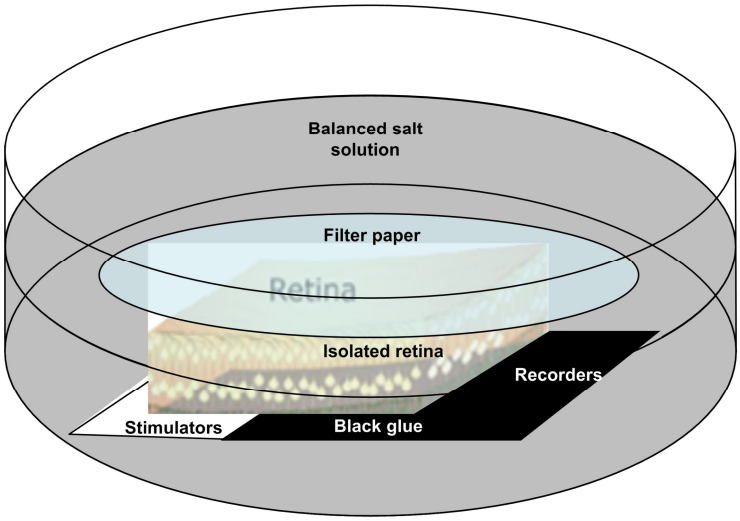

(a)

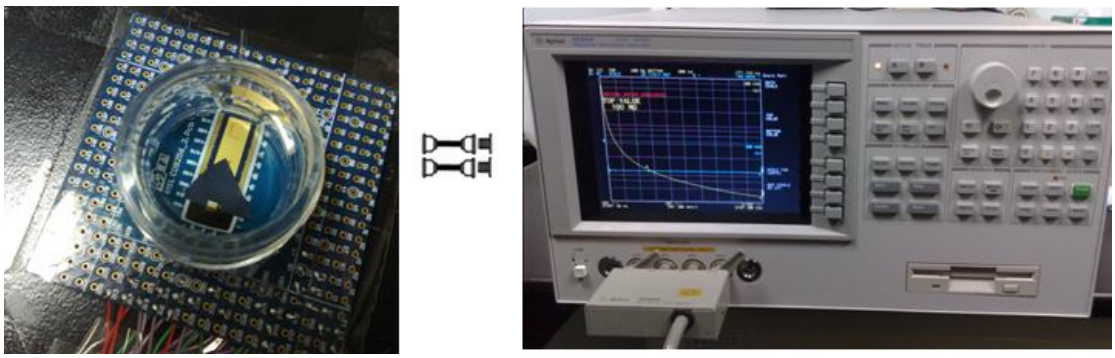

(b)

Figure 2.5 (a) Shematic of measurement setup for measuring retina interface impedance. (b) Photograph of impedance recording. Two wires of the wire-bounded microelectrode chip were connected to the probe of impedance analyzer.

2.3 Measurement Results and Discussion

In the measurement of retina interface impedance, one end of the probe of impedance analyzer was fixed at column 1 of the wire-bonded recorder as the other end moved from column 2 to column 15 to measure interface impedances of different electrode distances. Experiments were done on row A to row H to measure the impedance of multi sizes of electrodes. Frequency bandwidth was between 40Hz and 100kHz with 201 recording points. AC signal was sine wave with 500 mV magnitude, and no DC bias potential was included. The measurement results of frequency to impedance curve are shown in Fig. 2.6. Randomly choose data number 1, 5, 10, 20, 40, 80, 120, 160 and 201 totally 9 points from the recorded points. Frequency and impedance axes are in logarithm scale. Figure 2.6(a) shows the impedance between column 1 and column 6 of the big electrode chip; Fig. 2.6(b) shows the impedance between column 1 and column 7 of the small electrode chip. In each figure, the smaller electrodes have larger impedance at low frequency. But 10-μm and 40-μm side length electrodes did not yield consistent results, so these sizes were not included in Fig. 2.6(b). The impedance of small electrode sets was not always larger than big electrode sets, because these two kinds of sets were separated into two chips. Therefore, in the following analysis, we studied the results of big electrode chip only. Besides the impedance between column 1 and column 2 and between column 1 and column 15 of the big electrode chip, other columns yielded consistent results, so these columns were not included in further analysis. These problems may come from that retina did not and very closely attach to the chip thus the measurement results were not very reliable at the two ends of microelectrode chip. In this case, large contact resistance (R_{co}) was shown in the retina interface that would disturb the measurement results.

Looking into the relationship between retina interface impedance and electrode distance, we compared the relationship of row C at low frequency and at high frequency. Figure 2.7(a) shows the electrode distance to impedance curve at low frequency (40Hz, 0.5kHz, 1kHz and 1.5kHz); Fig. 2.7(b) shows the electrode distance to impedance curve at high frequency (25kHz, 50kHz, 75kHz and 100kHz). No consistent electrode distance to impedance relationship at low frequency, whereas impedance increases with increasing electrode distance at high frequency. These results indicate that the impedance modulus is not highly dependent on R_{co} at high frequency. Suggesting that C_{dl} was shunted with R_{co}, Z_{CAP} was smaller than R_{co} at

high frequency and thereby R_{co} didn't domain the interface impedance.

In other studies, electrochemical impedance spectroscopy (EIS) has been used to electrically characterize the retina interface, but the analyzing process acquired from EIS is complicated. The benefit of using an equivalent model is to develope a better understanding of the physical processes occurring at the biomedically relevant interface. Therefore, a curve fitting tool of the MATLAB was used in this work to analyze the approximate value of C_{dl}, R_{ct}, R_s and R_{re}. To simplify the equation, we grouped R_s and R_{re} into tissue resistance (R_u). From Fig. 2.1, the equivalent equation of retina interface is composed of magnitude portion and phase portion:

$$Magnitute = \sqrt{[\frac{R_{ct}}{1+(2\pi f \bullet R_{ct} \bullet C_{dl})^2} + R_u]^2 + [\frac{2\pi f \bullet {R_{ct}}^2 \bullet C_{dl}}{1+(2\pi f \bullet R_{ct} \bullet C_{dl})}]^2}$$

$$Phase = \tan^{-1}\left\{\frac{2\pi f \bullet {R_{ct}}^2 \bullet C_{dl}}{R_{ct} + R_u \bullet [1+(2\pi f \bullet R_{ct} \bullet C_{dl})^2]}\right\}$$

Using the magnitude portion as the general model and defining the range of three elements can fit a frequency to impedance curve. Three elements can be found by the tool as three constants. Thus the magnitude of impedance is the function of frequency. Figure 2.8 shows the fitted R_{ct} and C_{dl} results of big electrode sets. A large variance (about 10%) was in the fitted results as we analyzed each element by curve fitting tool rather than EIS. For most of the electrode distances, R_{ct} increases with decresing electrode size and C_{dl} increases with increasing electrode size. R_{ct} and C_{dl} are not relative to electrode distances. To obtain $R_{re,}$ we subtracted R_s from R_u. Figure 2.9(a) shows the calculated results of R_s by using the formula in section 2.1. R_s of different electrode distances were viewed as a constant. Figure 2.9(b) shows the fitted R_{re} results of big electrode sets. For most of the electrode sizes, R_{re} increases with increasing electrode distance. But the value of R_{re} for a smaller size of electrode was less than a bigger one; this fact was opposed to our prediction. We predicted that a bigger size of electrode would contact with bigger retinal area, and the resistance of bigger area is less. However, since large R_{co} was in the interface between retina and microelectrode chip, the relationship between R_{re} and electrode size was not correct. Therefore, contact between retina and microelectrode chip has to be improved by the weight of heavier stuff than filter paper (e.g. cover glass). Therefore, most amount of stimulation current would flow into the tissue without the bad influence of R_{co}.

Even though the fitted results were not very ideal, defining an approximate range of retina interface impedance is still capable. According to the analyzed results of different electrode distances and multi sizes, three elements were summarized in Table

III. R_{re} is about 10kΩ to 200kΩ, where as C_{dl} is about 0.01nF to 1nF and R_{ct} is about 1MΩ to 100MΩ for big electrode sets. Comparing to the work done by Humayun et al. [22], with similar electrode sizes (50μm side and 50μm diameter), electrode distances (745μm and 800μm), and measurement environment, our results are very similar to theirs. In our work and in [22], C_{dl} is 0.031nF and 0.033nF; R_u is 32kΩ and 74kΩ, respectively. The comparison between [22] and this work is depicted in Table IV.

Table III Fitting results of retina interface impedance of big electrode sets

Elements	**Electrode distance (μm)**	**ι (μm)**			
		80	**70**	**60**	**50**
R_{ct} (MΩ)	1077	5.800	5.860	20.500	29.900
	745	3.750	3.900	5.360	84.900
	487	2.300	3.990	4.130	12.000
C_{dl} (nF)	1077	0.201	0.192	0.073	0.014
	745	0.135	0.107	0.080	0.031
	487	0.736	0.168	0.153	0.087
R_{re} (kΩ)	1077	95.869	95.312	51.395	16.616
	745	166.329	152.962	96.905	25.566
	487	93.169	84.962	78.345	13.426

Table IV Comparison of Humayun et al. in 2007 [22] and this work

	Humayun et al., 2007 [22]	**This Work**
Animal tissue	Porcine eye	Rabbit eye
Electrode type	Polyimide thin-film	Aluminum
Recorder type	Thin-film platinum	Aluminum
Electrode size & shape	50μm diameter round electrode	50μm side square electrode
Electrode distance	800μm	745μm
Vitreous gel replacement	Balanced salt solution (BSS)	Balanced salt solution (BSS)
Frequency bandwidth	10Hz to 100kHz	40Hz to 100kHz
Measuring instrument	Commercial potentiostat (FAS1, Gamry, Inc)	Impedance analyzer (4294A, Aglient, Inc)
AC signal	10 mV sine wave	500 mV sine wave
DC signal	No DC bias Potential	No DC bias Potential

C_{dl}	0.033nF	0.031nF
R_u	74kΩ	32kΩ

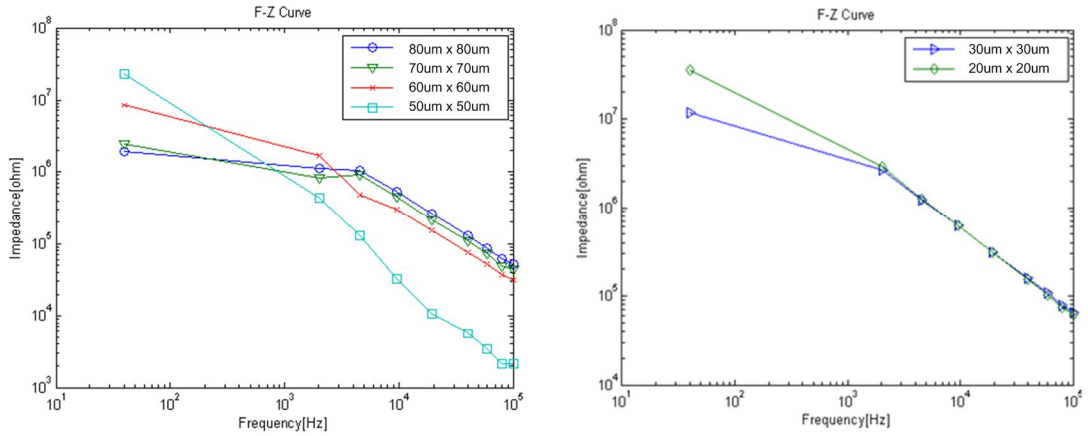

(a) (b)

Figure 2.6 Frequency to impedance curve of (a) big electrode sets and (b) small electrode sets. The electrode distance between 80μm x 80μm electrodes is 348μm; the space between 30μm x 30μm electrodes is 387μm.

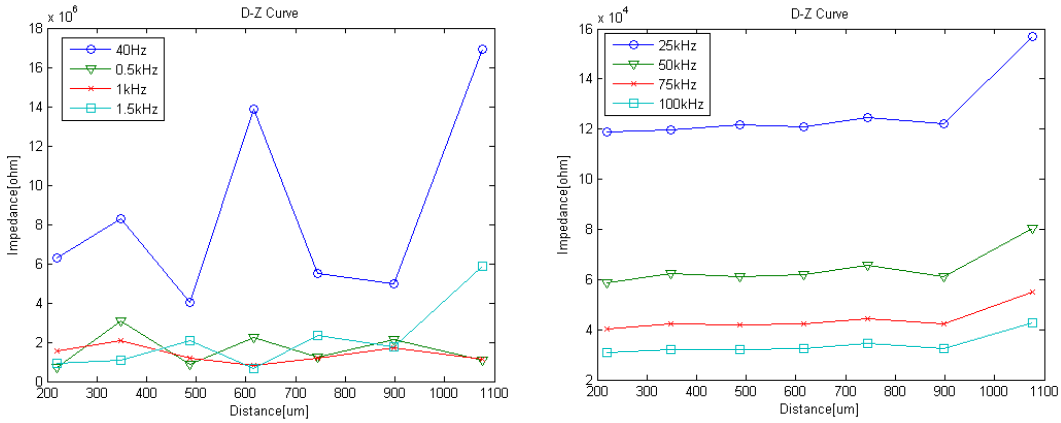

(a) (b)

Figure 2.7 Distance to impedance curve of 60-μm side length electrodes. Measuring frequency is at (a) 40Hz, 0.5kHz, 1kHz and 1.5kHz (b) 25kHz, 50kHz, 75kHz and 100kHz.

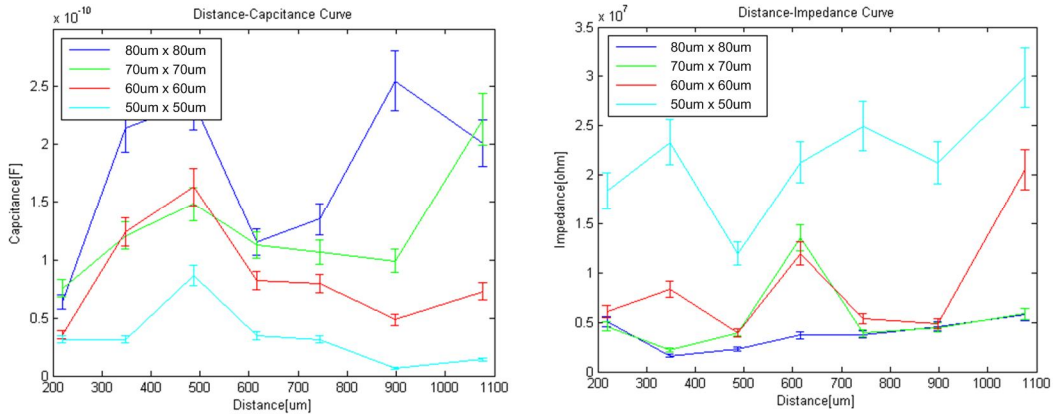

(a) (b)

Figure 2.8(a) Distance to impedance (R_{ct}) curve of big electrode sets (b) distance to capacitance (C_{dl}) curve of big electrode sets.

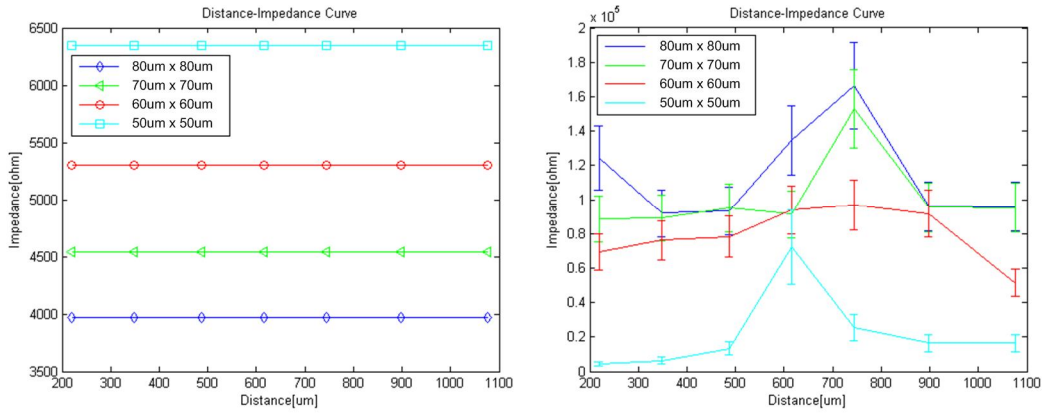

(a) (b)

Figure 2.9(a) Distance to resistance (R_s) curve of big electrode sets (b) distance to resistance (R_{re}) curve of big electrode sets.

CHAPTER 3 Solar Cell Array for Efficient Subretinal Stimulation

3.1 Chip Structure

3.1.1 Solar cell and photodiode structure

A photodiode can convert sunlight directly into electricity. When photons of sufficient energy enter a photodiode, they can create an electron-hole pair in the conduction band, producing a current which travels against diode polarity. This current is called the "photocurrent," and can forward bias the diode, producing a so-called "photovoltage." The photovoltage and photocurrent can be utilized to drive a passive load; in this case the cell is operating photovoltaically. It is sometimes desirable to place an external bias voltage across the photodiode; in this case the cell operates photoconductively. In both photovoltaic and photoconductive systems photocurrent is proportional to incoming light intensity. The linear conversion of light into current makes a photodiode an attractive data delivery option. Photovoltaic circuits, which are composed of solar cells, can also be used to deliver electrical power. A photodiode-based (passive) retinal prosthesis may employ either photovoltaic or photoconductive circuits. In the simplest photoconductive design, a bias voltage is provided to a photodiode in series with the retinal tissue load. In the simplest photovoltaic design, a single photodiode, which is so-called "solar cell," directly drives current into the retina. This approach does not require an external power supply, as each pixel generates current without a bias.

Cross-sections of P+/N-Well solar cells with floating P-substrate in 0.35μm 2P4M technology are proposed in Fig. 3.1. If solar cells are not connected in series, then each solar cell is called single solar cell (SSC). As light irradiates a SSC, if P+ has low voltage (LV) and N-Well is connected to stimulating electrode, then the SSC can directly drive high stimulation current (HI) into a passive load. If N-Well has LV and P+ is connected to a passive load, then anode has high voltage (HV) and the SSC can drive the load with photovoltage. Solar cells can not deliver power to CMOS circuits in this technology, because P-Substrate is usually connected to ground when solar cells and NMOS are in parallel connection. Nonfloating P-Substrate will results in the

leakage current problem of parasitic-BJT as shown in Fig. 3.2.

Photocurrent generated from a passive device could barely stimulate the retina if the output load is too large. Solar cells in series connection have higher photovoltage and thus the stimulation current is larger than those without series connection. Besides, with high photovoltage, solar cells can deliver higher voltage supply to CMOS circuits. To solve the problem depicted in Fig. 3.2, solar cells can be built in the deep N-Well (DNW) of 0.18μm 1P6M technology. The cross-sections of two N+/P-Well solar cells in series connection are proposed in Figure 3.3. P-substrate is kept floating to reduce the parasitic-BJT problem. If two solar cells are connected in series, then each pair of solar cells is called two cascode solar cells (TSC). As light irradiates a TSC, if P-Well has LV and N+ is connected to stimulating electrode, then the TSC can directly drive HI into a passive load. If N+ has LV and P-Well is connected to a passive load, then anode has HV and the TSC can drive the load with photovoltage. The photovoltage of a TSC is twice of a SSC.

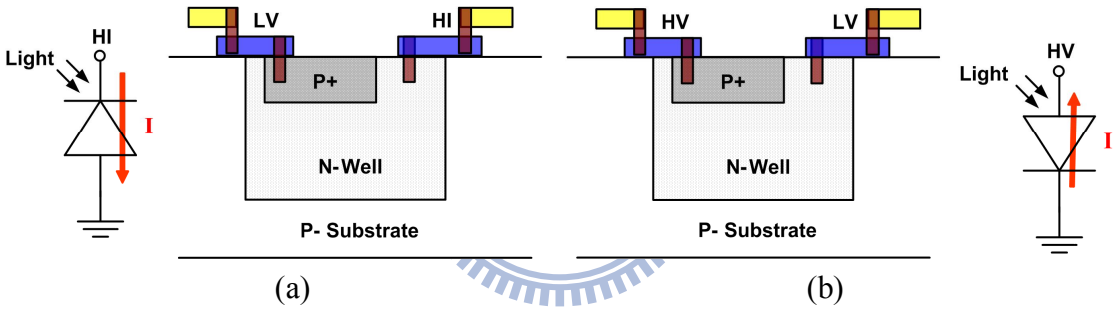

Figure 3.1 Cross-sections of P+/N-Well solar cells with floating P-Substrate in 0.35μm 2P4M technology. The functions are driving passive loads with (a) photocurrent and (b) photovoltage.

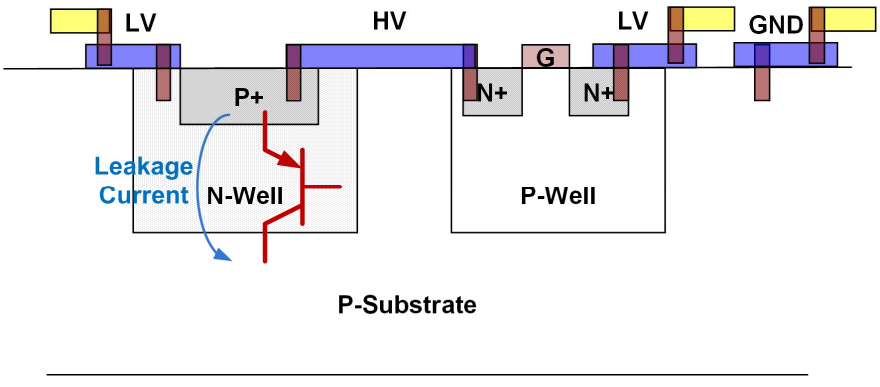

Figure 3.2 Cross-section of P+/N-Well solar cell and NMOS in parallel connection in 0.35μm 2P4M technology. Leakage current is induced by parasitic BJT from nonfloating P-Substrate.

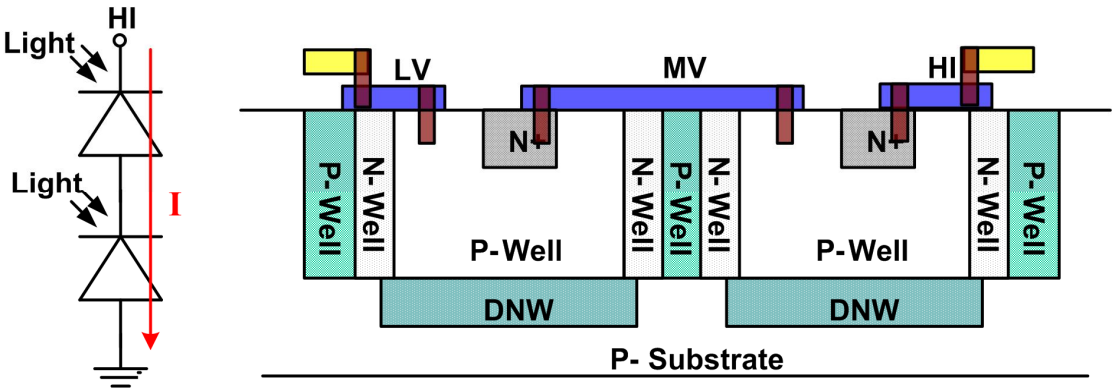

(a)

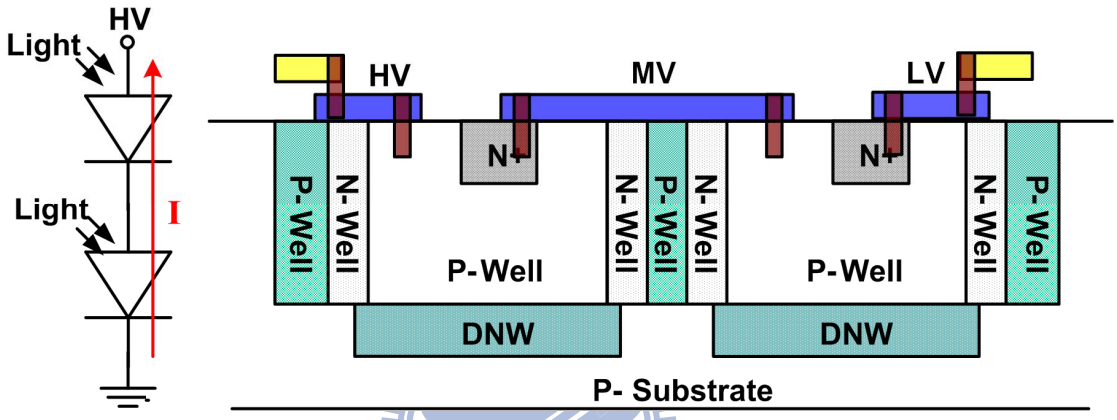

(b)

Figure 3.3 Cross-sections of two N+/P-Well solar cells in series connection with floating P-Substrate in 0.18μm 1P6M technology. The functions are driving passive loads with (a) photocurrent and (b) photovoltage.

3.1.2 Single and two cascode solar cell array stimulation chips

To increase retinal stimulation current, either photo-sensing region of a solar cell has to be enlarged or many solar cells have to be connected in parallel. According to [25], a solar cell with 4 times photo-sensing regions of a 5μm x 5μm solar cell can only generate about 2 times photocurrent under same light intensity. Based on the cross-sections of Fig. 3.1, the layout view of two P+/N-Well solar cells in parallel connection is shown in Fig. 3.4. The diffusion area and space between each cell is 5μm x 5μm and 1.1μm, respectively. The layout view of single solar cell array stimulation chip (SSCA stimulation chip) is shown in Fig. 3.5. SSCA stimulation chip was composed of 16-pixel SSCA. Each pixel was composed of a solar cell array (SCA) and two ends of SCA were connected to a stimulating electrode and a return electrode.

SSCA was composed of 2540 SSCs in parallel connection. The stimulating electrode was placed in the middle part of the pixel and was surrounded by SSCs. SSCA of each pixel was surrounded by local surrounding return electrode. The dummy metals surrounded whole pixels were cut off four corners for biocompatibility. The summary of the chip is shown in Table V. Implantable SSCA stimulation chip was fabricated in tsmc 0.35μm 2P4M technology. Whole chip size is 2.45mm x 2.45mm.

In order to increase the voltage supply, we connected two solar cells in series to provide twice photovoltage based on the cross-section of Fig. 3.3. Figure 3.6 shows the layout view of two cascode N+/P-Well solar cells connected in parallel. Building solar cells in the DNW takes a lot of area and the space between two N-Wells has to be larger than 5μm, so we enlarged the diffusion area and space between each cell to 10μm x 10μm and 14.1μm, respectively. The layout view of two cascode solar cell array stimulation chip (TSCA stimulation chip) is shown in Fig. 3.7. TSCA stimulation chip is composed of 1-pixel TSCA. Each pixel is also composed of a TSCA. TSCA is composed of 414 TSCs in parallel connection. The stimulating electrode is placed in the middle part of the pixel and is surrounded by TSCs. TSCA of each pixel is surrounded by local surrounding return electrode. The summary of the chip is shown in Table VI. Implantable TSCA stimulation chip was fabricated in tsmc 0.18μm 1P6M technology. Whole chip size is 0.976mm x 0.962mm.

In our past design, the return electrodes of all pixels were connected together and placed far from the stimulating electrodes. Output load of a stimulator increases with decreasing electrode size and increasing return electrode to stimulating electrode distance as mentioned in the previous chapter. Thereby the return electrode of each pixel was designed to be surrounding around whole SCA. Each pixel with its own local return electrode rather than sharing the same return electrode or placing the return electrode in a remote place decouples electric fields of neighboring electrodes and decreases cross-talk and interference [22]. Therefore, in a confined stimulation region, spatial resolution of pixel array should be better. However, we have no ideal whether this return electrode design could enhance subretina stimulation efficiency or not, so simulation on the current distribution in the retina of SCA has to be done.

Table V Summary of the SSCA stimulation chip

SUMMARY	
Technology	Tsmc 0.35μm 2P4M

Power supply voltage	No external power supply
Photo-sensing area per solar cell	5μm x 5μm
Solar cell number per pixel	2540
Exposured electrode	75μm x 75μm
Photosensing area per pixel	388μm x 388μm
Pixel size	495μm x 495μm
Pixel number	4 x 4 pixels
Chip size	2450μm x 2450μm

Table VI Summary of the TSCA stimulation chip

SUMMARY	
Technology	Tsmc 0.18μm 1P6M
Power supply voltage	No external power supply
Photo-sensing area per solar cell	10μm x 10μm
Solar cell number per pixel	414 x 2
Exposured electrode size	75μm x 75μm
Photosensing area	754μm x 754μm
Pixel size	930μm x 930μm
Pixel number	1 pixel
Chip size	976μm x 962μm

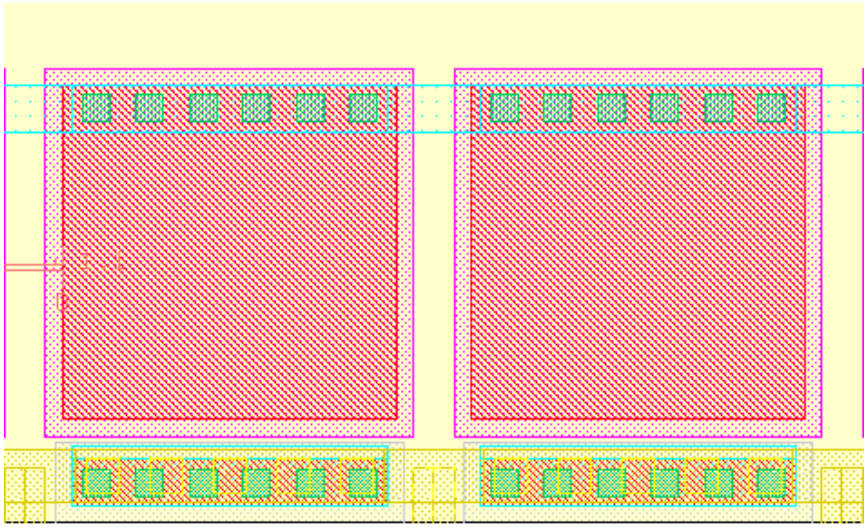

Figure 3.4 Layout view of two SSCs in parallel connection.

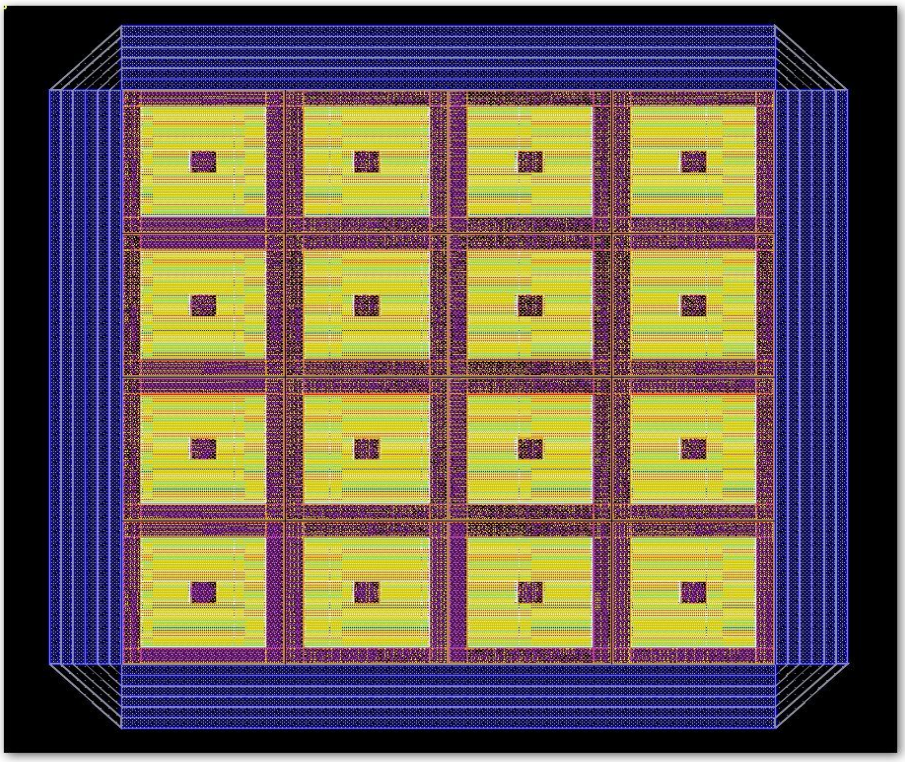

Figure 3.5 Layout view of SSCA stimulation chip. Whole chip size is 0.976mm x 0.962mm.

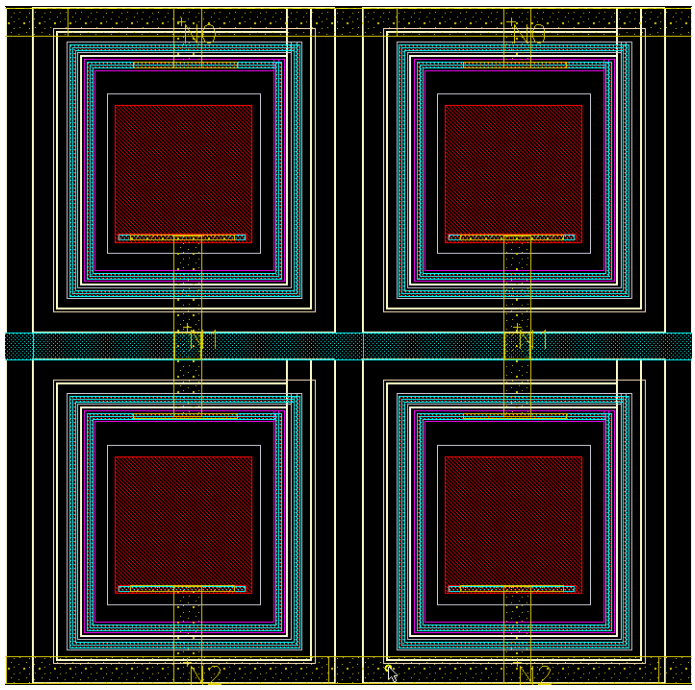

Figure 3.6 Layout view of two TSCs in parallel connection. Solar cells are built in the DNW.

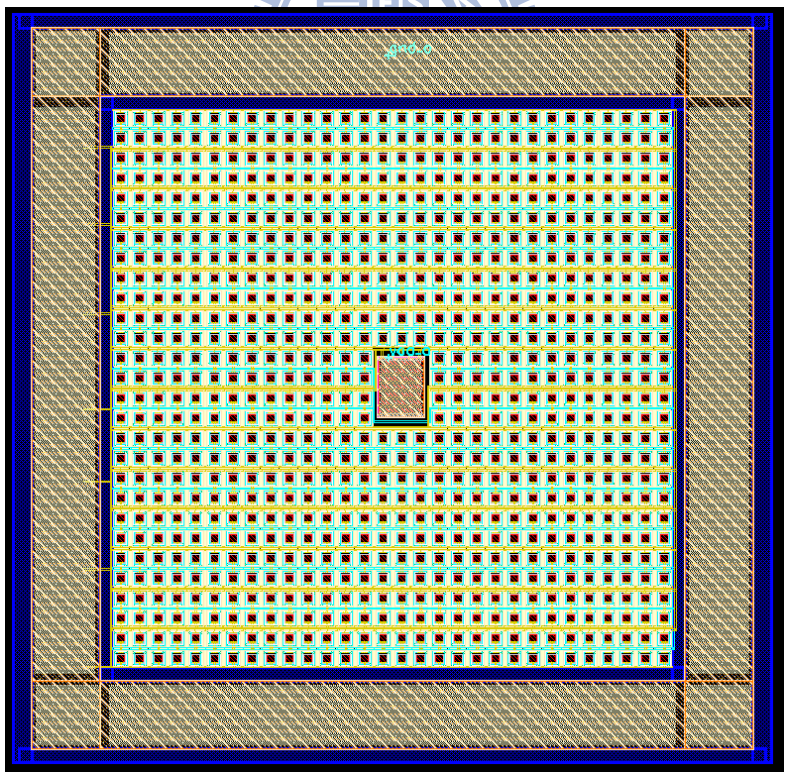

Figure 3.7 Layout view of TSCA stimulation chip. Whole chip size is 0.976mm x 0.962mm.

3.2 Simulation Results

Regardless of circuit specifics, prosthesis pixels interface with the body through microelectrodes. When SCA is implanted beneath the pigment epithelial layer (PRL) as shown in Fig. 3.8, three main layers are expected to be stimulated: photoreceptor layer, horizontal/bipolar layer and ganglion cell layer. Each layer can be viewed as 2-dimensional spreading resistive network; three layers can be viewed as 3-dimension (3D). In order to simulate current distribution in the retina and to evaluate which kind of return electrodes is the best one for SCA, 3D spreading resistive network model, as shown in Fig. 3.9, has to be involved in the simulation of retinal stimulation current. SCA directly drives current to the retina from the return electrode to the stimulating electrode.

The surfaces of three main layers of retina are defined as layer 1, layer 2 and layer 3. Layer 1 is closest to the SCA. Impedances of each layer are thought to be equal. Retina layers are composed of many thick resistance and surface resistance. Thick resistances of each layer are R_{t1}, R_{t2} and R_{t3}, respectively. Surface resistance can be considered as a resistive matrix which consists of column resistance and row resistance. Column resistances of each layer are R_{c1}, R_{c2}, and R_{c3}, respectively. Row resistances of each layer are R_{r1}, R_{r2}, and R_{r3}, respectively. A set of resistance is composed of 9 resistances (R_{t1}, R_{t2}, R_{t3}, R_{c1}, R_{c2}, R_{c3}, R_{r1}, R_{r2} and R_{r3}). From previous measurement results, we define R_{ti} to be 10kΩ, R_{ci} to be 1MΩ and R_{ri} equals R_{ci}, where $_i$ represents 3 different layers. Assuming that the stimulating electrode of SCA attaches to 3 x 3 sets of resistances and the retinal tissue is composed of 256 x 256 sets of resistances. Stimulation current flows from the stimulating electrode to the return electrode. Potential of the return electrode is represented by ground. Figure 3.10 shows the simplified schematic of the first tissue layer. The resistances are represented by the lines between two intersections to better understand the relationship among different positions. Elements of the matrix are named by x-coordinate and y-coordinate. Origin of the coordinates locates on the middle point of the matrix, and it is also middle point of the stimulation site and probe region. Stimulation site is where the stimulating electrode attaches to the retina; 3 x 3 nodes surrounding the origin of the resistive network are involved. We probed the current passing through R_{ti}, and probe region involves 5 x 5 nodes surrounding the stimulation site of the resistive network.

In addition to the proposed local surrounding return electrode in this work, there

are two other kinds of return electrodes as shown in Fig. 3.11. One is remote surrounding return electrode which is far away from the stimulation site in ring shape. The other one is remote single return electrode which is also far away from the stimulation site in square shape. Electrode distance of local return is 2 columns, which is very close to the stimulation site; whereas electrode distance of remote return is 128 columns. Single remote return is at the position (-128, 0).

The simulation model of each solar cell in the circuit is established based on the previous experimental results. As strong light irradiates a 5μm x 5μm solar cell, generated photocurrent is about 10nA [25] as shown in Fig. 3.12(a). In the simulation, we shunted a current source near a solar cell to be the generated photocurrent as shown in Fig. 3.12(b). In comparison of which design of return electrodes can stimulate higher current at retina tissue, we probed the current passing through Rt1. Simulation results of one pixel of SSCA stimulation chip with three different kings of return electrodes are shown in Fig. 3.13. With 25.4μA photocurrent, current in the stimulation site, i.e. (-1, -1), (-1, 0), (-1, 1), (0, -1), (0, 0), (0, 1), (1, -1), (1, 0), (1, 1), taking the major portion of the generated photocurrent. The minimum current in the stimulating area is at the (0, 0); the maximum current (Imax) is at the four corner, because the equivalent resistance at the latter node is lower than the former node. Imax of the remote single return structure is 101.1nA; Imax of the remote surrounding return structure is 344.7nA; Imax of the local surrounding return structure is 1085.4nA. The Imax of local surrounding return is 10 times of remote single return structure and 3 times of remote surrounding return structure. Thereby SCA with local surrounding return electrode has higher current efficiency than other return electrode designs.

The simulation method of TSCA is similar with SSCA. Because the photo-sensing region of each solar cell of TSC is four time larger than SSC, we assumed the zero bias photocurrent of each solar cell is 40nA as shown in Fig. 3.14 (a); then 414 TSCs can generate 16.56μA photocurrent. In the simulation, we shunted a current source near the solar cells as the generated current in Fig. 3.14(b). Simulation results of TSCA with three different kings of return electrodes are shown in Fig. 3.15. Imax of the remote single return structure is 217.1nA; Imax of the remote surrounding return structure is 697.5nA. Imax of the local surrounding return structure is 1917.8nA. The Imax of local surrounding return is 10 times of remote single return structure and 3 times of remote surrounding return structure. These ratios are very similar with SSCA. Even though the current generated from the SSCA is 1.5 times larger than the TSCA, the stimulation current of the latter is twice larger than the former, because

photovoltage of the latter is twice larger than the former. Thereby TSCA with local surrounding return electrode is more current efficient than SSCA. Stimulation current not only changes with different return electrode designs but also decreases with the depth of retinal layer for both SSCA and TSCA. Figure 3.16 shows the SSCA simulation results of stimulation current passing through three different retina layers with different return electrode designs. No matter what kind of return electrode is, stimulation current decreases 1.5 times with increasing retina layers if impedance of each layer is the same.

The quantity of solar cells decides the electrode distance. More solar cells generate more stimulation current but also result in farer electrode distance. To find the optimum value of solar cells with local surrounding return electrode, simulation on various quantities of solar cells is made. We pretended that SSCA or TSCA covers 256 x 256 retina impedance sets. Then electrode distance of 2540 SSCs or 414 TSCs is equivalent to 128 impedance sets. To make these two solar cell numbers more relate to electrode distance, we viewed them as 18 times and 3 times of 128, that is, 2304 and 384. If the decreasing ratio of electrode distance to solar cell number is 1:1, then for electrode distances 64, 48, 32, 16, 4, the solar cell numbers of SSCA approximate to 1152, 864, 576, 288, 72, respectively, whereas for TSCA approximate to 192, 144, 96, 48, 32, respectively. Figure 3.17 shows electrode distance to current curves of SSCA and TSCA, and maximum current occurs at electrode distances 32 columns and 64 columns, respectively. Simulation on various quantities of solar cells was also made. Figure 3.18(a) shows solar cell numbers to current curve of SSCA and TSCA. Maximum currents occur at 576 and 192 solar cells, respectively. Figure 3.18(b) shows photo-sensing region to current curve of two SCA, Optimum photo-sensing regions are 14400μm^2 and 19200μm^2 and maximum stimulation currents are 36.8nA and 60.6nA for SSCA and TSCA, respectively. Current stimulation efficiency of TSCA is 1.65 times larger than SSCA with the optimum photo-sensing region.

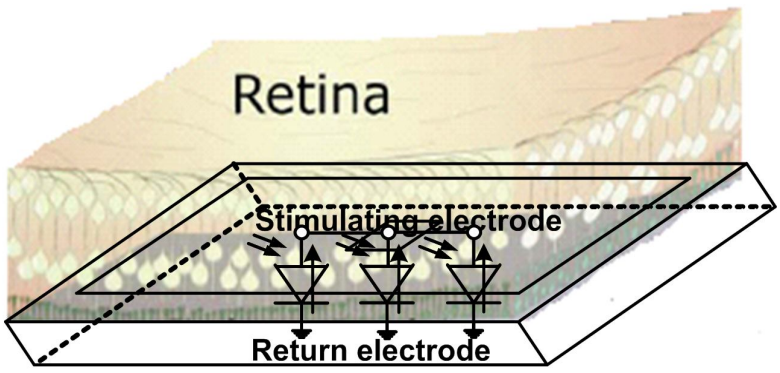

Figure 3.8 Schematic of a SCA implanted beneath the PRL.

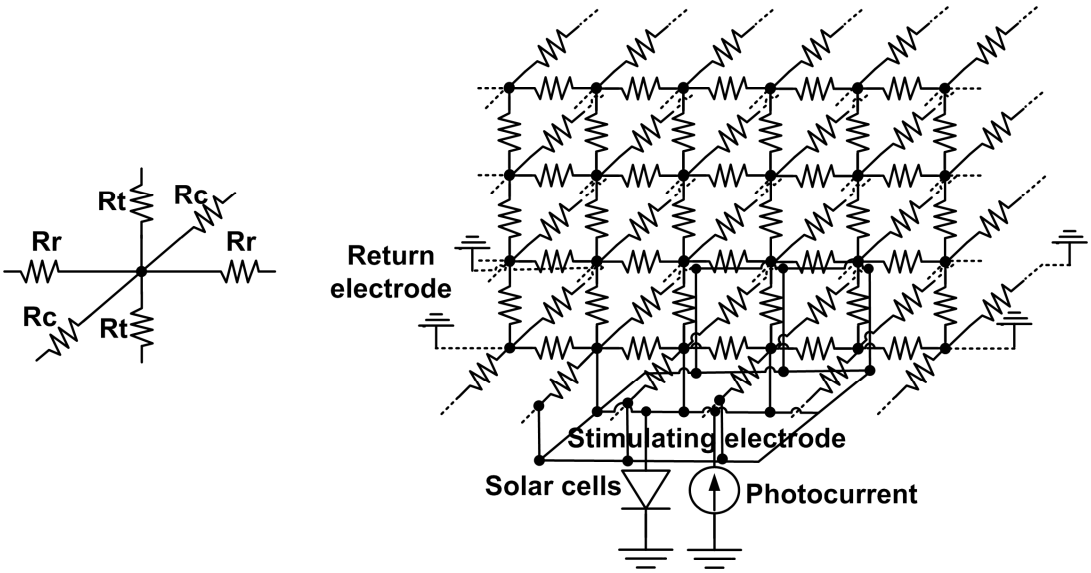

Figure 3.9 Schematic of the 3D spreading resistive network model. Thick, column and row resistances are represented by R_t, R_c, and R_r, respectively.

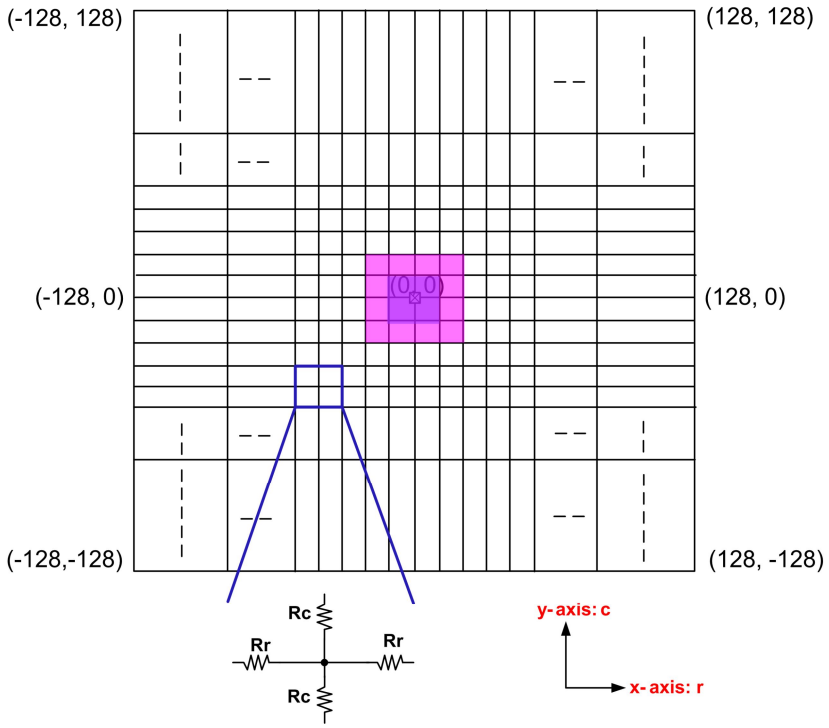

Figure 3.10 Schematic of the first layer of the retinal tissue. The retinal tissue we assumed is composed of 256 x 256 sets of resistances. The middle point of the matrix is at (0, 0). Stimulation site is labeled by the smallest square, 9 sets of resistances are included in a stimulating electrode. Probe region is labeled by the bigger square, 25 sets of resistances are included in the probe region.

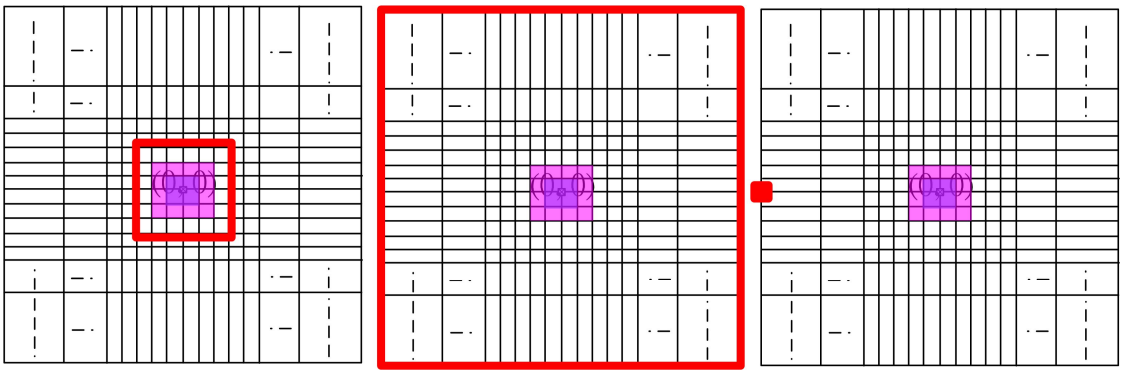

(a) (b) (c)

Figure 3.11 Three different kinds of return electrodes: (a) local surrounding return electrode, (b) remote surrounding return electrode and (c) remote single return electrode.

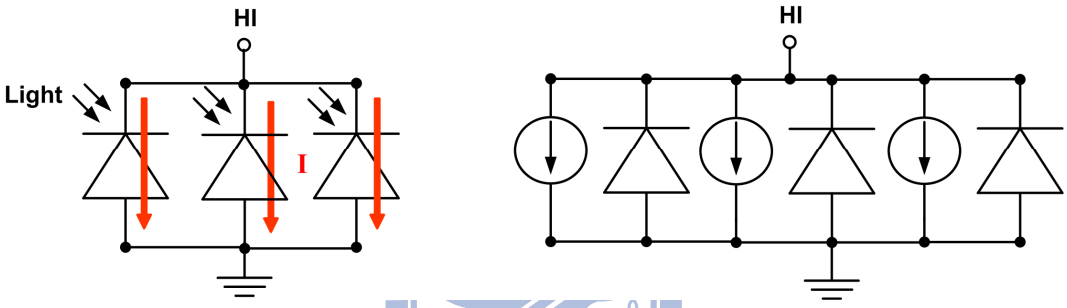

(a) (b)

Figure 3.12 (a) Illumination model and (b) simulation model of P+/N-Well solar cells. P+ with LV is connected to ground and N-Well with HI is connected to retina tissue.

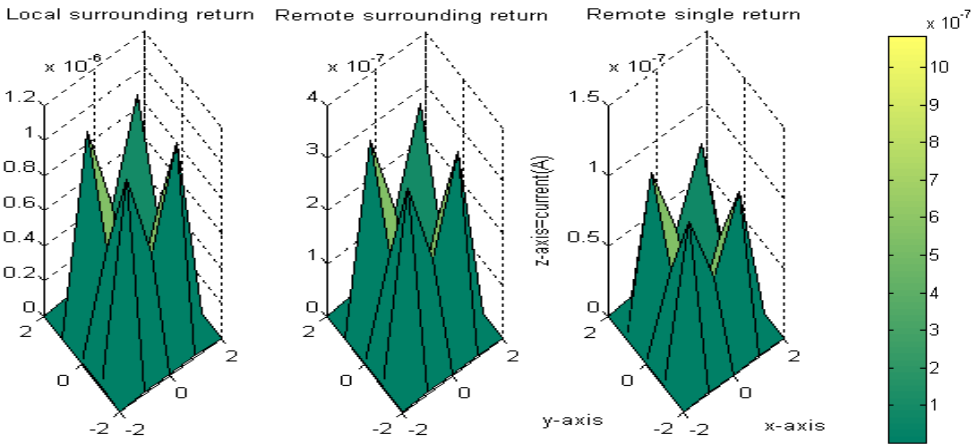

(a) (b) (c)

Figure 3.13 Simulation results of stimulation current of three different return electrode designs in SSCA: (a) local surrounding return, (b) remote surrounding return, and (c) remote single return.

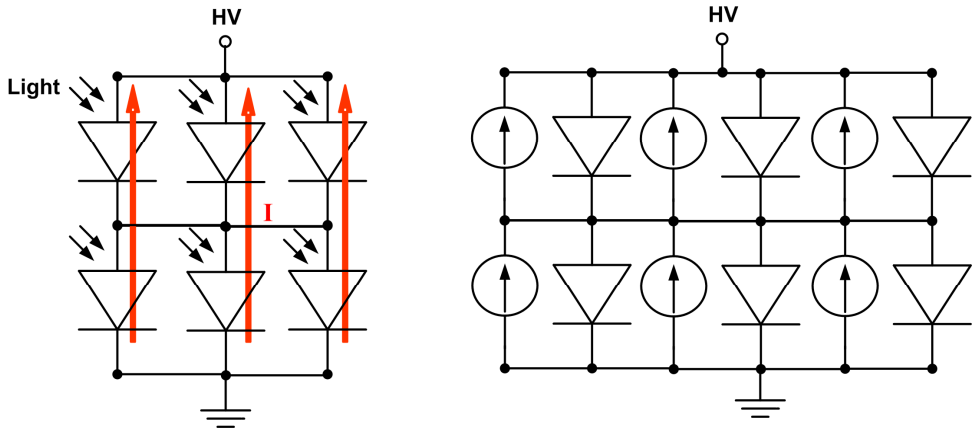

(a) (b)

Figure 3.14 (a) Illumination model and (b) simulation model of two cascode N+/P-Well solar cells. N+ with LV is connected to ground and P-Well with HV is connected to retina tissue.

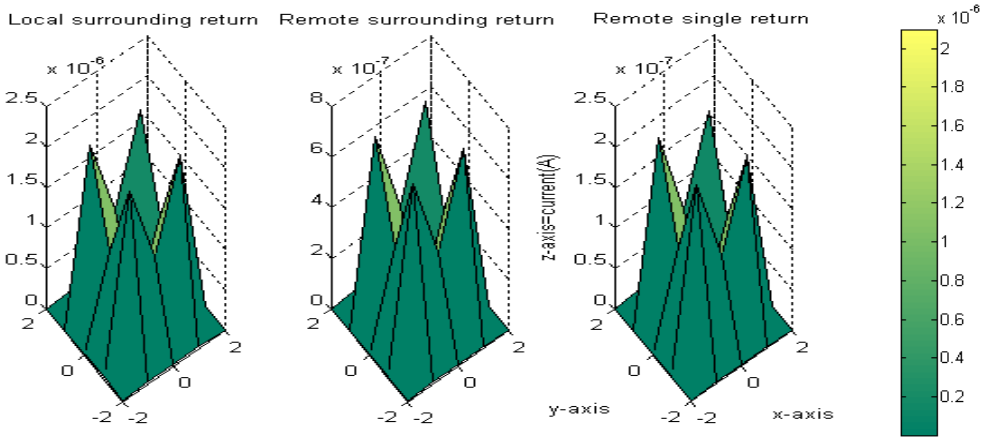

(a) (b) (c)

Figure 3.15 Simulation results of stimulation current of three different return electrode designs in TSCA: (a) local surrounding return, (b) remote surrounding return, and (c) remote single return.

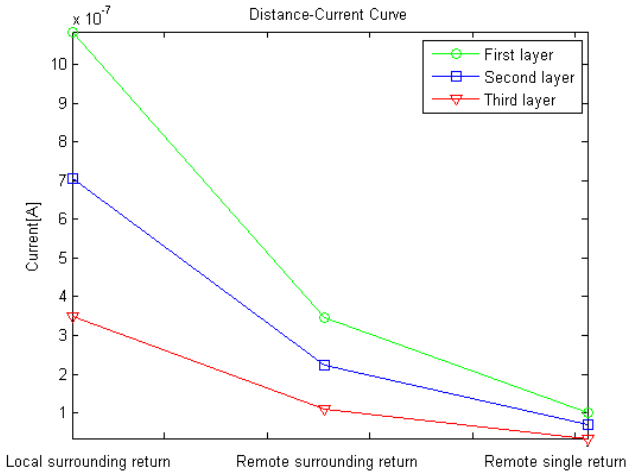

Figure 3.16 SSCA simulation results of stimulation current to different return electrode design curves of three different retina layers.

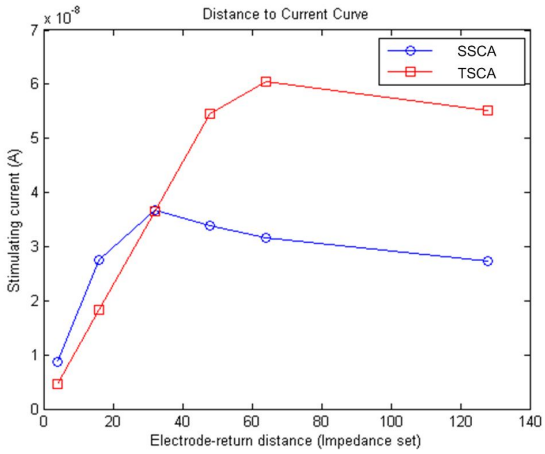

Figure 3.17 (a) Electrode distance to current curves of SSCA and TSCA. Maximum current occurs at electrode distances 32 and 64, respectively.

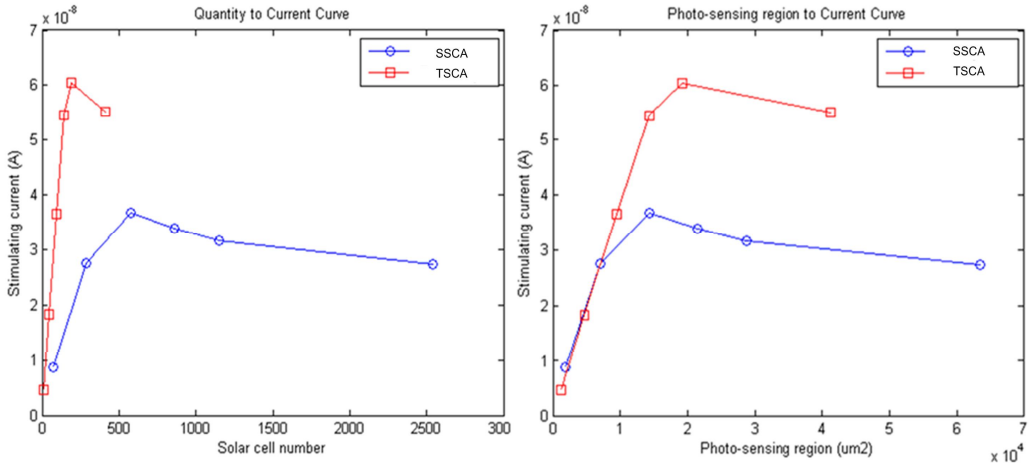

Figure 3.18 (a) Solar cell numbers and (b) Photo-sensing region to current curves of SSCA and TSCA. Maximum current (36.8nA and 60.6nA) occurs at solar cell numbers of 576 and 192 and photo-sensing regions of 14400μm^2 and 19200μm^2 for SSCA and TSCA, respectively.

3.3 Measurement Results

Chip micrographs of single pixel of SSCA and TSCA stimulation chips are shown in Fig. 3.19, and pixel sizes are 495μm x 495μm and 930μm x 930μm, respectively. To measure the output current of the SSCA, we bonded 2 electrodes of each pixel, totally 4 pixels of a chip were bonded on a PCB. Three chips were bonded for

measurement. To measure the output current of the TSCA, 2 electrodes of each pixel were bonded. Totally 8 chips were bonded on PCBs for measurement.

Figure 3.20 shows the measurement setup of this experiment. The light source of this experiment, which set up on the microscope, was 532nm laser. Output power of the light source was tuned to be 1mW, 5mW, 10mW, 20mW, 50mW, 100mW and 200mW, totally seven kinds. Stimulus pulse duration is 10ms. Microscope stage of a fluorescence microscope (Axioskop 2 FS Plus, Zeiss, Germany) was used to better understanding the illuminated location. In order to measure the photocurrent generated from solar cell array, we used auto-ranging Picoammeter to probe the output current while solar cell array was under various laser power illumination.

Since the diameter of laser beam is only 30μm with less than 150μm divergence, illuminating area is too small to cover whole pixel, we separated SSCA to four regions and illuminated them separately. In each pixel, we probed two photo-sensing regions (photo1 & 2), one electrode one ground region. Charge density can be calculated from the equation of the charge density:

$$\frac{Q}{A} = \frac{I_{photo} \times t_{duration}}{A_{electrode}}$$

where A is the electrode size; t is the duration time of the pulse, and I is the output photocurrent. Figure 3.21 shows the measurement results of the average output current and charge density of SSCA under various output power of laser light. Illuminating photo-sensing regions results in higher stimulating level than electrode or ground regions. For 1-mW laser power, output charge densities are 135μC/cm^2, 137μC/cm^2, 164μC/cm^2 and 50μC/cm^2 for electrode, photo1, photo2 and ground regions, respectively. Light illumination of photo-sensing region can result in larger photocurrent. In the measurement of TSCA, we illuminated photo2 region only. Figure 3.22 shows the measurement results of the average output current and charge density of TSCA under various output power of laser light. For 1-mW laser power, output charge density is 2.73μC/cm^2 for photo2 region.

Measurement environment of Fig. 3.23 was to probe the I-V curve of these chips. With 632.8nm He-Ne laser light sources, the I-V curves can be probed by the HP4145B parameter meter. The measurement results of output current per photo-sensing region are shown in Fig 3.26. Zero biased currents per photo-sensing region of SSCA and TSCA are 1.93nA/μm^2 and 0.66nA/μm^2, respectively. The open circuit voltage is 0.4-0.5V and 0.8-1.0V for two structures. SSCA has 3 times current but only half voltage of TSCA.

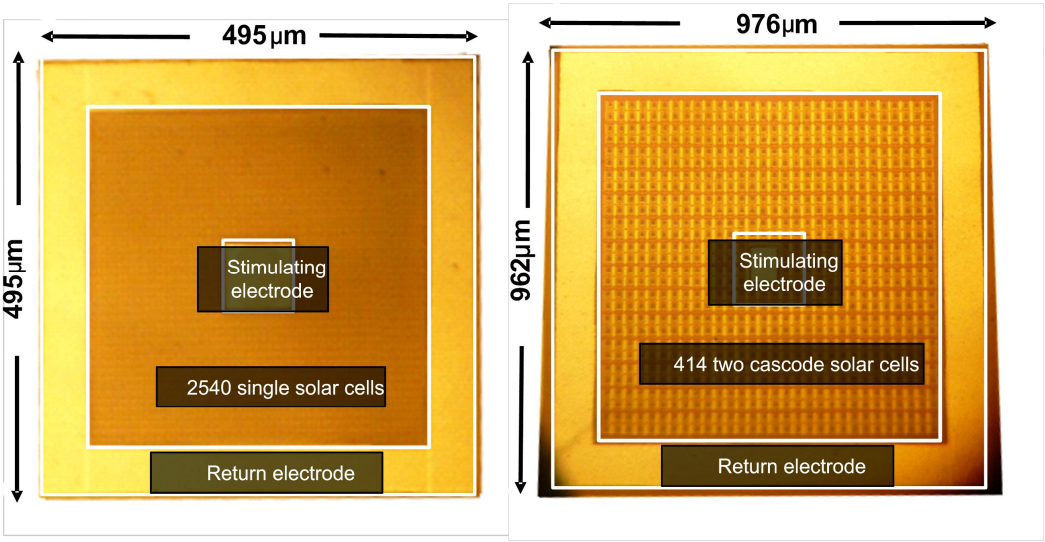

(a) (b)

Figure 3.19 Chip micrographs of one pixel of (a) SSCA and (b) TSCA stimulation chips.

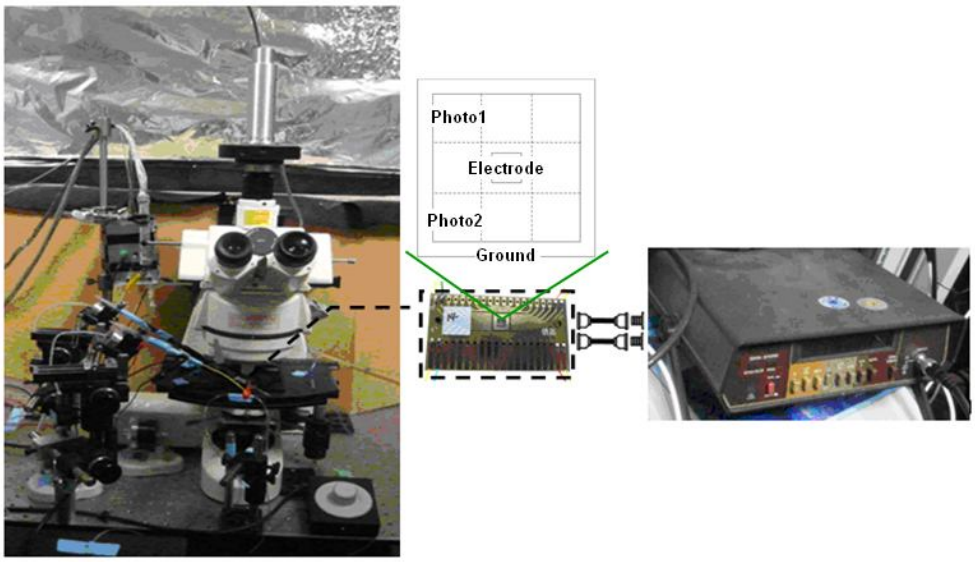

Figure 3.20 Measurement environment of the output current of SCA. The left part is a microscope with 532nm laser light source. The chip in the middle part is placed on the stage of the microscope. The left part is an auto-ranging Picoammeter.

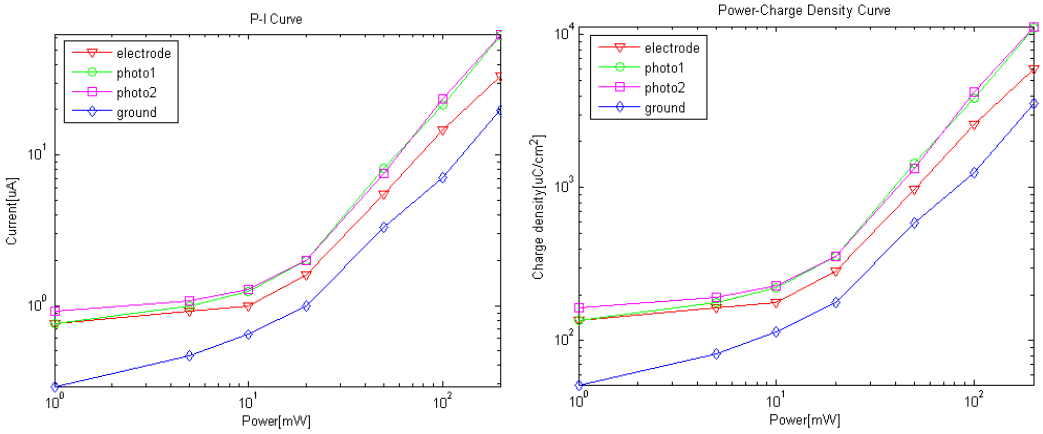

(a) (b)

Figure 3.21 Measurement results of the (a) output current and (b) charge density of SSCA under various power of laser light source.

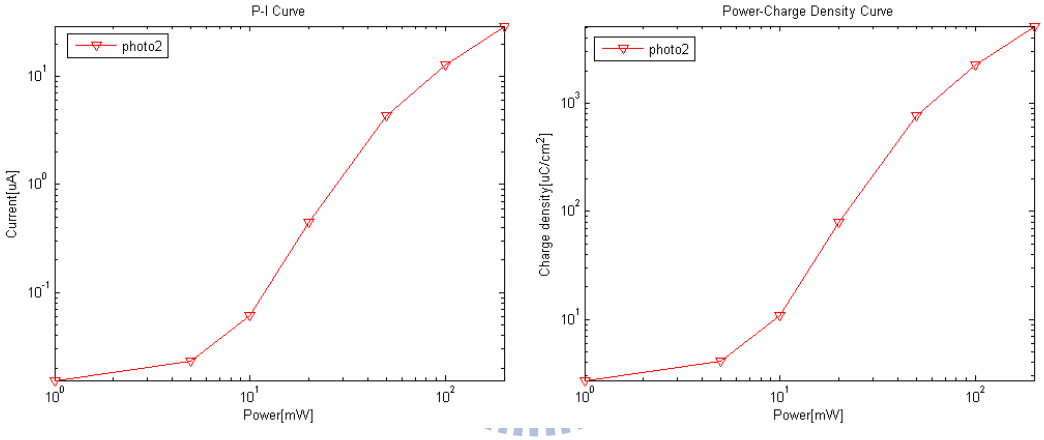

(a) (b)

Figure 3.22 Measurement results of the (a) output current and (b) charge density of TSCA under various power of laser light source.

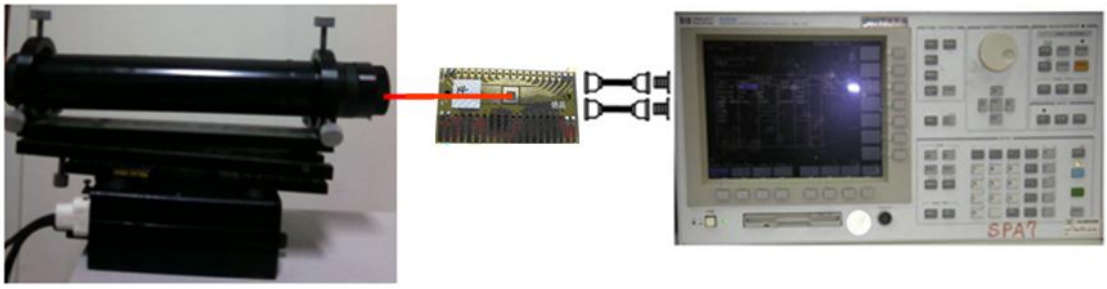

Figure 3.23 Measurement environment of the IV curve. The left part is He-Ne laser light sources; the middle part is the chip setup middle, and the right part is the HP4145B parameter meter.

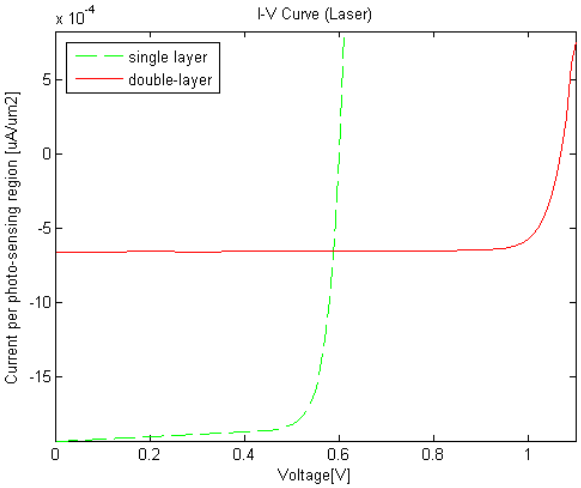

Figure 3.24 Measurement results of the I-V curves of SSCA and TSCA stimulation chips under He-Ne laser light source.

3.4 In Vitro Experimental Results

The SSCA stimulation chip was used in the in vitro experiment of subretinal prosthesis. Preparation method of the isolated rabbit's retina is the same as mentioned in section 2.2.2. A small piece of retina had to be cut off from the isolated retina first. The stimulating chip was placed beneath the PRL of isolated retina. The retina was closely attached on the chip by filter paper and then moved to a custom-made recording chamber attached to a fluorescence microscope, which amplifying ratio is 40. All procedures were carried out under green laser (532nm) illumination as in Fig. 3.25 to provide frequency and intensity controllable light source [26]. Membrane potentials were extracellular recorded from individual retina ganglion cell (RGC) bodies in the ganglion cell layer (GCL) with a tungsten-in-glass electrode (tip size, 30-40μm; resistance, ~1 MΩ). The ON and OFF alpha RGC used in this in vitro experiment are shown in Fig. 3.26. Each RGC is about the size of four pixels of the SSCA stimulation chip. Signals were amplified, filtered, and fed into a differential amplifier (ISO-80, WPI). The analog inputs were converted into digital signals using a PC computer equipped with the data acquisition (DAQ) device (National Instrument, Texas, USA). The signals were also displayed on an oscilloscope for observation and fed into an audio amplifier for monitoring spikes. The operation of extracellular recording was controlled by custom-written software (LabView). Off-line analysis was carried out using the MATLAB (The MathWorks).

To look into the efficiency of the electrical response of the retinal stimulation chip, we have to eliminate the light response of the RGC. Figure 3.27 shows the responses of RGC before and after light bleaching protocol. After bleaching, RGC had no response to CRT light and laser light. Laser light voltage used here is 1mV and the duration is 100ms. Even at higher power of laser (100mW) the RGC still had no response, so RGCs have no response to light anymore. The responses occurred in later works can ascribe to electrical stimulation and the electrically evoked response from RGC was due to stimulation of presynaptic neuron.

In attention to know if the threshold of RGCs is correlated with electrical stimulation locations and their cell soma locations on the SSCA stimulation chip, we probed several locations as shown in Fig. 3.28(a). Illuminated location was same as the probed location. Figure 3.28(b) shows that threshold charge densities of different regions, except the outside region, thresholds have no much difference; therefore, RGC response threshold does not correlate with its illuminated and soma location on the chip. We can summarize from Fig.3.21 that the charge densities of 1-mW to 20-mW laser power are as small as the ground region and 50mW to 200mW are as big as photo2 region, that is, charge densities of 1mW, 5mW, 10mW, 20mW, 50mW, 100mW, 200mW are 50μC/cm^2, 82μC/cm^2, 114μC/cm^2, 178μC/cm^2, 1333μC/cm^2, 4213μC/cm^2, 11324μC/cm^2, respectively.

For a retinal stimulation chip, strength of electrical stimulation is mainly controlled by light intensity and stimulating frequency. Figure 3.29 shows one term of many recorded signals of both ON and OFF alpha RGCs for 10 trails (5 trails on the left and 5 trails on the right, top to bottom in sequence) and recording time is 1 second. Light source in this experiment is 1-mW laser and stimulus duration is 10ms. For the ON alpha RGC, every trail was responded while only 8 trails were responded for the OFF alpha RGC. Therefore, the percentages of responded trails are 100% and 80%, respectively. There are many spikes responded; the first spike latency for each type is 50ms and 90ms. Electrically evoked responses were recorded from totally 18 RGCs (11 OFF RGCs and 7 ON RGCs). During various experiments some RGCs could not be identified conclusively due to poor light-evoked responses.

RGCs were 50% activated upon equivalent charge density of the electrical stimulation less than 50μC/cm^2 under 1mW power of laser (8cd/cm^2 light intensity). Therefore, electrical stimuli successfully trigger the RGCs with threshold charge of 2.8nC with a 75μm x 75μm stimulating electrode. The averaging results are shown in Fig. 3.30. The relationship between electrical stimulation strength and RGC responses indicates that higher equivalent charge intensity doesn't mean more responses, but

first spike latency of ON alpha RGC would slightly decreases with increasing intensity. Spike number of RGC response showed a rise-and-fall pattern with increasing intensity.

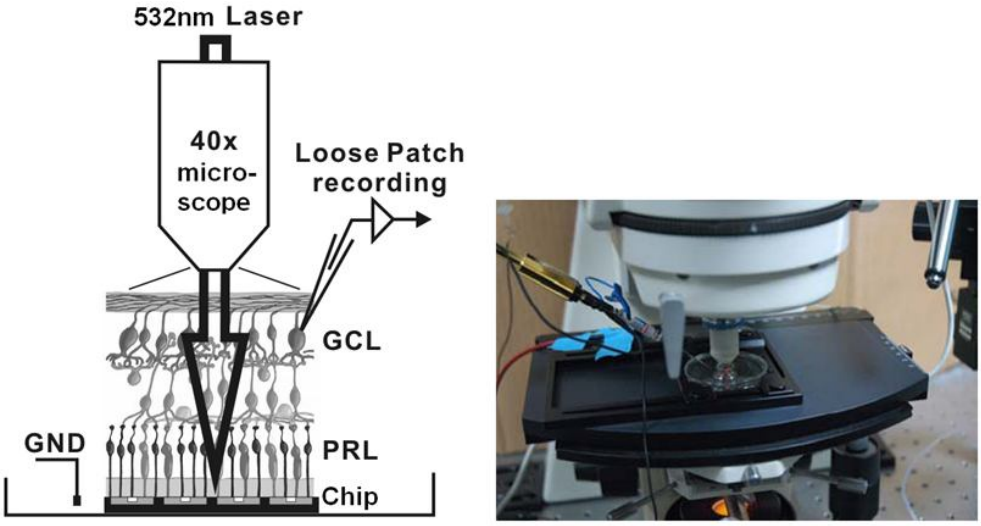

(a) (b)

Figure 3.25 Schematic and a photograph of the measurement environment. Light source is 532nm laser, amplifying ratio of microscope is 40, the stimulating chip is placed beneath the PRL of isolated retina, and recording the signal from a loose patch on the ganglion cell layer (GCL).

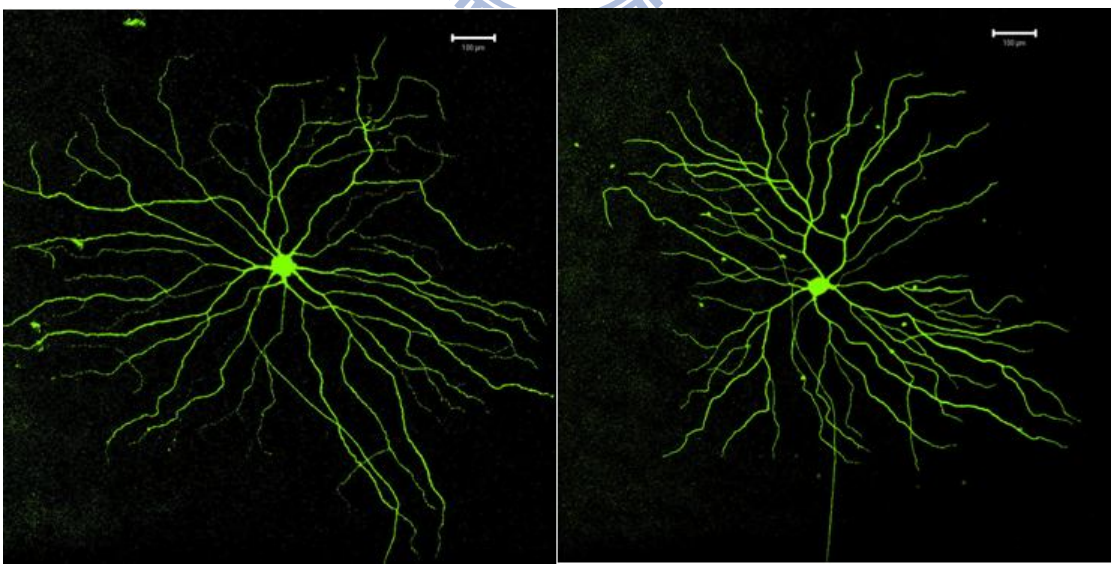

(a) (b)

Figure 3.26 Photographs of (a) ON alpha RGC; (b) OFF alpha RGC. White bar represent 100um and the size of this ganglion cell is about 1.2mm. These pictures are reprinted from NTHU Y.T. Yang.

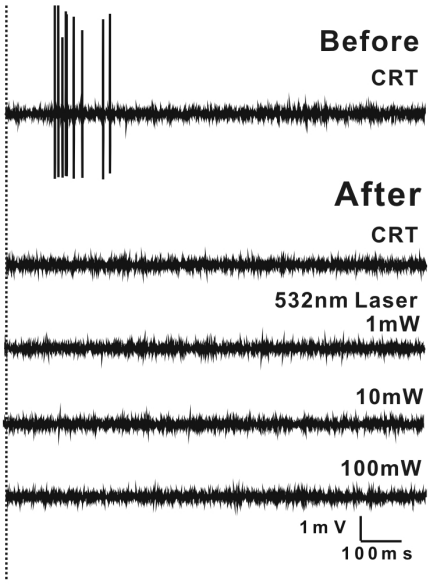

Figure 3.27 Responses of RGC before and after the light bleaching protocol.

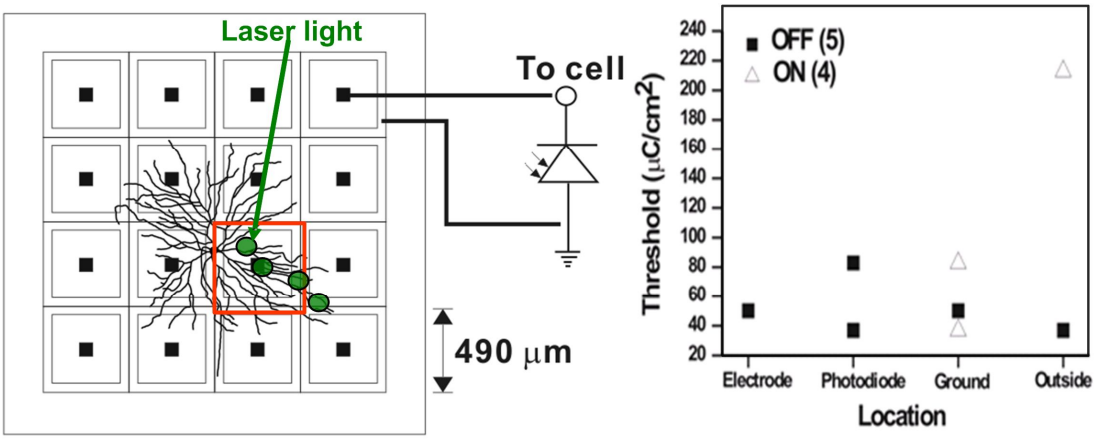

(a) (b)

Figure 3.28 (a) Cell soma locations on the SSCA stimulation chip and (b) relationship between the threshold of RGCs upon electrical stimulation and their locations.

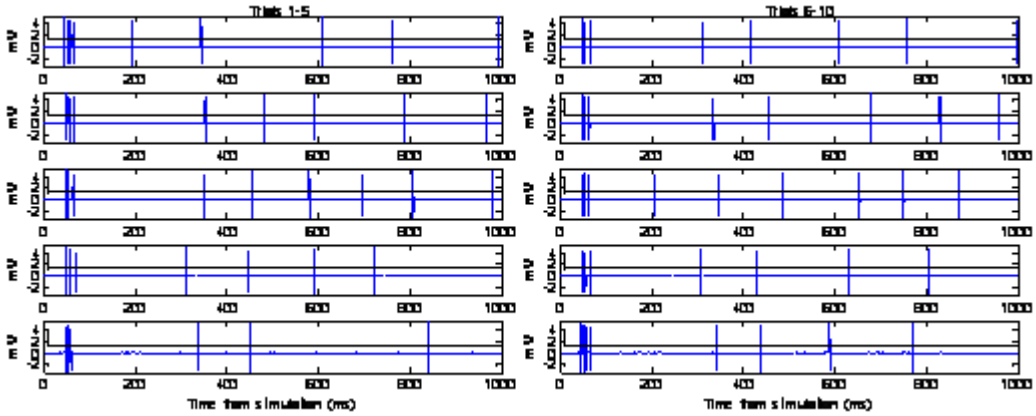

(a)

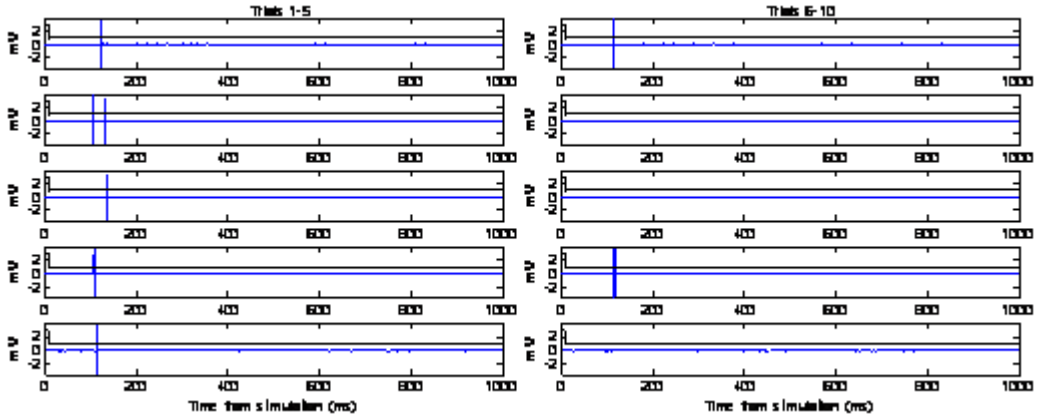

(b)

Figure 3.29 Recorded signals of (a) ON alpha RGC and (b) OFF alpha RGC for 10 trails, 1000ms. Light source is 1-mW laser and stimulus duration is 10ms.

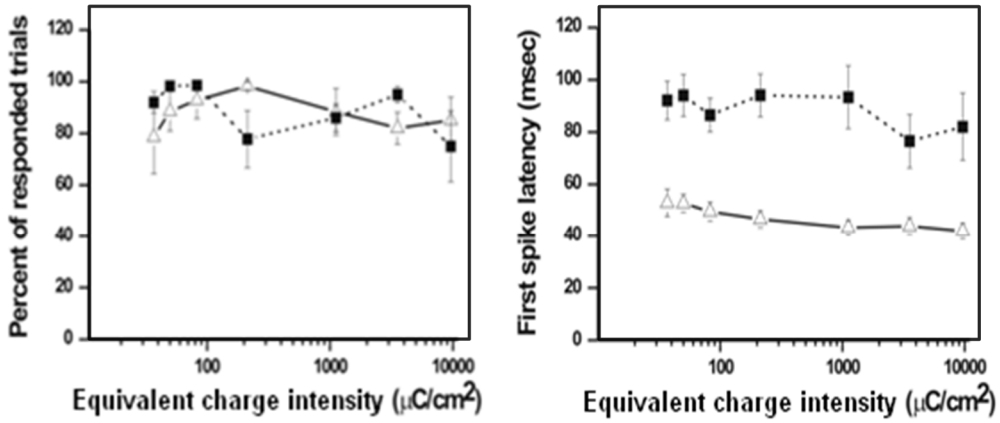

(a) (b)

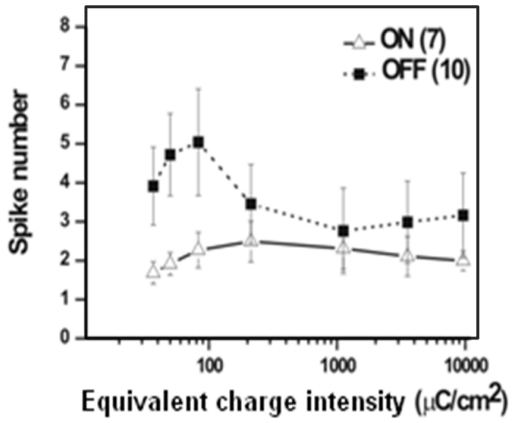

(c)

Figure 3.30 Relationship between electrical stimulation strength and RGC responses of (a) percent of responded trails, (b) first spike latency and (c) spike number.

3.5 Conclusions

From the simulation results of 3D spreading resistive model, stimulation current of SSCA with local surrounding return electrode is 1.08μA, which is 10 times of remote surrounding return and 3 times of remote single return. Stimulation current of TSCA is 2.09μA, which is 2 times more current efficient than SSCA. With local surrounding return electrode, optimum solar cell numbers of SSCA and TSCA are 576 and 192; optimum photo-sensing regions are 14400μm^2 and 19200μm^2, and maximum stimulation currents are 36.8nA and 60.6nA for SSCA and TSCA, respectively. Current stimulation efficiency of TSCA is 1.65 times larger than SSCA with the optimum photo-sensing region.

From the measurement results, the solar energy had transfer to electrical energy. SSCA with a 75μm x 75μm stimulating electrode can generate charge density from 50$\mu C/cm^2$ to 11324$\mu C/cm^2$ with a laser light source which output power was adjusted from 1mW to 200mW. In vitro experimental results indicate that we have verified the functionality of the electrical stimulation from the retinal stimulation chip. The electrical stimulation strength of a retinal stimulation chip is mainly controlled by light intensity. Electrical stimuli could successfully trigger the RGCs with threshold charge of 2.8nC with a 75μm x 75μm stimulating electrode of SSCA under light intensity 10 times larger than room light. The threshold charge multiplies stimulating electrode size (TCME) of this work is 15.8 $\mu C \cdot \mu m^2$.

TCME can be viewed as a figure of merit for the subretinal stimulation chip and this value is the smaller the better. Since it is easier to trigger the retina cells, if the threshold charge is small, and the electrode size is expected to be small for the scale-down chip size. Table VII shows the comparison of several subretinal studies with this work. Gekeler and Stett used 4 x 2 100μm side square microelectrode array to stimulate rabbit's RGC with a stimulus generator [27]. The threshold charge is about 2 times larger and TCME is over 3 times larger than this work. Jensen and Rizzo used stimulating electrode of 400μm wire with a stimulus generator [28]. The threshold charge of rabbit's RGC is about 3 times larger and TCME is about 135 times larger than this work. Zrenner used 4 x 4 50μm side square microelectrode array with a stimulus generator to deliver power to the intraocular chip and use photodiode array to receive data [19]. The threshold charge for patients to recognize letters is about 10n-27nC and TCME is 25-67.5$\mu C \cdot \mu m^2$, which is respectively over 3.5 times and 1.5 times larger than this work. Among the 4 studies, only this work used solar

cells as the power delivery system rather than used external power supply through wire connection to reduce heat.

Table VII Comparison of several subretinal studies with this work

	F. Gekeler and A. Stett, 2004 [27]	**R. Jensen and J. Rizzo, 2007 [28]**	**Zrenner et al., 2009 [19]**	**This work**
Subject	Rabbit	Rabbit	Human	Rabbit
Stimulus delivery system	Stimulus generator	Stimulus generator	Stimulus generator	Solar cells
Device	Au with Pt MEA (4 x 2)	Pt wire	TiN MEA (4 x 4)	Si chip with SCA (4 x 4) and Al ME
Electrode size	100μm side	400μm diameter	50μm side	75μm side
Phase	Biphasic	Biphasic	Biphasic	Monophasic
Pulse duration (mS)	0.5	1	0.5-6	10
Method	Extracellular recording	Extracellular recording	Perception	Extracellular recording
Threshold current or voltage	0.94V	17μA	1-2.5V	0.28μA
Threshold charge (nC)	5	17	10-27	2.8
TCME ($\mu C \cdot \mu m^2$)	50	2136	25-67.5	15.8

CHAPTER 4 Four-Block Divisional Power-Supply Stimulation Chip

4.1 Chip Structure

According to the refractory period of retina cells, the retinal stimulation chip needs not to stimulate the retina cells continuously but can stimulate discretely with specific frequency, say, 60Hz. By applying the technique of divisional power supply architecture, output current and the power we saved could be proportional to the divided block numbers. More pixels in a retina chip mean higher resolution but result in a larger area. According to the report of the artificial retina prostheses, [24] we chose 4 x 4 pixel resolution in this work. In a conventional 16-pixel SCA design, as depicted in Fig. 4.1(a), if each pixel of the array requires 1-unit solar cells, then 16 units are required totally. This is not only taking a large area but also not power efficient. If we divide the pixel array into 4 blocks as shown in Fig. 4.1(b), and 4 blocks can be activated in turn with 4 control signals. Then each block can be supplied with 4-unit solar cells. In the same way, if we divide the array into 8 blocks in Fig. 4.1(c) with 8 control signals; then each block can be supplied with 8-unit solar cells. Therefore, if we divide the array into more blocks and supplied with the same power, then the structure is more power efficient than conventional SCA design. Even though wasted power in refractory period can be saved by adding to another blocks for more effective stimulation, power control unit (PCU) also requires power. Therefore, in this work, we only separated the pixels into 4 blocks and each block contains four pixels.

The discrete stimulus can not cause any misinterpret in the retina. Time interval between two activations of the same block should be less than 16ms and larger than 0ms, that is, overlapping situation is not permitted between each control signals. Therefore, four nonoverlapping and on different phases power control signals should be made to activate four blocks of pixel array in turn. The whole architecture of the chip is shown in Fig. 4.2. The block diagram of PCU is marked in the upper box of Fig. 4.2. Whole PCU is only power supplied by on-chip solar cells. Three main components are in the unit, a pulse generator, three frequency dividers, and two combinational logic circuits. A pulse generator can produce main clock signal to the PCU, and frequency

dividers can produce signals that have lower frequency than clock signal. Two-level combinational logic circuits can make sure the output signals would not overlap with each other. The schematic of the pulse generator is shown in Fig. 4.3. With 13-stage ring oscillator, pulse generator can generate the reference clock. This structure is similar to the one proposed in [29]. Solar cells are the only voltage supply of the clock generator. At the beginning, all MOSFETs are off. As light irradiates Dx1 faster than Dx2-Dx13, anode of the Dx1 rises to HV first and thus triggers M2; the photocurrent of Dx2 becomes the drain current of M2 and the anode of Dx2 falls to LV. LV of Dx2 could not turn on M3 and the anode of Dx3 becomes HV. In the same way, Dx13 rises to HV and feedbacks to M1. The state of M1 changes from LV to HV and the whole circuit thus becomes a clock generator. In order to generate different phase signals, a low power consumption D flip-flop frequency divider shown in Fig. 4.4(a) was chosen. Two frequency dividers are required to generate the inputs of the first-level combinational logic circuits, because the clock signal from the pulse generator is not in a square waveform. A clear square waveform with relatively short rise time and fall time is required for the combinational logic circuit. Therefore, we use two frequency dividers to provide two square waveforms with half and quarter frequency of the clock. We chose the conventional static cross-coupled NAND gate structure to implement the D flip-flop of the frequency divider as shown in Fig. 4.4(b). The operating frequency of the frequency divider is about 0.1kHz to 10kHz. This frequency range is much lower than the radio-frequency application. Therefore, the modern dynamic D flip-flop design is not suitable for this work because of the probability of charge leakage problem. The static design can not only operate in low voltage supply but have lower power consumption. The circuit schematics of the INV gate and the AND gate are shown in Fig. 4.5. AND gate is composed of a NAND gate and an INV gate. Figure 4.6(a) shows the combinational logic circuit 1, two AND gates and four INV gates are used to synthesize two nonoverlapping control signals. Finally four nonoverlapping control signals are synthesized by third-level frequency divider and two asynchronous control signals in Fig. 4.6(b), four AND gates and one INV gate are used in the combinational logic circuit 2. The voltage level of the control signals is only about 0.5V. Tapered buffer as shown in Fig. 4.7 is used for measuring usage. The sizes of the MOSFETs in each block are depicted in Table VIII.

In the design of the conventional SCA, whole chip mainly contains solar cells only. Total power generated by the solar cells is in proportion to the area of solar cells. However, some layout area of the four-block divisional power-supply stimulating chip is occupied by the PCU. Therefore, the power generated by the solar cells in this work

is smaller than conventional SCA for same area. But the power saved by divisional power supply system is much higher than the power generated by the solar cell within the area of PCU. Thereby this structure is still a power efficient one. Table IX shows the specification of the four-block divisional power-supply (FBDP) stimulation chip. Clock frequency is bonded by 8 times of stimulation frequency and the operating frequency of D flip-flop. Power dissipation is limited by the maximum power consumption of a load that would probably damage the retina [30]. Simulation photocurrent of each 5μm x 5μm photo-sensing region solar cell is set as 1nA under 3.60mW/cm^2 light intensity from the measurement result of [25].

The logic gates mentioned above are powered by on-chip solar cells, and each gate requires certain number of solar cells as the power supply. However, the quantity is hard to predict precisely, from [25], at least six solar cells are required in average. Within the limited area, solar cell numbers for the power supply of PCU are designed to 1066. The PCU generates four nonoverlapping phase signals to activate the four blocks in the 16-pixel array in turn as shown in lower box of Fig. 4.2. The pixel circuitry is shown in Fig. 4.8. Each pixel is composed of a PMOS current mirror, photodiodes and a NMOS switch. Whenever the current path is cut off by the switch of MN0, the photocurrent could not be amplified as the output current. As control signal from PCU is at high level, MN0 is turned on; as gate voltage is lower than threshold voltage, M0 is cut off. When one block is activated, four pixels in this block receive the power from the parallel solar cells of all the blocks while the pixels in the other blocks consume almost no power because their photocurrent paths are cut off. The amplified current will be sent out for stimulating the retina tissue via the in-pixel electrode if the block is activated.

In the prototypical design of the pixel circuit, there is only one photo-sensing diode [16]. To acquire a large output current, we connected the photodiode with one stage current mirror. However, with one photodiode current mirror should afford more than 1000 times amplification ratio to generate 1μA current, but the ratio would result in the serious mismatch problem. Therefore, the quantity of the photodiodes is chosen to be 6 to keep the amplification ratio of current mirror to be 190; this ratio was calculated and simulated the best one. There are 5003 solar cells connected in parallel as the on-chip solar cell power supply. Therefore, the quantity of solar cells for each pixel is 312 in average. Whenever one of the block is activated, 312 by 4 solar cells can ensure the photocurrent induced be amplified 190 times although there will be quiescent current in the photodiodes under the light illumination.

In the testing stage, to acquire the waveform and magnitude of the output current,

two methods were used. Firstly, one pixel of each block is connected to current to voltage output convertor as shown in Fig. 4.9. The gain of the OP is very high (>97dB), so output current approximately equals to output voltage of OP dividing R_{OUT} (100kΩ). Secondly, the other pixel of each block is connected to output electrode. If each electrode connects to a resistive load, then we can probe the drop voltage of the load to obtain equivalent output current.

The stimulating frequency is varying with the light strength of illumination, because oscillating frequency of the clock generator is controlled by the photocurrent. Clock frequency uncertainty from light intensity results in unpredictable solar power. Howerver, we can solve this problem by wearing a goggle to provide solar cells with high light intensity.

Table VIII Sizes of the MOSFETs of each circuit

<table>
<tr><th colspan="2">Clock generator</th><th colspan="2">D flip-flop and Combinational logic</th><th colspan="2">Pixel array</th><th colspan="2">Buffer</th></tr>
<tr><td>M1 to M13</td><td>N: 100μm /1μm</td><td>INV</td><td>N:10μm /5μm P:10μm /5μm</td><td>MN0</td><td>N:1μm /1.5μm</td><td>INV1</td><td>P:0.5μm /9μm N:1.8μm /0.6μm</td></tr>
<tr><td rowspan="3" colspan="2"></td><td>NAND</td><td>N:10μm /5μm P:10μm /5μm</td><td>MP1</td><td>P:1μm /1.5μm</td><td>INV2</td><td>P:15μm /9μm N:15μm /9μm</td></tr>
<tr><td rowspan="2" colspan="2"></td><td>MP2</td><td>P: 190μm /1.5μm</td><td>INV3</td><td>P:15μm /9μm N:15μm /9μm M=2</td></tr>
<tr><td colspan="2"></td><td>INV4</td><td>P:15μm /9μm N:15μm /9μm M=5</td></tr>
</table>

Table IX Specification of the FBDP stimulation chip

SPECIFICATION	
Technology	Tsmc 0.18μm 1P6M N-Well CMOS
Power supply	No external power supply
Pixel number	4 x 4 cells
Pixel size	10μm x 10μm - 350μm x 350μm
Stimulating electrode size	10μm x 10μm - 80μm x 80μm
Chip dimension	<1500μm x 1500μm
Output stimulating current	>1μA
Clock Frequency	0.48kHz - 10kHz
Stimulation Frequency	60Hz - 1.25kHz
Power Dissipation	<20mW

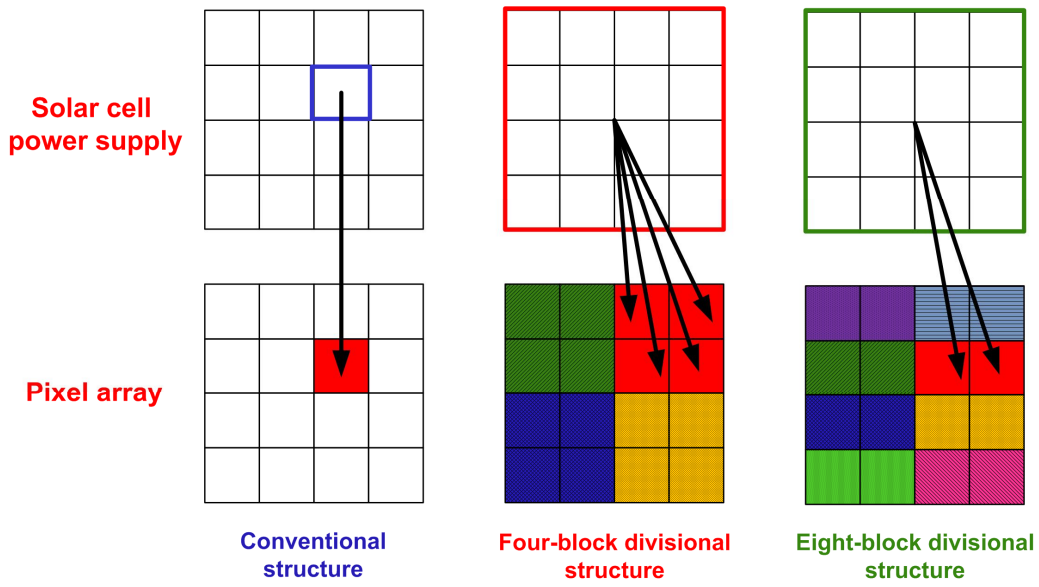

Figure 4.1 Schematic of 16-pixel (a) conventional SCA, (b) four-block divisional SCA and (c) eight-block divisional SCA.

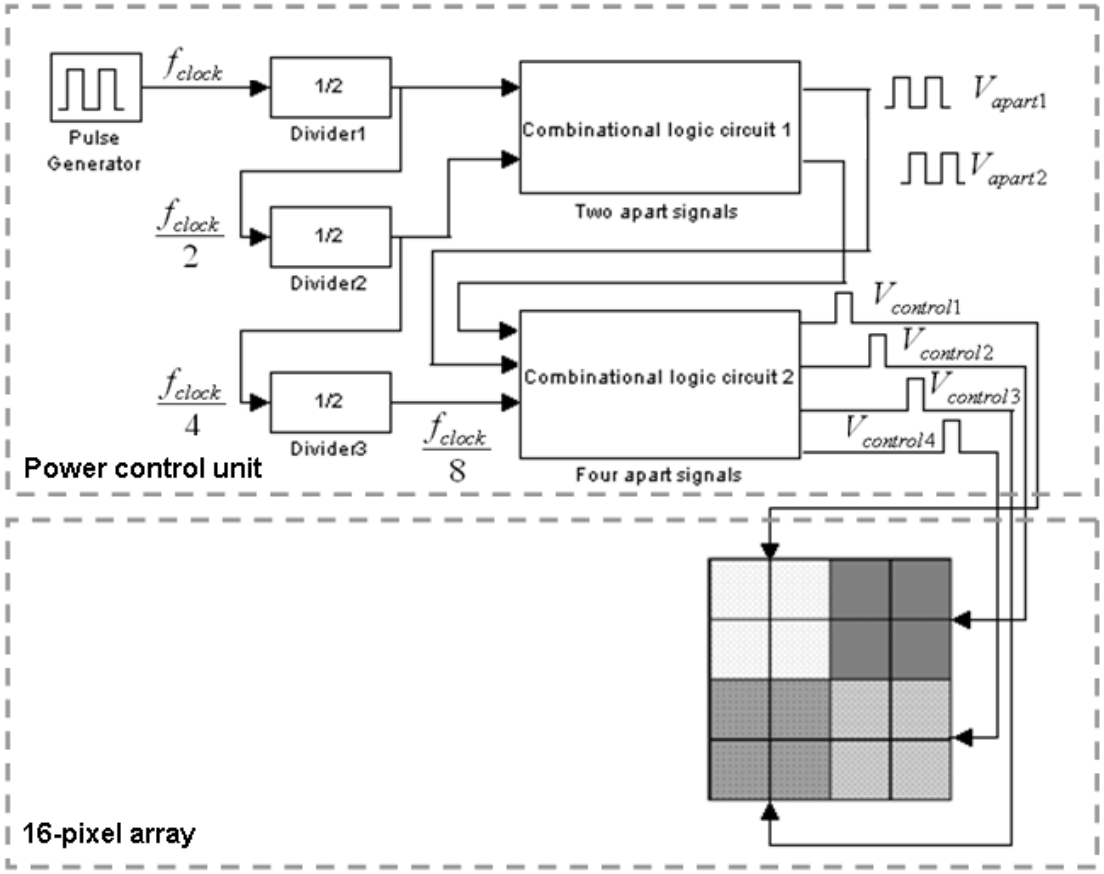

Figure 4.2 Block diagram of the FBDP stimulation chip. Upper block: power control unit (PCU); lower block: 16-pixel array.

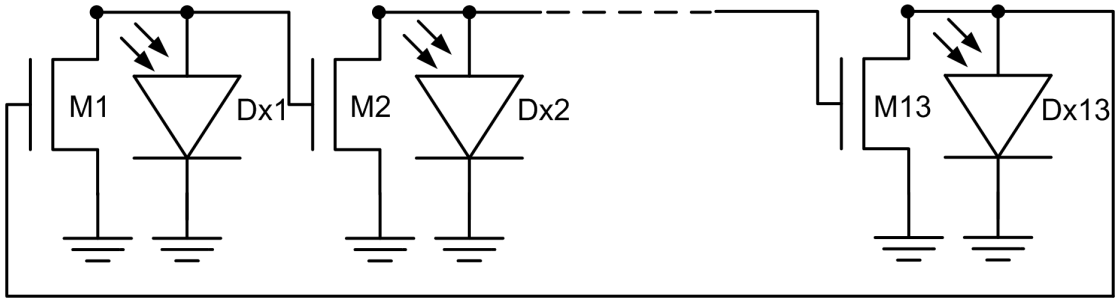

Figure 4.3 Schematic of the pulse generator.

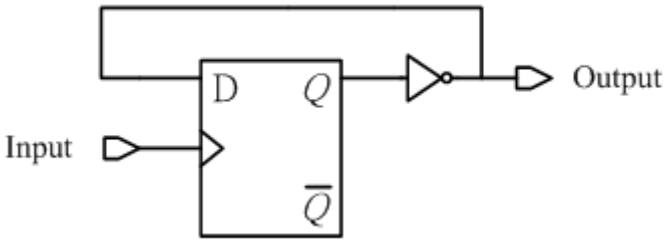

(a)

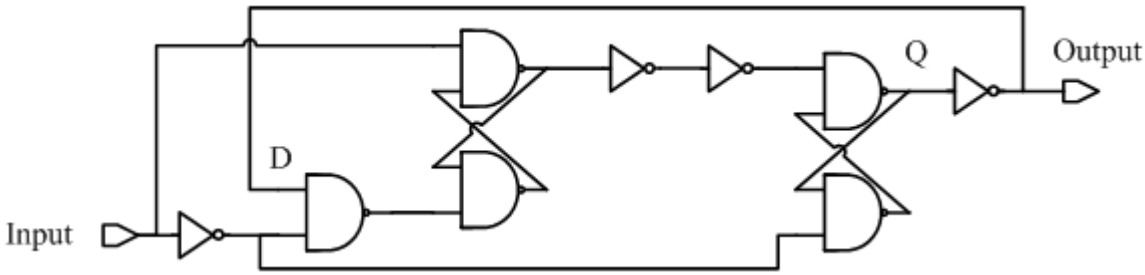

(b)

Figure 4.4 (a) Block dagram and (b) schematic of the frequency divider.

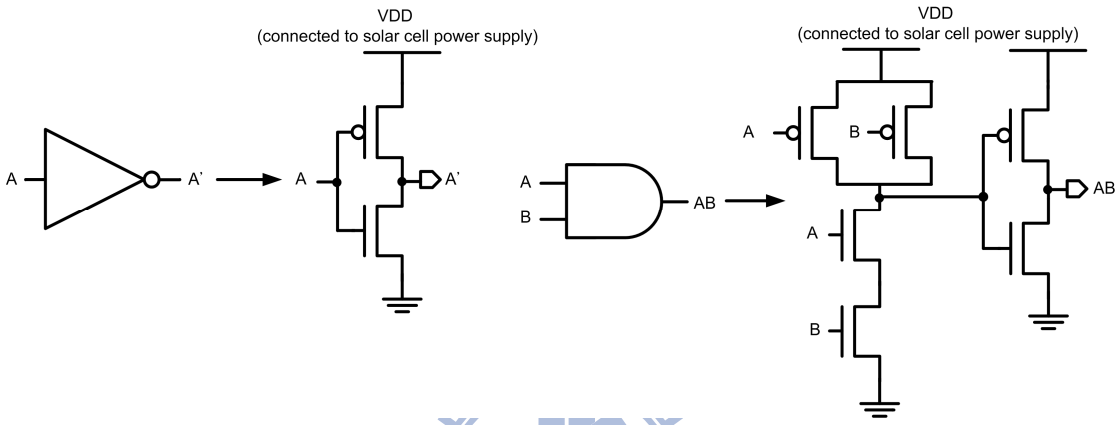

Figure 4.5 Schematic of the NAND gates and INV gates.

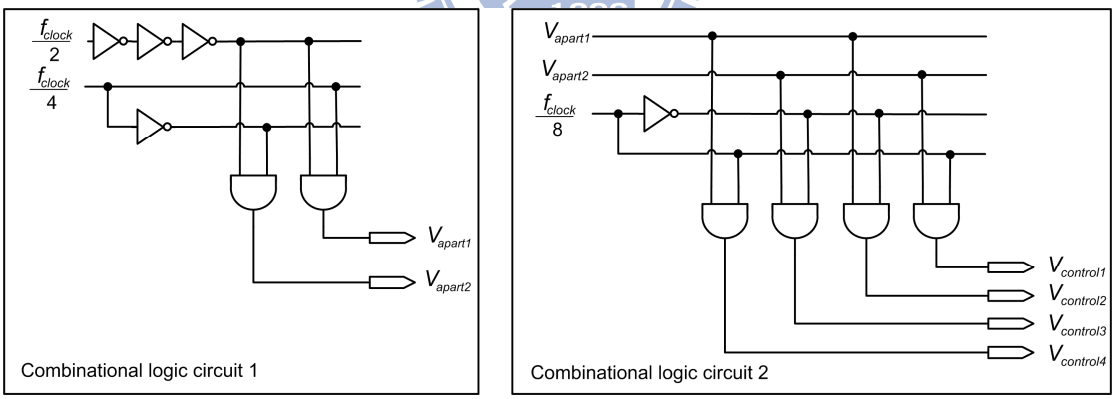

(a) (b)

Figure 4.6 Schematics of (a) combinational logic circuit 1 and (b) combinational logic circuit 2.

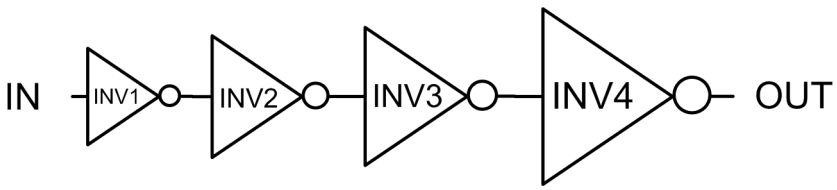

Figure 4.7 Schematic of the tapered buffer.

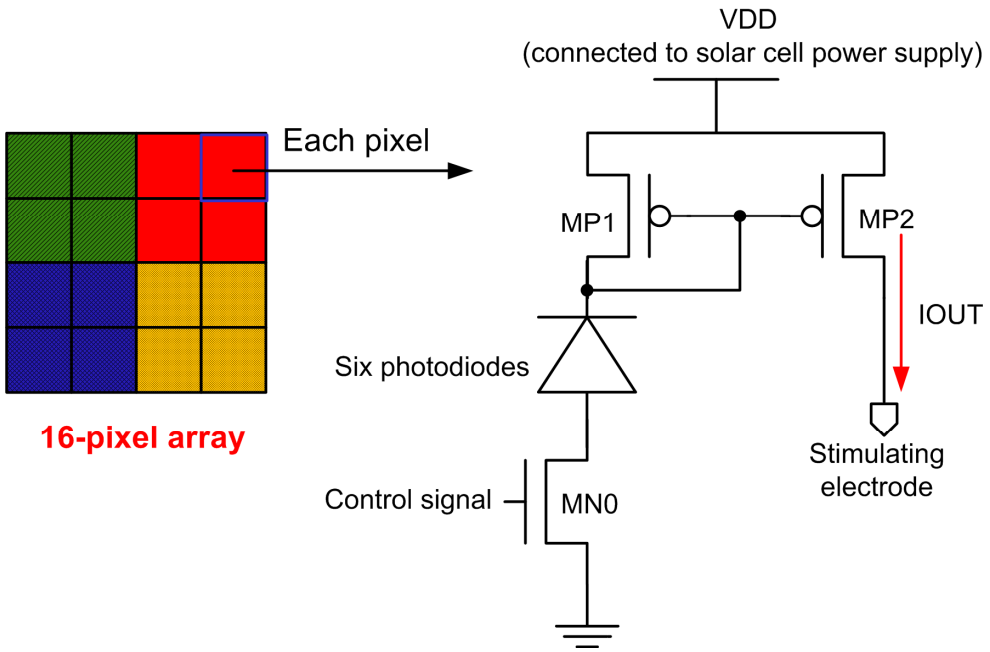

Figure 4.8 Schematic of one pixel circuit. Output current (IOUT) is controlled by the NMOS switch with the control signal from PCU.

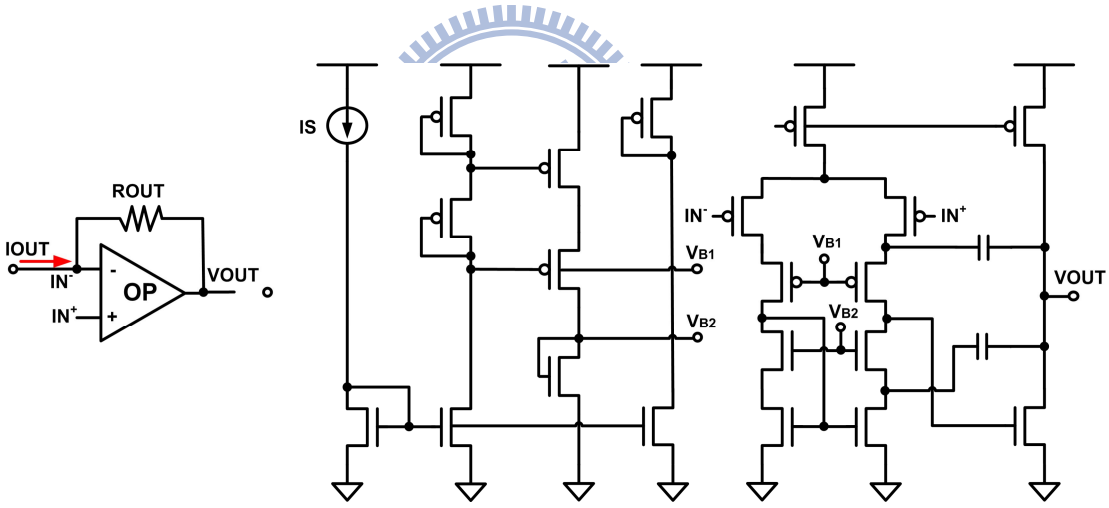

(a) (b)

Figure 4.9 Schematic of (a) current to voltage output convertor and (b) two stage amplifier.

4.2 Simulation Results and Layout Description

4.2.1 *Simulation Results*

The simulation model of each solar cell in the circuit is established based on the photocurrent generated by each solar cell is 1nA for light intensity of 3.60mW/cm^2.

The transient post-simulation results of the orignal clock signal is shown in Fig. 4.10(a), and the buffered signals of clock generator, and three frequency dividers are shown in Fig. 4.10(b). Clock frequency is 2.32kHz. Figure 4.11 shows the buffered four nonoverlapping control signals. The voltage supply of the PCU from the solar power is 0.478V. Signals become 1V after buffering with an external 1.5V power supply for the taperd buffer. Post-simulation results of the output stimulation current of each block are shown in Fig. 4.12. The time interval between neighboring activation is less than 3ms and output stimulating current is 1.01μA per pixel. The monte-carol simulation results with 5% variation of the output current are shown in Fig. 4.13. The results show that no overlapping situation is encountered from one parameter to another. With 5% variation of width, length and threshold voltage, the output is from 0.818μA to 1.22μA per pixel. Figure 4.14 is the post-simulation results of the current to voltage convertors. The differential value is 0.099 V and R_{OUT} is 100kΩ. Calculated output current is 0.99μA, only 0.02μA difference between actual and calculated output current. Figure 4.15 shows the post-simulation results of the voltage drop of 50kΩ resistances of the output electrodes. The voltage drop is 50mV and the calculated output current is 1.01μA.

Power consumption of the whole chip, which was calculated by solar cell power supply, is 2.92μW including 0.53μW from the control unit under 3.60mW/cm^2 illumination light intensity. Since PCU takes some portion of chip area and thus consumes some photo-sensing region of pixel array. But overall current efficiency of this structure would be higher than conventional SCA.

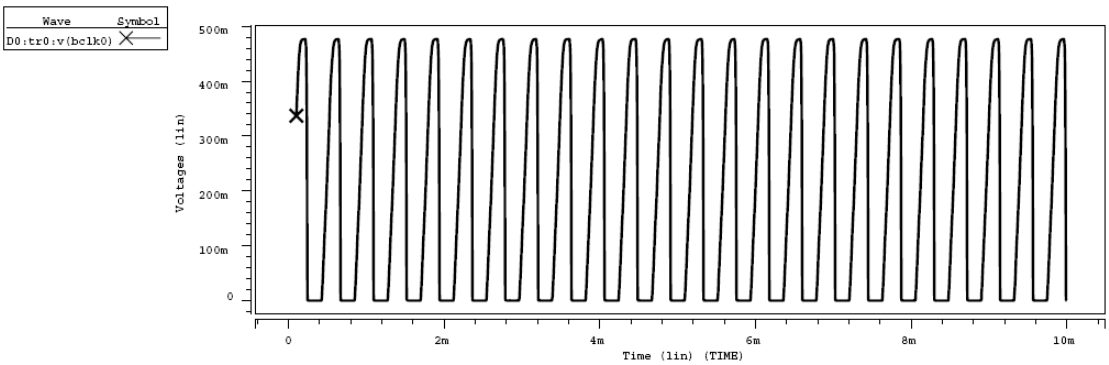

(a)

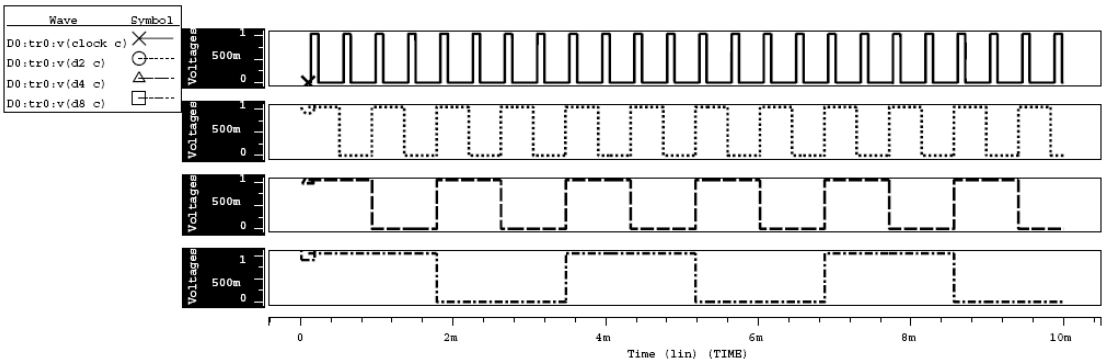

(b)

Figure 4.10 Post-simulation results of (a) the clock generator and (b) buffered signals of the clock generator and frequency dividers under 3.60mW/cm^2 light intensity.

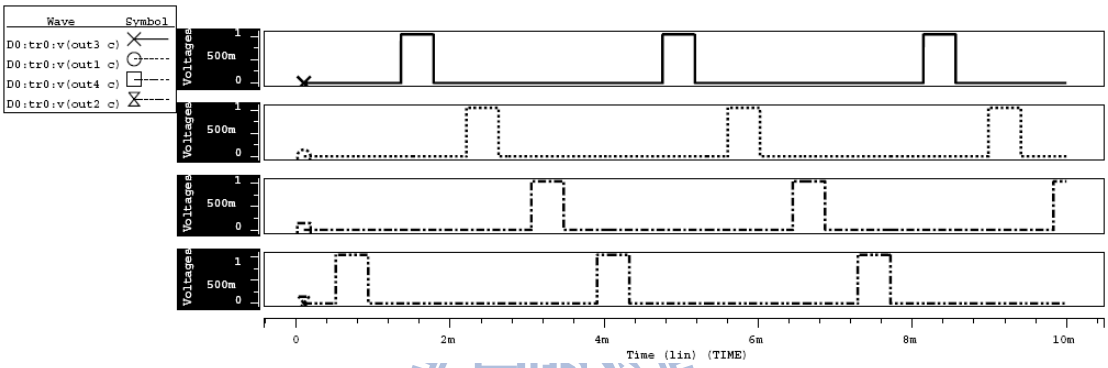

Figure 4.11 Post-simulation results of the four buffered control signals under 3.60mW/cm^2 light intensity.

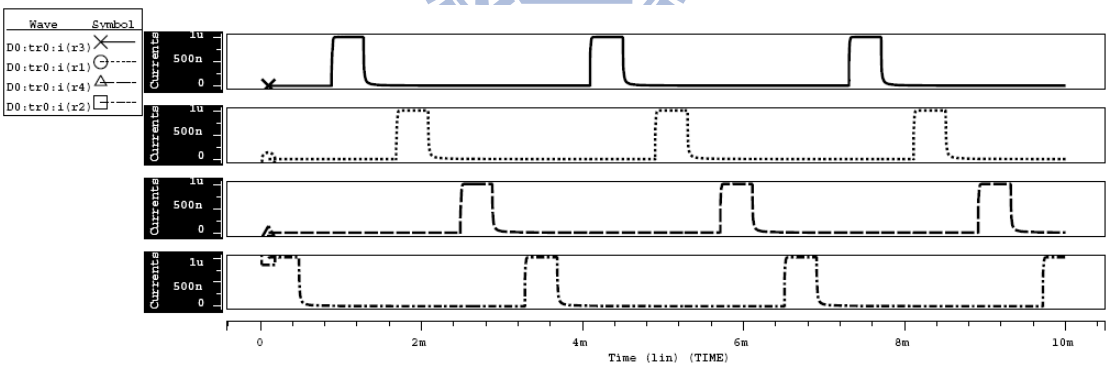

Figure 4.12 Post-simulation results of the output stimulation current of each block under 3.60mW/cm^2 light intensity.

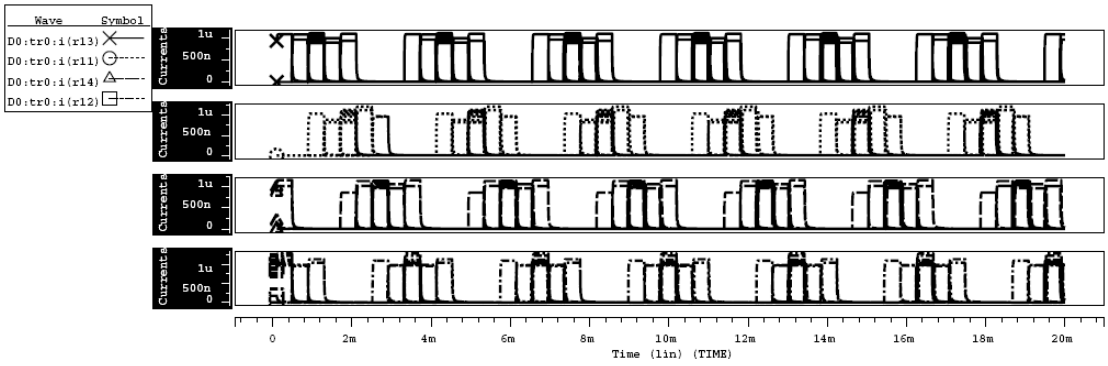

Figure 4.13 Monte-carol simulation results with 5% variation of the output stimulation current of each block under 3.60mW/cm^2 light intensity.

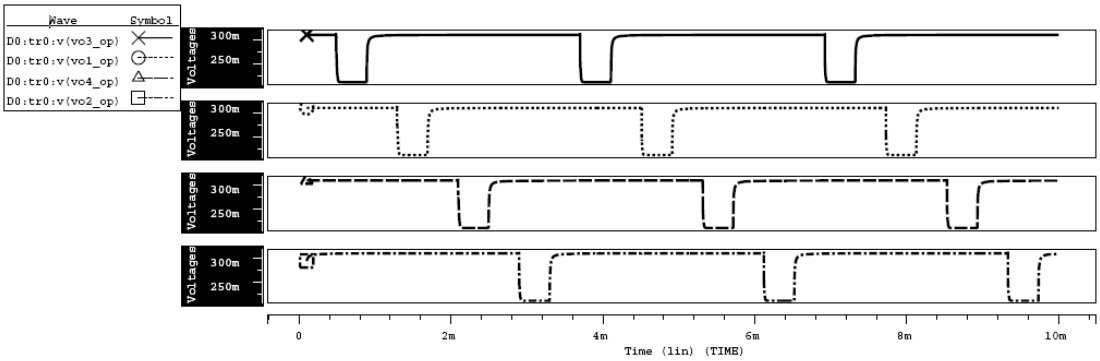

Figure 4.14 Post-simulation results of the output voltage of current to voltage convertors under 3.60mW/cm^2 light intensity.

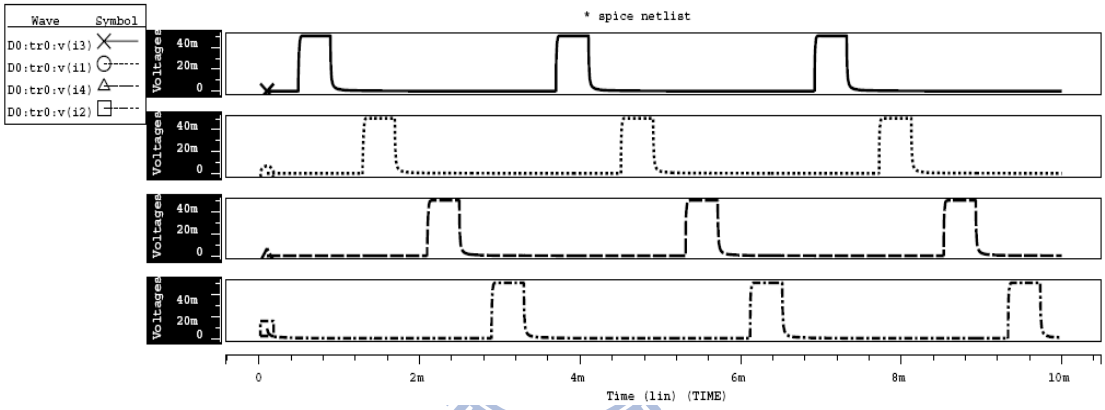

Figure 4.15 Post-simulation results of the voltage drop of 50kΩ resistances of the output electrodes under 3.60mW/cm^2 light intensity.

4.2.2 Layout description

The layout methodology of the solar cell is a key issue of this retinal stimulation chip design. In order to keep the p-substrate floating, all the NMOS in this FBDP stimulation chip is located in the DNW as shown in Fig. 4.16(a). With the twin-well technology, the P-Pick up (body) of the NMOS can connect to the P-Well within the DNW. The floating p-substrate can ensure the performance of the solar cell and prevent the leakage current by the parasitic lateral BJT. There is no leakage path between PMOS and solar cell connection, so PMOS needs not to locate in the DNW. In addition to the leakage problem, a silicide layer procedure may contribute to serious photoelectric effect in the tsmc CMOS 0.18μm technology. A silicide is a compound of silicon and electropositive elements, such as titanium silicide ($TiSi_2$). The problem

is that the light penetrability of the silicide is very low. Therefore, the incident light of both the solar cells and photodiodes is insufficient to provide the power supply and photocurrent. The silicide blocking procedure is required to prevent the light penetrability problem in this retinal stimulation chip. Therefore, the layout of individual solar cell and photodiode is alone with the RPO layer (SAB layer in umc technology) to block the silicide on the diffusion region and avoid the efficiency loss in the photoelectric effect.

Four main parts are proposed in the FBDP stimulation chip as shown in Fig. 4.17. Firstly, the PCU, producing nonoverlapping and different phase control signals for the retinal stimulation part, is shown in Fig. 4.18. Each stage of ring oscillator is composed of a NMOS and 4 solar cells (with 1μm space between each other). There are 44 transmission gates in the PCU. The 1066 solar cell power supply of the PCU is connected together and here shows partial of the solar cells only. The space between each solar cell is 8μm. Secondly, the pixel array with 4 by 4 resolutions, mimicking the photoreceptor cells of the retina, can generate the stimulus for retina according to the incident light strength. In each pixel as shown in Fig. 4.19, there are 6 photodiodes with 6μm space between each other to generate photocurrent, a NMOS switch and a PMOS current mirror. The 5003 solar cell power supply (with 2.5μm space between each other) of the pixel array is located in the middle apart of the FBPD stimulation chip. The current monitor amplifier and R_{OUT} for measuring current is shown in Fig. 4.20. The main circuit includes a PCU and a 16-pixel array. Thirdly, the test-key of PCU is shown in the left block of Fig. 4.17. For the measurement usage, we can obtain detail information of the PCU from the test-key. Tapered buffers were located between the PCU and output pads. Lastly, containing 102 solar cells with 8μm space between each other, a solar cell test-key was added to measure the functionality of solar cells in the lower-right corner of Fig. 4.17. The fact that solar cells with farer space between each other was verified in previous experiment [25] that generated photocurrent is larger than closer space.

The layout dimension of the whole chip is 1.350mm x 1.315mm and the area of the solar cells is about 0.76mm^2, almost half area of the whole chip. The larger number of solar cells can better ensure the function of the PCU and the current mirror of the pixel array.

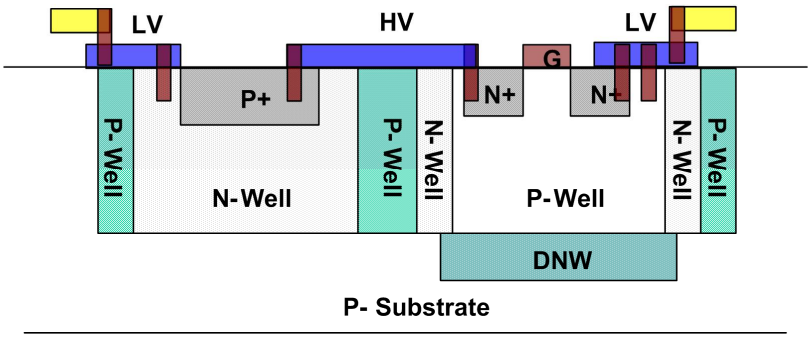

(a)

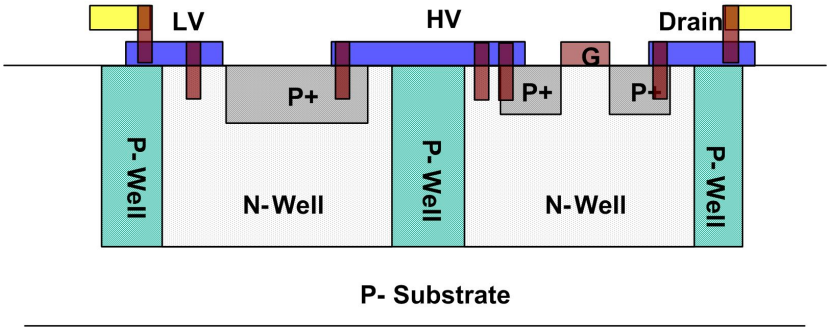

(b)

Figure 4.16 Cross-sections of a solar cell and (a) a NMOS and (b) a PMOS in parallel connection.

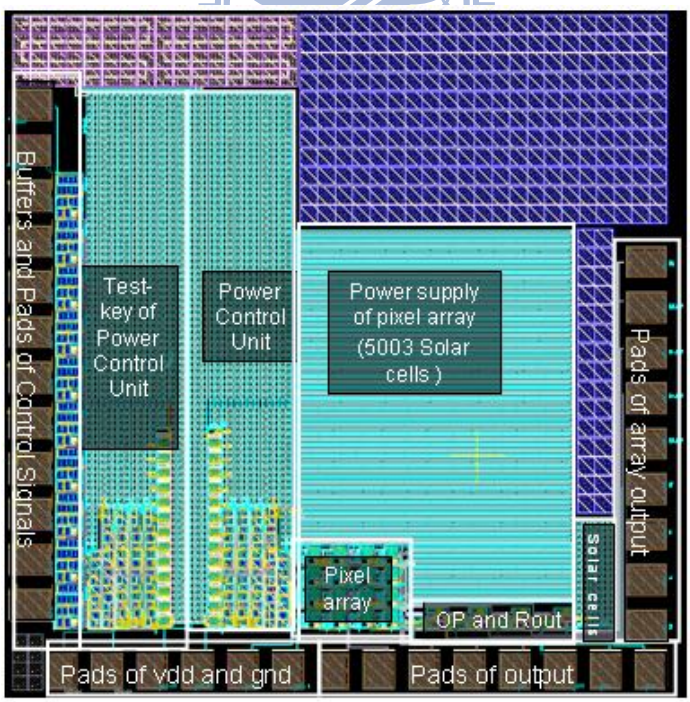

Figure 4.17 Layout of the FBDP stimulation chip with control circuit and other test-key. The layout dimension is 1.350mm x 1.315mm.

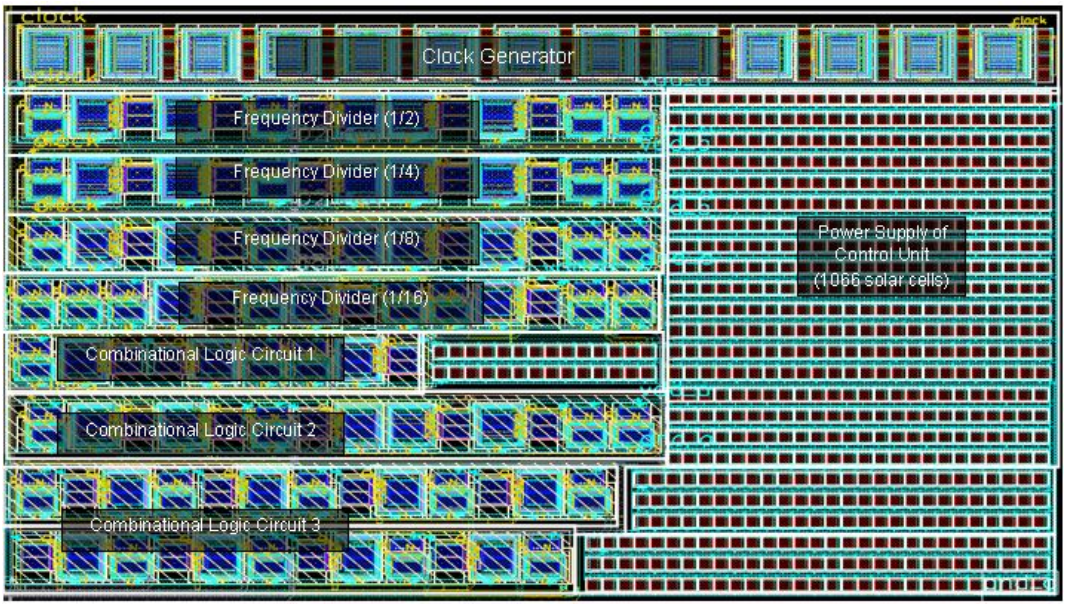

Figure 4.18 Layout of the PCU.

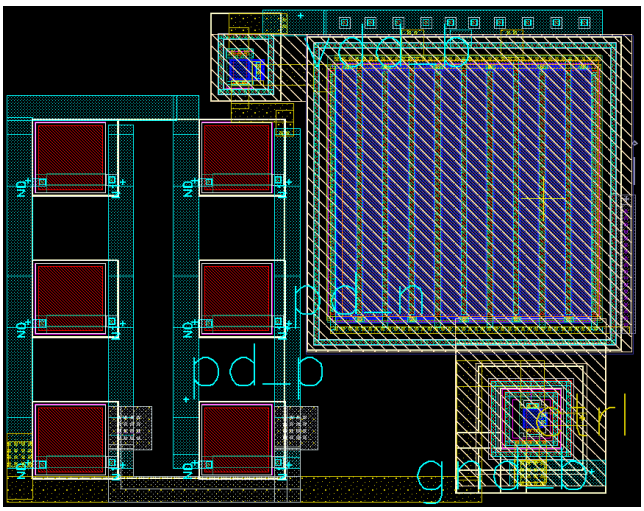

Figure 4.19 Layout of a single pixel in the 16-pixel array.

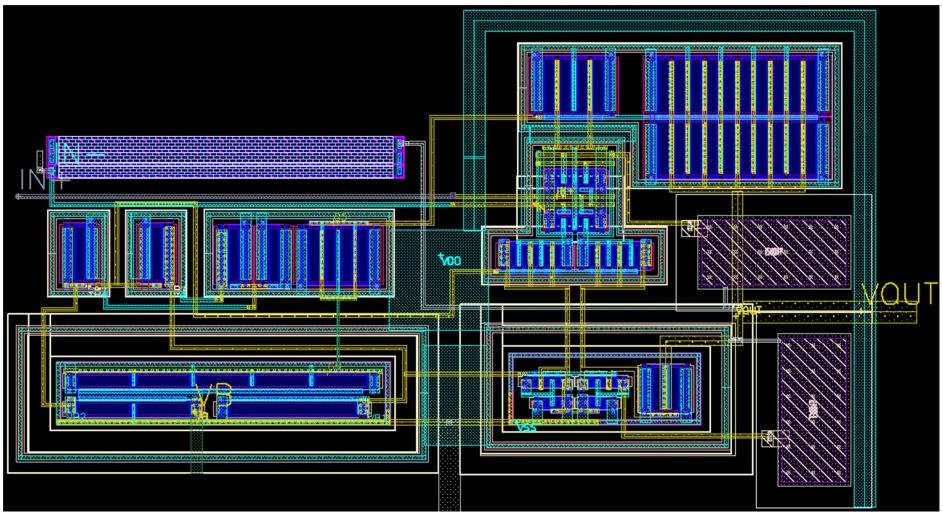

Figure 4.20 Layout of the current to volatge convertor and R_{OUT}.

4.3 Measurement Results

Chip micrograph of the FBDP stimulation chip is shown in Figure 4.21. Whole chip size is 1.350mm x 1.315mm. To measure the output waveforms of PCU test-key, the measurement environment is shown in Fig. 4.22. The light source we used here is a LED flashlight (Ultrafire WF501B). The flashlight can be tuned to three different kinds of brightness (high, middle and low). A convex lens was used to converge the diverged light, so as to illuminate whole chip with high light intensity. To observe the output waveform of each signal, 4-channel oscilloscope (Lecroy wavesurfer 104MXS) was used. The measurement results of the clock generator and frequency dividers are shown in Fig. 4.23. VDD of the tapered buffer is 0.8V here. Even under light intensity of 92.3mW/cm^2, the very high brightness could not afford to perform functional output waveforms except the clock signal. Due to high light intensity, the clock frequency is as fast as 7.5kHz. The abnormal divided frequcy signals resulted in error function of control signals as shown in Fig. 4.24. The measurement result of the voltage supply of PCU is only 0.05V. Therefore, the error signals may come from insufficient power supply of solar cell system or unknown leakage problem. To verify the point of insufficient power supply, we connected the voltage supply of PCU test-ley with external power supply. With 2540 extra solar cells from the solar cell test-keys of other chips (SSCA stimulation chip) as shown in Fig. 4.25, the voltage supply of PCU increased to 0.5V as shown in Fig. 4.26 under 15.8mW/cm^2 light intensity. Furthermore, the function of the clock generator, three frequency dividers and four different phase control signals are all the same as we simulated as shown in Figs. 4.27 and 4.28. The clock frequency drops to 1.5kHz. Low light intensity results in slow clock frequency and lower power comsuption of PCU but also brings about lower power supply of solar cell system. Therefore, total 3606 solar cells are required for the PCU under 15.8mW/cm^2 light intensity.

BJT leakage problem would not occur in different substrates of different chips, whereas the voltage level of floating P-substrate was not defined which may lead to unpredicted leakage problem. To make sure that the right function was not from the elimination of parasitic BJT problem, internal solar cells were added to the power supply PCU. Whenever the control signals of the pixel array are not in function, the MOSFETs of each pixel would be always off. Thereby the solar cell power supply system of the pixel array was not used by the current mirror, thus became a sufficient solar cell power supply for PCU test-key. The measurement results of the clock

generator, three frequency dividers and four different phase control signals with 5003 extra internal solar cells are similar to Fig. 4.27 and Fig. 4.28, only slight difference at clock frequency. As the function of each signal is also correct with internal solar cell supply, no leakage problem shows up in the structure of solar cells accompanying with CMOS. The measurement environment for measuring output stimulation current is shown in Fig. 4.29. Load resistances (R_L) of 50kΩ were placed at four electrodes of pixel array. Figure 4.30 shows the measurement results of four different phase signal of output currents from the voltage drops of R_L. With 2540 extra external solar cells for the PCU, voltage level is 55mV under 15.8mW/cm^2 light intensity. The measured current from the electrode is 1.1μA for each pixel, which is close to the post-simulation result. Comparing with 16-pixel conventional SCA, which can only generate 0.31μA at 15.8mW/cm^2 for total 5003 solar cells, output stimulation current of this structure is 3 times larger. Output waveform of the current to voltage convertor was not able to acquire, because the input of the OP should be higher than 0.6V, which is beyond the operating range of the current mirror. Summary results of the FBDP stimulation chip are shown in Table X. The simulation and measurement results all conform with the specification. Comparing the power dissapation between the simulation and measurement results by setting photocurrent of each solar cell to be 1nA, the measurement results of PCU seemed to require more solar power than simulation. Solar cell model we used might not be very correct.

Table X Comparison between the simulation and measurement results with the specification of the FBDP stimulation chip

	Specification	**Simulation results**	**Measurement results**
Technology	0.18μm 1P6M N-Well CMOS		
Power supply (PCU + Pixel array + Extra solar cells)	No external power supply	Solar power supply (1066+5003+0)	Solar power supply (1066+5003+2540)
Light intensity	None	3.60mW/cm²	15.80mW/cm²
Pixel number	4 x 4	4 x 4	4x 4
Pixel size (μm²)	10 x 10 - 350 x 350	50 x 50	50 x 50
Stimulating electrode size (μm²)	10 x 10 - 80 x 80	20 x 20	20 x 20

Chip dimension (μm²)		<1500 x 1500	1350 x 1315	1350 x 1315
Output stimulation current (μA)		>0.5	1.01	1.10
Clock frequency (kHz)		0.48 - 10	2.32	1.50
Power dissipation	**PCU**	<20mW	0.53μW	1.80μW
	Pixel array		2.39μW	2.50μW

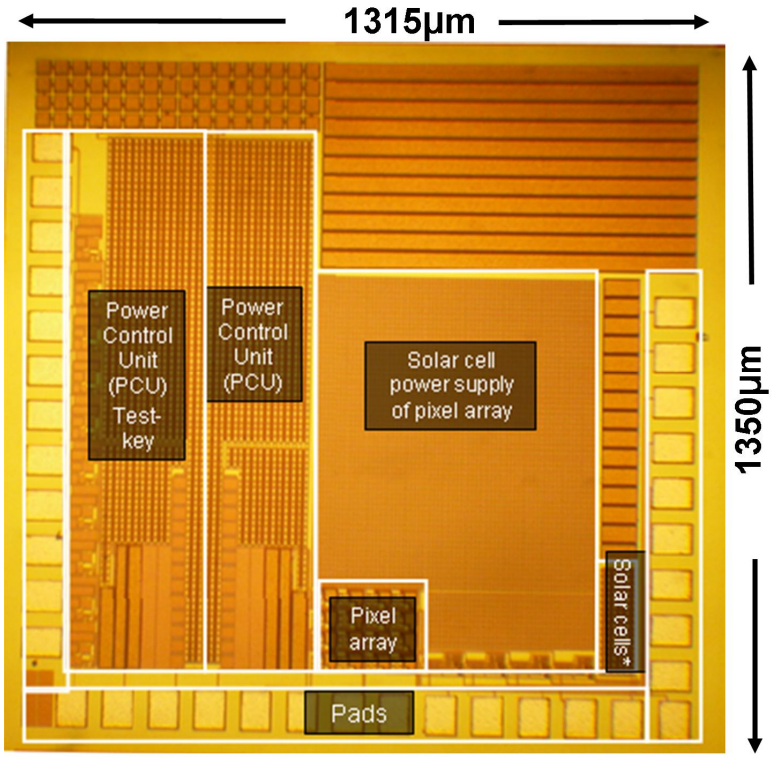

Figure 4.21 Chip micrograph of the FBDP stimulation chip.

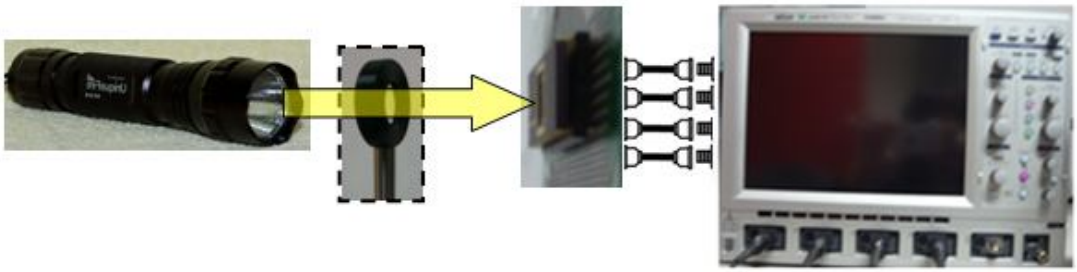

Figure 4.22 Measurement environment of the PCU test-key. Left part: high brightness LED flashlight with a convex lens; middle part: chip setup; right part: 4-recording channel oscilloscope.

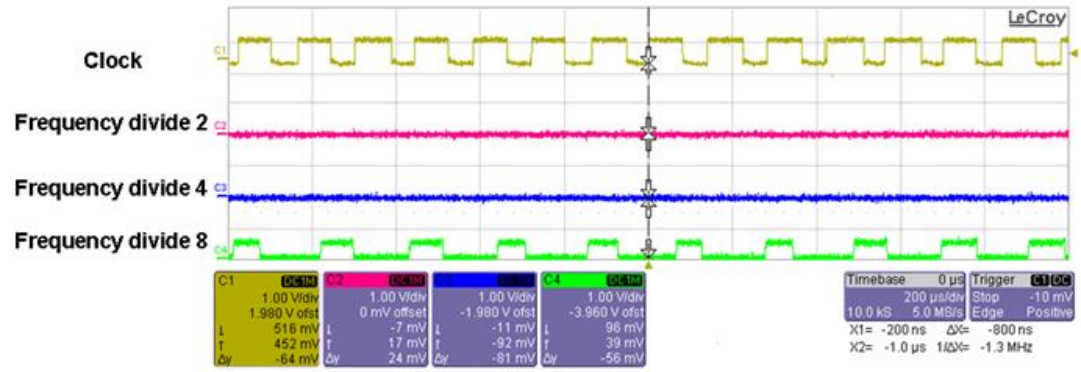

Figure 4.23 Measurement results of the clock generator and frequency dividers under 92.3mW/cm^2 light intensity.

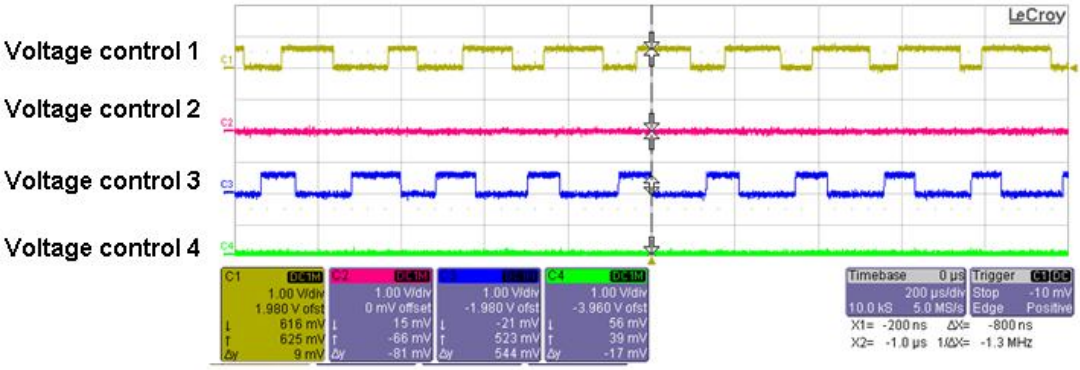

Figure 4.24 Measurement results of the control signals under 92.3mW/cm^2 light intensity.

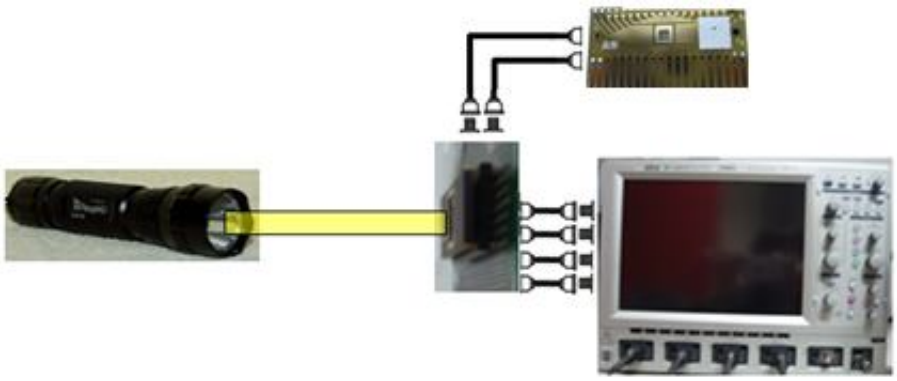

Figure 4.25 Measurement environment of the PCU test-key. Left part: middle brightness LED flashlights; middle part: chip setup wth an external solar cell power supply; right part: 4-recording channel oscilloscope.

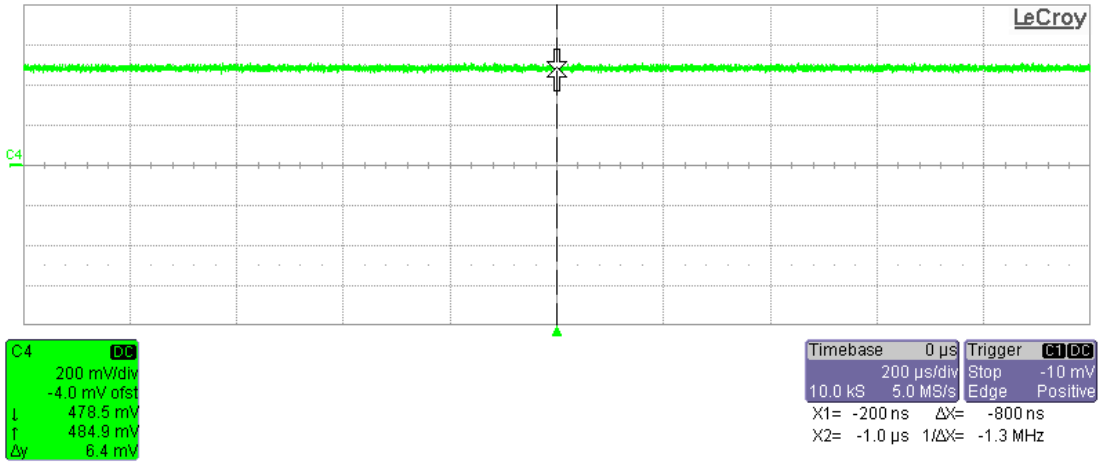

Figure 4.26 Measurement result of the voltage supply of PCU under 15.8mW/cm^2 light intensity with extra 2540 external or 5003 internal solar cells. Voltage level increases to 0.5V.

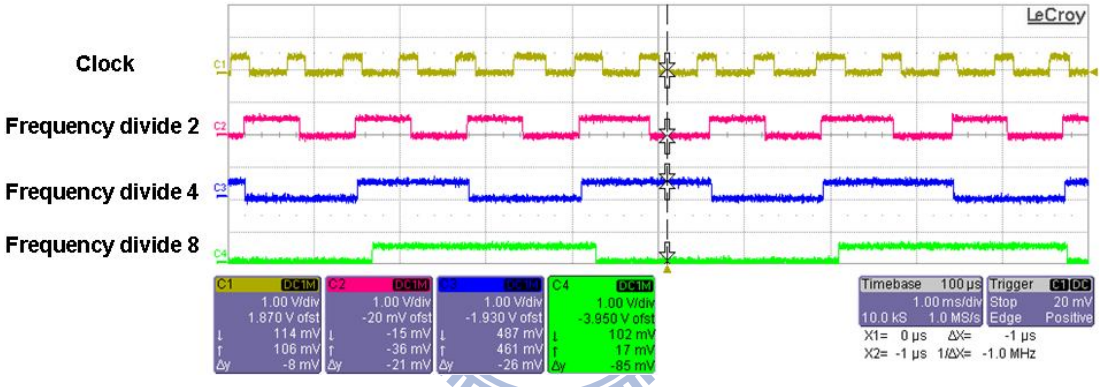

Figure 4.27 Measurement results of the clock generator and frequency dividers under 15.8mW/cm^2 light intensity with extra 2540 external or 5003 internal solar cells. Voltage level is 0.5V as the VDD of tapered buffer.

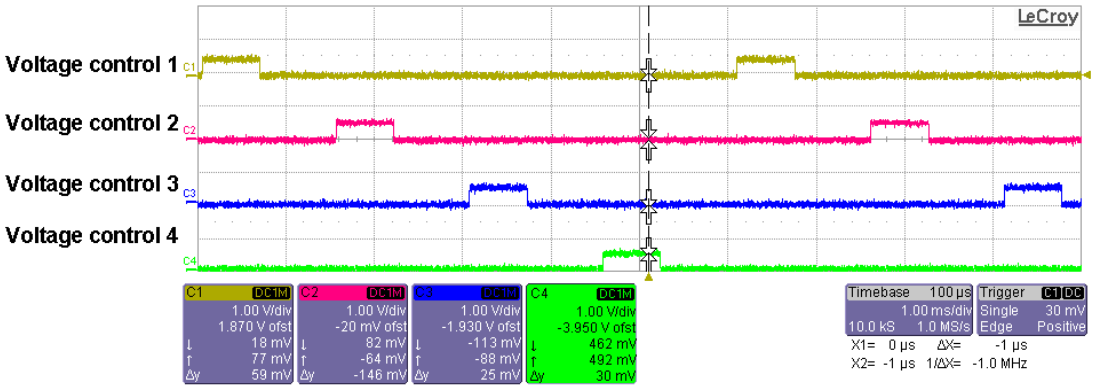

Figure 4.28 Measurement results of four different phase control signals under 15.8mW/cm^2 light intensity with extra 2540 external or 5003 internal solar cells. Voltage level is 0.5V as the VDD of tapered buffer.

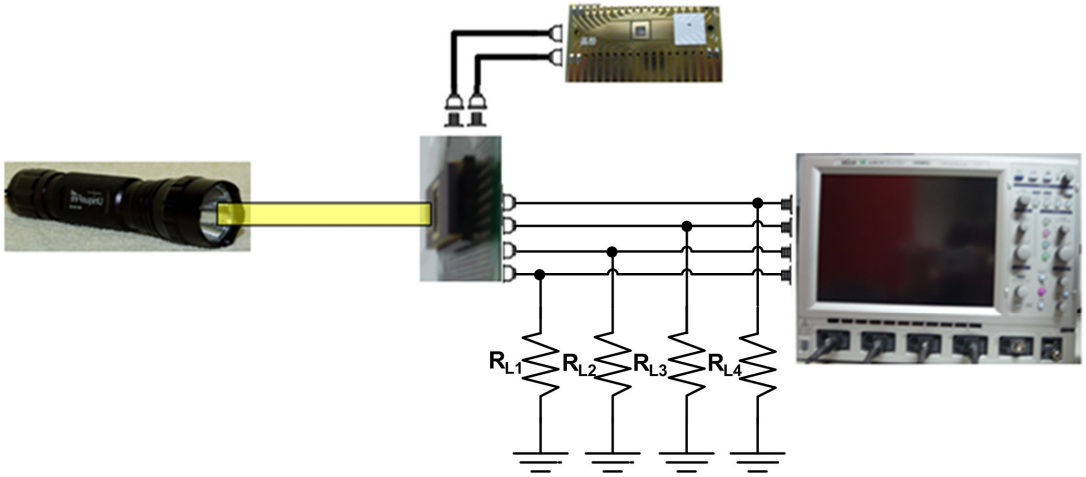

Figure 4.29 Measurement environment of the pixel array. Left part: middle brightness LED flashlights; middle part: chip setup wth an external solar cell power supply; right part: 4-recording channel oscilloscope.

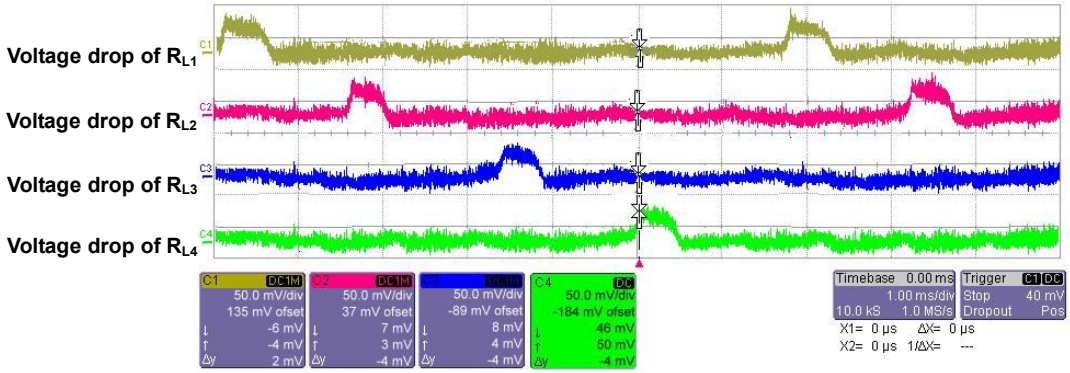

Figure 4.30 Measurement results of four different phase signals of output current from the voltage drop of external 50kΩ resistances. With 2540 extra external solar cells for PCU, voltage level is 55mV under 15.8mW/cm^2 light intensity.

4.4 Discussion

Although the function of PCU and pixel array is designed and verified with only on-chip solar cell supply, from the simulation results, the designed solar cells are sufficient in each segment, but the measurement results do not reveal the same conclusion. One possible reason is that the simulation model of solar cells is not very correct. Comparing the measurement and simulation I-V curves of the solar cell test-key from the measurement environment of Fig. 3.23, the simulation result with the original model varies significantly with the measurement, see Fig. 4.31. To modify the

P+/N-Well diode model, looking into the P-N junction voltage equation of a diode is necessary:

$$V_D = nV_T \ln(\frac{I}{I_s})$$

where n is emission coefficient, V_T is thermal voltage and I_s is saturation current. Changing n from 1.03 to 1.08 makes the original I-V curve shift to the revised simulation curve depicted in Fig. 4.31. However, whole chip simulation with this model is still function well as the quantity of the solar cells remaining the same for 1nA photocurrent of each solar cell. Therefore, the problem may come from the loading effect of the solar cells, because the redistributed current may not afford to supply whole PCU. With various loading connected to the anode of the solar cell test-key, the positive voltage drops according to the drawn current from solar cells. Measurement and simulation loading to positive voltage curves of the solar cell test-key under 73.2mW/cm^2 light intensity of laser are shown in Figure 4.32. Without extra loading paralleled with each solar cell, the positive voltage of original simulation curve is larger than measurement. In order to develop a reliable model of a CMOS integrated chip with solar cells, it is necessary to refer to the measurement R-V curve. Exploiting the result of the characterization, an equivalent circuit of the solar cell can be obtained in Fig. 4.33 [31]. We discovered that each solar cell with 266-MΩ shunt resistance (R_{sh}) and 10-kΩ series resistance (R_{se}) better fit for the measurement curve. As a result, the original R-V curve shifts to the revised simulation curve depicted in Fig. 4.32.

Applying the n factor, R_{sh} and R_{se} to the simulation of the PCU, for 1nA photocurrent of each solar cell, the function of each signal is incorrect except clock. With solar cells 3606 solar cells, the redistributed current is balanced to supply both PCU and solar cells, resulting in a correct function as shown in Fig. 4.34. With the new model, simulated output current for each pixel of the power efficient chip is also similar to measurement result.

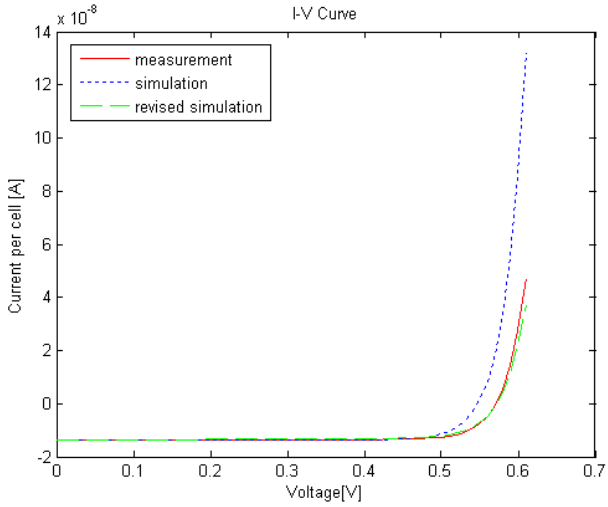

Figure 4.31 Measurement and simulation I-V curves of the solar cell test-key under 73.2mW/cm^2 light intensity of laser.

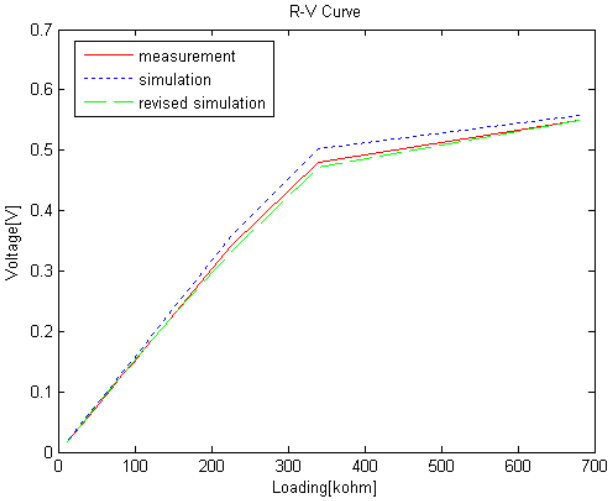

Figure 4.32 Measurement and simulation loading to positive voltage curves of the solar cell test-key under 73.2mW/cm^2 light intensity of laser.

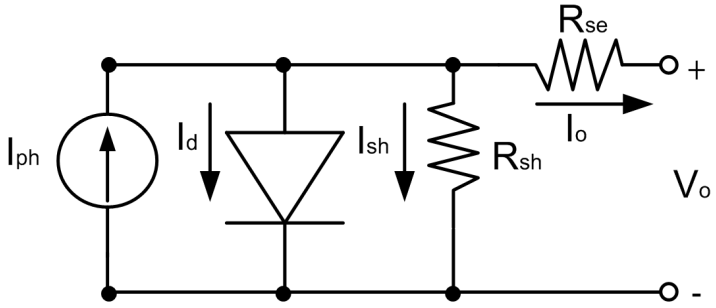

Figure 4.33 Equivalent circuit model of a solar cell. I_{ph} represents the photocurrent, R_{sh} is the shunt impedance and R_{se} is the series impedance. Currents pass through solar cell, R_{sh} and R_{se} are I_d, I_{sh} and I_o, respectively.

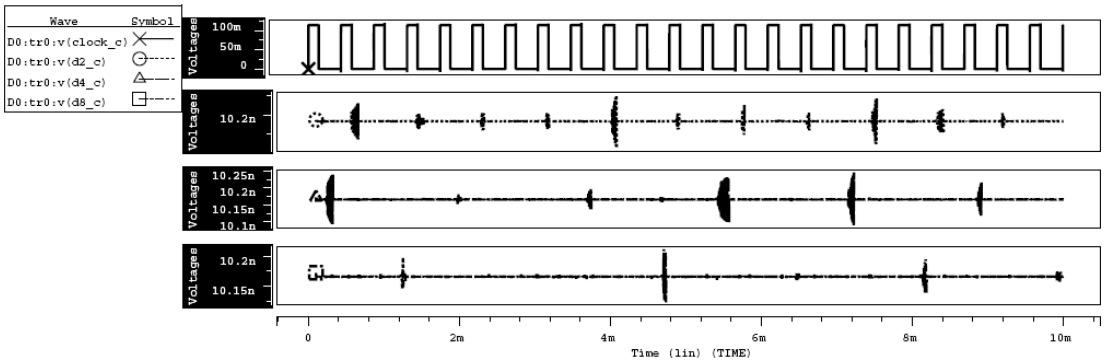

(a)

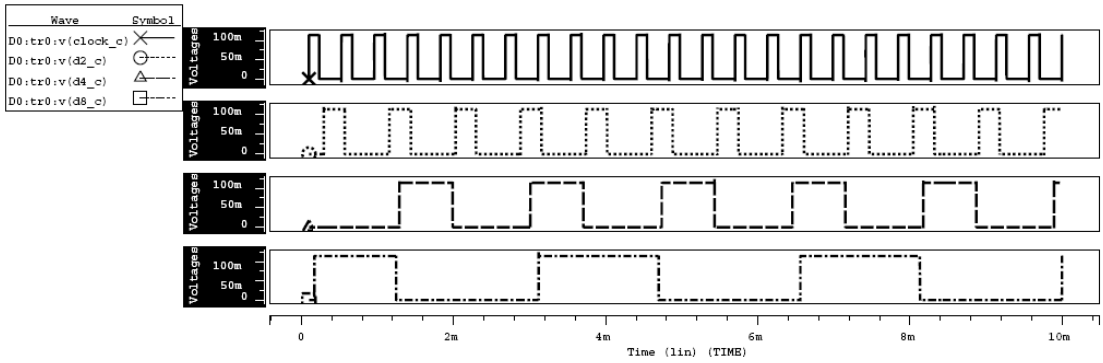

(b)

Figure 4.34 Pre-simulation results of the buffered signals of clock generator and frequency dividers with new solar cell model. Power supplies of the PCU are (a) 1066 solar cells and (b) 3606 solar cells. VDD of the tapered buffer is 0.7V.

CHAPTER 5 Conclusions and Future Work

5.1 Conclusions

In this thesis, efficient current stimulation CMOS chips for subretinal prostheses have been designed, analyzed, and fabricated. On-chip solar cell supply system is integrated with circuit system in CMOS technology. The feasibility of the supply system has been verified in the work. From the multi-size microelectrode chip, we have proved that retina interface impedance increases with a decreasing electrode size and decreases with increasing frequency. At high frequency, retina interface impedance also increases with decreasing center-to-center distance of electrodes. According to the experiment data, we have acquired rough magnitude of interface capacitance (0.01n-1nF), charge transfer resistance (1MΩ-100MΩ) and retina impedance (10kΩ-200kΩ) of 50μm side to 80μm side square retinal electrodes. These impedances are studied as a function of electrode sizes.

The silicon retinal stimulation chip that is composed of 16-pixel SSCA, 75μm x 75μm stimulating electrode and local surrounding return electrode has been designed and verified after the in vitro experiment. The experimental data describes the silicon retina with solar cells can successfully trigger the retina cell by the electrical stimulus. With 1mW (8cd/cm^2) output power of laser, threshold charge of 2.8nC is able to activate ganglion cells of isolated rabbit's retina. This threshold charge is about 3.5 times lower than those reported by Zrenner et al. [19]. The value of threshold charge multiplies electrode size is also low, only 15.8μC • μm^2, which is 1.5 times lower than [19].

With 3D spreading resistive network model, stimulation current of SSCA with local surrounding return electrode is 1.08μA, which is 10 times of remote surrounding return and 3 times of remote single return. Stimulation current of TSCA is 2.09μA, which is 2 times more current efficient than SSCA. With local surrounding return electrode, optimum solar cell numbers of each pixel of SSCA and TSCA stimulation chips are 576 and 192; optimum photo-sensing regions are 14400μm^2 and 19200μm^2. Current stimulation efficiency of TSCA is 1.65 times larger than SSCA with the optimum photo-sensing region.

Taking the advantage of the refractory period of retina cells, about three times output stimulating current is achieved and four times power has saved by the FBDP

stimulation chip in comparison with conventional SCA chip. The time interval between neighboring activation of the same pixel is smaller than the refractory period of the cells thus to provide continuous signals for the brain. No extra pulse generator is required to transmit pulse light source into the eyeball, that is, common light sources with DC power supply are allowable. Nonoverlapping design structure can avoid misinterpret in the retina, because only four pixels of the same block are activated at the same time. The discrete stimulus can stimulate the retina cells with pulses thus to operate at high frequency domain. The solar cell power supply can activate four pixels to four pixels in turn to increase the output stimulating current. The stimulating output current is approximately 1.1μA under the illumination of 15.8mW/cm^2 light intensity. The retinal stimulation chips demonstrate good mimic of electrical behavior of human retina with low-power consumption.

5.2 Future Work

In the future, several things have to be done for the designed chips. To reduce contact resistance with the attachment of retina and microelectrode chip by the weight of cover glass and to find more accurate values of retina impedance by doing more experiments are the first things. Secondly, since the in vitro experiment of SSCA stimulation chip has be done the verified its function, the next stage of this chip is to implement in vivo experiment. The electrode material of aluminum is easy to decay, so plating bio-compatible metal, such as Pt, on Al is need to be done first. Animal experiment of implanting the chip in a rabbit's or a rat's subretina is required to verify the safety of the prosthesis. The last but the most important process is to implant in human patient; this process is the only way to know if the eyes with degenerated photoreceptors are able to have the vision with the subretinal prosthesis. Thirdly, the next stage of TSCA stimulation chip is to do in vitro experiment to verify if the equivalent threshold charge of TSCA is lower than SSCA. Fourthly, power efficiency of solar cells has to be improved. One method is to redefine the potential of substrate and DNW rather than let them floating. Besides, since the optimum photo-sensing regions of SCAs have been acquired, we have to fabricate them with higher power efficient solar cells.

Lastly, as we have proved that power efficiency of the FBDP stimulation chip is better than merely solar cell array, the next step is to put sufficient number of solar cells into this version and the test-keys of this chip have to be removed to do in vitro

experiments. Besides, with more power efficient solar cells, the next generation PCU might divide the power into 8 or 16 blocks by elevating clock frequency and adding frequency dividers to increase the subretinal stimulation current.

REFERENCES

[1] W. Liu, E. McGucken, K. Vitchiechom and M. Clements, "Dual unit visual intraocular prosthesis," in Proc. IEEE/EMBS Annual International Conference of the IEEE, vol. 5, Nov. 1997, pp. 30.

[2] M. Javaheri, D. Hahn, R. Lakhanpal, J.D. Weiland, M.S. Humayun, "Retinal prostheses for the blind," in Annals Academy of Medicine, vol. 35, March 2006, no. 3.

[3] Dobelle WH, "Artificial vision for the blind by connecting a television camera to the visual cortex," in Journal of ASAIO, vol.46, pp.3-9, 2000.

[4] C. Veraart, M.C. Wanet-Defalque, B. Gerard, A. Vanlierde, J. Delbeke, "Pattern recognition with the optic nerve visual prosthesis," IEEE Journal of Artificial Organs, vol. 27, pp.996-1004, 2003.

[5] Y. Terasawa, H. Tashiro, A. Uehara, T. Saitoh, M. Ozawa, T. Tokuda, and J. Ohta, "The development of a multichannel electrode array for retinal prostheses," IEEE Journal of Artificial Organs, vol. 9, pp.263–266, 2006.

[6] J. A. Zhou, S. J. Woo, S. I. Park, E. T. Kim, J. M. Seo, H. Chung, and S. J. Kim, "A suprachoroidal electrical retinal stimulator design for longterm animal experiments and in-vivo assessment of its feasibility and incompatibility in rabbits," IEEE Journal of Biomed. Biotech., vol. 2008, pp.547428-1–547428-10, 2008.

[7] T. Tokuda, R. Asano, S. Sugitani, Y. Terasawa, et al., "In vivo stimulation on rabbit retina using CMOS LSI-based multi-chip flexible stimulator for retinal prosthesis," in Proc. IEEE/EMBS Annual International Conference of the IEEE, Aug. 2007, pp.5790-5793, 22-26.

[8] J.D. Weiland, W. Liu, M.S. Humayun, "Retinal prosthesis," in Annu Rev Biomed Eng, 2004.

[9] M.S. Humayun, J.D. Dorn, A.K. Ahuja, A.Caspi, et al, "Preliminary 6 month results from the argus^{tm} epiretinal prosthesis feasibility study," in Proc. IEEE/EMBS Annual International Conference of the IEEE, Sept. 2009, pp.4566-4568, 3-6,.

[10] J.D. Weiland and M.S. Humayun, "Visual Prosthesis," in Proc. of the IEEE, vol. 96, no. 7, July 2008.

[11] R. Eckmiller, M. Becker, R. Hunermann, "Dialog concepts for learning retina encoders," in International Conference on Neural Networks, vol.4, 9-12, Jun. 1997, pp.2315-2320.

[12] R. Eckmiller, O, Baruth, D.Neumann, “Learning retina encoder RE: results from dialog-based tuning in humans with normal vision,” in Invest Ophthalmol Vis Sci, 2005.

[13] J.F. 3rd Rizzo, J. Wyatt, J. Loewenstein, S. Kelly, D. Shire, “Methods and perceptual thresholds for short-term electrical stimulation of human retina with microelectrode arrays,” in Invest Ophthalmol Vis Sci, 2003, pp.44:5355-61.27.

[14] J.F. 3rd Rizzo, J. Wyatt, J. Loewenstein, S. Kelly, D. Shire, “Perceptual efficacy of electrical stimulation of human retina with a microelectrode array during short-term surgical trials,” in Invest Ophthalmol Vis Sci, 2003, pp.44:5362-9.

[15] A. Chow, V. Chow, K. Packo, J. Pollack, G. Peyman, R. Schuchard, “The artificial silicon retina microchip for the treatment of vision loss from retinitis pigmentosa,” in Arch Ophthalmol, 2004, pp.122:460-9.

[16] A. Chow, V. Chow, “Subretinal electrical stimulation of the rabbit retina,” in Neuroscience Letters, vol. 225, 1997, pp.13–16.

[17] F. Gekeler, P. Szurman, S. Grisanti, U. Weiler, R. Claus, T. O. Greiner, M. vol.ker, K. Kohler, E. Zrenner, and K. U. Bartz-Schmidt, “Compound subretinal prostheses with extra-ocular parts designed for human trials: Successful long-term implantation in pigs,” in Graefes Arch. Clin. Exp. Ophthalmol., 2006.

[18] E. Zrenner, “Subretinal implants for the restitution of vision in blind patients,” presented at the ARVO Annu. Meeting, Ft. Lauderdale, FL, USA, 2007.

[19] E. Zrenner, R. Wilke, et al., “Subretinal Microelectrode Arrays Allow Blind Retinitis Pigmentosa Patients to Recognize Letters and Combine them to Words,” in Biomedical Eng. and Informatics, 2009.

[20] D. Shire, S. Kelly, J. Chen, P. Doyle, J.F. 3rd Rizzo, et al., “Development and implantation of a minimally invasive wireless subretinal neurostimulator,” in Biomedical Eng., vol. 56, no. 10, Oct. 2009.

[21] J. Loudin, D.M. Simanovskii1, et al., “High resolution optoelectronic retinal prosthesis,” in Proc. of SPIE, vol. 7163 71631B-1, 2009.

[22] S. Shah, A. Hines, D. Zhou, R.J. Greenberg, M.S. Humayun, and J.D. Weiland, “Electrical properties of retinal-electrode interface,” IEEE Journal of Neural Eng., vol. 4, pp.S24-S29, 2007.

[23] S. Dokos, G. J. Suaning, and N. H. Lovell, “A Bidomain model of epiretinal stimulation,” IEEE Trans on Neural Syst Rehab Eng, vol. 13, pp.137-146, 2005.

[24] W. Liu, “Retinal Implant: Bridging engineering and medicine,” in IEDM Digest, pp.492-495, Dec. 2002.

[25] C. Wan, C.Y. Wu, P.K. Lin, “A CMOS implantable retinal chip with solar cell

power supply control circuit for retina prostheses," unpublished master degree's dissertation, National Chiao Tung University of Taiwan.

[26] C.C. Chiao, Y.T. Yang, C. Wan, W.C. Yang, L.J. Lin, P.K. Lin, C.Y. Wu, "Responses of rabbit retinal ganglion cells to subretinal electrical stimulation with a silicon-based microphotodiode array," presented at the ARVO Annu. Meeting, Ft. Lauderdale, FL, USA, 2010.

[27] F. Gekeler, A. Stett, E. Zrenner, "Subretinal electrical stimulation of the rabbit retina with acutely implanted electrode arrays." in Graefes Arch. Clin. Exp. Ophthalmol., vol. 242, issue 7, July 2004, no. 587-596.

[28] R.J. Jensen and J.F. 3rd Rizzo, "Responses of ganglion cells to repetitive electrical stimulation of the retina," IEEE Journal of Neural Eng., vol.4, pp.S1-S6, 2007.

[29] T. Ytterdal, Y. Cheng, T.A. Fjeldly, "Device modeling for analog and RF CMOS circuit design," copyright of John Wiley & Sons, Ltd, 2003.

[30] D. Palanker, A. Vankov, P. Huie and S. Baccus, "Design of a high-resolution optoelectronic retinal prosthesis," IEEE Journal of Neural Eng. vol.2 pp.S105-S20, 2005.

[31] M. Ferri, D. Pinna, E. Dallago, P. Malcovati, "Integrated micro-solar cell structures for harvesting supplied microsystems in 0.35-μm CMOS technology," IEEE SENSORS Conference, 2009.

VITA

姓 名：柳慧君

學 歷：

私立天主教宏仁女子中學　(90年9月~93年6月)
國立中興大學電機工程學系　(93年9月~97年6月)
國立交通大學電子研究所碩士班　(97年9月~99年8月)

研究所修習課程：

類比積體電路	吳介琮教授
數位積體電路	周世傑教授
積體電路之靜電放電防護設計特論	柯明道教授
計算機結構	劉志尉教授
鎖相迴路設計與應用	陳巍仁教授
三維積體電路	陳冠能教授
生物晶片技術	袁俊傑;黃遠東
穩健設計之品質工程	黎正中教授
電子商務	彭德保

永久地址：嘉義縣竹崎鄉內埔村過坑2-4號

Email：airplane1121.ee97g @nctu.edu.tw
m9711664@alab.ee.nctu.edu.tw